

https://dspace.org/

Identification of refractory material failures in cement kilns

Lugisani, Peter

2016

http://hdl.handle.net/10539/22336

Lugisani, Peter (2016) Identification of refractory material failures in cement kilns, University of Witwatersrand, Johannesburg, <http://wiredspace.wits.ac.za/handle/10539/22663>

Downloaded from a DSpace repository. https://dspace.org/



IDENTIFICATION OF REFRACTORY MATERIAL FAILURES IN CEMENT KILNS

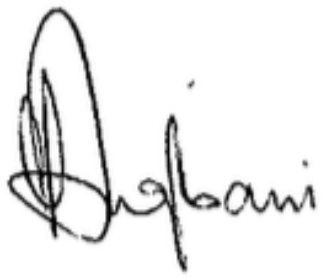
Peter Lugisani

A dissertation submitted to the Faculty of Engineering and the Built Environment, University of the Witwatersrand, Johannesburg, in fulfilment of the requirements for the degree of Master of Science in Engineering

Johannesburg, 11 October 2016

DECLARATION

I declare that this dissertation is my own unaided work. It is being submitted for the Degree of Master of Science in Engineering to the University of the Witwatersrand, Johannesburg. It has not been submitted before for any degree or examination to any other University



Peter Lugisani

11th day of October year 2016

ABSTRACT

Refractory lining failure of damaged magnesia bricks and used alumina bricks was investigated by XRF, XRD, SEM-EDS analysis and computational thermochemistry (phase diagrams). In addition, the effect of oxygen partial pressure towards the refractory lining and alkali sulphate ratio were also determined. The presence of low melting phases of KCl, (Na, K) Cl, K_2SO_4 and $CaSO_4$ compromised the refractoriness of the magnesia bricks because they are liquid at temperatures below clinkerisation temperature (1450 °C). Sodium oxide and potassium oxide in the kiln feed and chlorine and sulphur in the kiln gas atmosphere migrated into the magnesia brick and react to form KCl, (Na, K) Cl and K_2SO_4. Components of the magnesia brick, CaO reacted with the excess sulphur in the kiln gas atmosphere forming $CaSO_4$. The presence of these impurity phases indicated that the magnesia bricks suffered chemical attack. Potassium and part of components of high-alumina brick reacted to form K_2 ($MgSi_5O_{12}$) impurity phase. Phase diagram predictions indicated that the presence of sodium at any given concentration automatically results in liquid formation in the high alumina brick. This confirms that the chemical attack is also the cause of the failure of the high alumina brick. The analysis of the microstructures of both unused and damaged magnesia bricks revealed that the fracture was predominantly intergranular whereas, in high alumina brick, the fracture was transgranular. The absence of evidence of micro-cracks in both magnesia and alumina bricks rules out thermal shock as a failure

mechanism. The absence of clinker species and phases in the examined magnesia and alumina bricks indicated that corrosion by clinker diffusion was absent. The partial pressure of oxygen is low (1.333×10^{-4} atm), it indicates the stability of Fe_3O_4 and Mn_3O_4 and therefore does not favour the oxidation of Fe_3O_4 to formation of Fe_2O_3 and Mn_3O_4 to formation of Mn_2O_3. The values of alkali sulphate ratio indicated that the kiln operating conditions were favourable for chemical attack to occur.

PUBLICATIONS AND PRESENTATIONS

Journal Publications

Lugisani, P., Eric, R. H., 2014. Identification of failure of refractory materials in cement kilns. *Submitted to SAIMM* (pending publication)

Conference Proceedings

Lugisani, P., Eric, R. H., 2013. Identification of refractory materials failure(s) in cement kilns. In: Refractories Conference 2013, SAIMM, Muldersdrift – Misty Hills, South Africa, April 23 – 24.

DEDICATION

I dedicate this work to my wife Dr. Mmapula Lugisani. Your love, support and encouragement always enables me to do better.

ACKNOWLEDGEMENTS

Firstly I thank God for making it possible to study for this degree and providing me with all resources that were required for the research to be completed.

I thank my supervisor Professor R.H. Eric for his guidance throughout my research, his willingness to guide me was instrumental for the successful completion of this research work.

I also thank AfriSam Ulco cement plant for supplies of materials for this research.

I thank Mr Kalenda Mutombo from CSIR for his assistance with microscopy.

I thank Doctor Johan Zietsman from University of Pretoria for assistance with FactSage software.

I thank Mr Alain Mutombo from University of Pretoria for his encouragement and critique.

Contents

1 INTRODUCTION 2

1.1 Research objectives 5

1.2 Research questions 5

1.3 Approach 6

2 LITERATURE REVIEW 9

2.1 Introduction 9

2.2 Refractory materials 9

2.2.1 The alumina-silica refractory 10

2.2.2 The basic refractory 10

2.3 Refractory lining failures 11

2.4 Chemical corrosion behaviour by clinker diffusion 12

2.4.1 Introduction 12

2.4.2 Sample preparation and analysis 12

2.4.3 Clinker corrosion of $MgAl_2O_4$, MgO and MgO-$CaZrO_3$-calcium silicate materials. 13

2.4.4 Corrosion behaviour of MgO/CaZrO3 matrix by clinker 15

2.4.5 Interaction between Clinker-MgO-$CaZrO_3$ 16

2.4.6 Conclusion 18

2.5 Chemical corrosion by cement kiln materials 19

2.5.1 Introduction 19

2.5.2 Sample preparation and chemical analysis 19

2.5.3 The chemical corrosion of magnesia-spinel and magnesia-zirconia 21

2.5.4 High-temperature chemical corrosion. 24

2.5.5 The wear phenomena of refractory linings in the burning zone 27

2.5.6 The refractories corrosion in cement rotary kilns fired with waste fuels 27

2.5.7 Conclusion 29

2.6 Thermal shock of refractory materials 30

2.6.1 Introduction 30

2.6.2 Sample preparation and thermal shock analysis 30

2.6.3 The effect of spinel content on the properties of magnesia-spinel composite. 33

2.6.4 Fracture behaviour of magnesia and magnesia-spinel composites. 34

2.6.5 Thermal shock behaviour of magnesia-spinel composites. .. 36

2.6.6 The mechanical properties of magnesia-spinel composites . 39

2.6.7 Conclusion 41

2.7 The effect of partial pressure of oxygen or CO_2/CO gas mixtures 44

2.7.1 Introduction 44

2.7.2 Stability of Fe_2O_3 and Mn_2O_3 46

2.7.3 Redox burning conditions 47

3 EXPERIMENTAL PROCEDURE 50

3.1 Materials 51

3.1.1 The unused brick 51

3.1.2 The used (damaged) brick 51

3.1.3 The kiln feed 51

3.2 The industrial kiln 52

3.3 Sample preparation 53

3.4 Analytical methods 54

3.4.1 XRF 54

3.4.2 XRD 55

3.4.3 SEM-EDS 55

3.5 Computational thermochemistry (FactSage) 56

3.6 Carbon monoxide / carbon dioxide (CO_2/CO) measurements 56

3.7 Alkali-sulphate ratio 56

4 RESULTS AND DISCUSSION: MAGNESIA BRICKS 59

4.1 Introduction 59

4.2 Chemical analysis of the magnesia refractory lining..... 59

4.3 Formation of impurity species in the damaged bricks..... 66

4.3.1 Formation of KCl..... 67

4.3.2 Formation of $CaSO_4$ 67

4.3.3 Formation of (Na, K) Cl..... 68

4.3.4 Formation of K_2SO_4 68

4.4 Diffusion of the clinker into the magnesia bricks 70

4.5 Microstructural examination for thermal shock attack..... 76

4.6 Thermodynamics (phase diagrams)..... 80

4.6.1 Effect of chlorine (Cl_2)..... 81

4.6.2 Effect of sulphur trioxide (SO_3) 84

4.6.3 Effect of sodium oxide (Na_2O) 88

4.6.4 Effect of potassium oxide (K_2O)..... 93

4.7 Conclusion 98

5 RESULTS AND DISCUSSION: HIGH - ALUMINA BRICK..... 100

5.1 Introduction 100

5.2 Chemical analysis of the high-alumina refractory lining..... 100

5.3 Formation of impurity species in the damaged high-alumina brick 104

5.3.1 Formation of K_2 ($MgSi_5O_{12}$) 104

5.4 Diffusion of clinker into the high-alumina brick 105

5.5 Microstructural examination and analysis for thermal shock attack 108

5.6 Thermodynamics (phase diagrams) 110

5.6.1 Effect of sulphur trioxide (SO_3) 111

5.6.2 Effect of sodium oxide 113

5.6.3 Effect of potassium oxide (K_2O) 116

5.7 Conclusion 119

6 RESULTS AND DISCUSSION: EFFECT OF PARTIAL PRESSURE OF OXYGEN 121

6.1 Introduction 121

6.2 Calculation of the oxygen partial pressure 121

6.3 Stability of oxides in the refractory lining 124

6.3.1 Reduction of Hematite (Fe_2O_3) 124

6.3.2 Reduction of Mn_2O_3 126

6.3.3 Conclusion 127

7 CONCLUSIONS AND RECOMMENDATIONS 129

7.1 Introduction 129

7.2 Effect of impurities 129

7.3 Thermal shock attack 130

7.4 Corrosion by clinker 131

7.5 Effect of kiln operating conditions 131

7.6 Alkali sulphate ratio 132

7.7 Recommendations 132

REFERENCES 134

APPENDICES 138

APPENDIX A: XRD RESULTS 139

APPENDIX B: Calculations for conversion from mass% to mole% 148

APPENDIX C: ASR data 150

APPENDIX D: Kiln feed composition 151

APPENDIX E: Residence time in Kiln 152

LIST OF FIGURES

Figure 2-1. SEM micrographs for the clinker–$MgAl_2O_4$ interface of the sample fired at 1500 °C for 1 min 14

Figure 2-2. X-ray maps of corrosion scale from case 1 kiln 25

Figure 2-3. X-ray maps of corrosion scale from case 2 kiln 25

Figure 2-4. SEM photograph of a fracture face of pure MgO, showing pronounced transgranular fracture. 40

Figure 2-5. SEM photograph of a fracture face of 20% 22 μm spinel composites, showing predominantly intergranular fracture 40

Figure 3-1 Experimental procedure for sample preparation and analysis 50

Figure 3-2 Schematic diagram of the kiln 53

Figure 3-3. ASR of the study kiln 57

Figure 4-1. SEM-EDS mapping of magnesia-spinel brick type A 62

Figure 4-2. SEM-EDS mapping of magnesia-spinel brick type B 63

Figure 4-3. SEM-EDS mapping magnesia-fused spinel 64

Figure 4-4. The SEM micrograph polished brick section of magnesia-spinel brick type A, a) the unused, and b) the damaged 73

Figure 4-5. The SEM micrograph polished brick section of magnesia-spinel brick type B, a) the unused, and b) the damaged 74

Figure 4-6. The SEM micrograph polished brick section of magnesia-fused spinel, a) the unused, and b) the damaged 75

Figure 4-7. The SEM micrograph fracture of magnesia-spinel brick type A, a) the unused, and b) the damaged 76

Figure 4-8. The SEM micrograph fracture of magnesia-spinel brick type B, a) the unused, and b) the damaged 77

Figure 4-9. The SEM micrograph fracture of magnesia-fused spinel brick, a) the unused, and b) the damaged..... 78

Figure 4-10. System MgO-Al_2O_3-KCl ternary phase diagram at 1500 °C and 1 atmosphere for magnesia-spinel brick type A..... 82

Figure 4-11. System MgO-Al_2O_3-KCl ternary phase diagram at 1500 °C and 1 atmosphere for magnesia-fused spinel..... 83

Figure 4-12. System MgO-CaO-SO_3 ternary phase diagram at 1500 °C and 1 atmosphere for magnesia-spinel brick type A..... 85

Figure 4-13. System MgO-CaO-SO_3 ternary phase diagram at 1500 °C and 1 atmosphere for magnesia-spinel brick type B..... 86

Figure 4-14. System MgO-CaO-SO_3 ternary phase diagram at 1500 °C and 1 atmosphere for magnesia-fused spinel..... 87

Figure 4-15. System MgO-Al_2O_3-Na_2O ternary phase diagram at 1500 °C and 1 atmosphere for magnesia-spinel brick type A..... 89

Figure 4-16. System MgO-Al_2O_3-Na_2O ternary phase diagram at 1500 °C and 1 atmosphere for magnesia-spinel brick type B..... 90

Figure 4-17. System MgO-Al_2O_3-Na_2O ternary phase diagram at 1500 °C and 1 atmosphere for magnesia-fused spinel..... 91

Figure 4-18. System MgO-Al_2O_3-Na_2O ternary phase diagram at 1500 °C and 1 atmosphere 92

Figure 4-19. System MgO-Al_2O_3-K_2O ternary phase diagram at 1500 °C and 1 atmosphere for magnesia-spinel brick type A..... 94

Figure 4-20. System MgO-Al_2O_3-K_2O ternary phase diagram at 1500 °C and 1 atmosphere for magnesia-spinel brick type B..... 95

Figure 4-21. System MgO-Al_2O_3-K_2O ternary phase diagram at 1500 °C and 1 atmosphere for magnesia-fused spinel..... 96

Figure 4-22. System MgO-Al_2O_3-K_2O ternary phase diagram at 1500 °C and 1 atmosphere 97

Figure 5-1. SEM-EDS mapping of the damaged high-alumina powder sample..... 102

Figure 5-2. The SEM micrograph of high-alumina polished brick section, a) the unused, and b) the damaged..... 107

Figure 5-3. The SEM micrograph of fracture high-alumina brick, a) the unused, and b) the damaged..... 109

Figure 5-4. System Al_2O_3-CaO-SO_3 ternary phase diagram at 1200ºC and 1 atmosphere 112

Figure 5-5. System Al_2O_3-SiO_2-Na_2O ternary phase diagram at 1200ºC and 1 atmosphere 114

Figure 5-6. System Al_2O_3-SiO_2-Na_2O ternary phase diagram at 1200ºC and 1 atmosphere 115

Figure 5-7. System Al_2O_3-SiO_2-K_2O ternary phase diagram at 1200ºC and 1 atmosphere 117

Figure 5-8. System Al_2O_3-SiO_2-K_2O ternary phase diagram at 1200ºC and 1 atmosphere 118

LIST OF TABLES

Table 3-1 Industrial kiln feed chemical composition 52

Table 4-1. Chemical compositions of virgin and damaged magnesia brick, based on XRF assay 60

Table 4-2. Elemental composition of virgin and damaged magnesia powder sample, based on SEM-EDS analysis 61

Table 4-3. Phase composition of the virgin and damaged magnesia bricks, based on XRD analysis 65

Table 4-4. Elemental composition of the damaged magnesia polished brick section, based on SEM-EDS chemical analysis. 70

Table 4-5. Molar composition of the damaged magnesia lining, based on XRF assay 80

Table 4-6. Normalised composition of the damaged magnesia lining, for Cl_2 effect 81

Table 4-7. Normalised composition of the damaged magnesia lining, for SO_3 effect 84

Table 4-8. Normalised composition of the damaged magnesia lining, for Na_2O effect 88

Table 4-9. Normalised composition of the damaged magnesia lining, for K_2O effect 93

Table 5-1. Chemical composition of virgin and damaged high-alumina brick, based on XRF assay 100

Table 5-2. Elemental composition of virgin and damaged high-alumina powder sample, based on SEM-EDS analysis 101

Table 5-3. Phase composition of the virgin and used high-alumina lining, based on XRD analysis 103

Table 5-4. Elemental composition of the damaged high-alumina polished brick section, based on SEM-EDS chemical analysis 105

Table 5-5 Molar composition of the damaged high-alumina lining, based on XRF assay 110

Table 5-6. Normalised composition of the damaged high-alumina brick, for SO_3 effect 111

Table 5-7. Normalised composition of the damaged high-alumina brick, for Na_2O effect 113

Table 5-8. Normalised composition of the damaged high-alumina brick, for K_2O effect 116

Table 6-1: Volume percent of CO_2 and CO, measured from industrial kiln 122

LIST OF SYMBOLS

XRF:	X-ray fluorescence
XRD:	X-ray powder diffraction
SEM:	Scanning electron microscopy
EDS:	Energy dispersive spectrometry
ASR:	Alkali sulphate ratio
E:	Young's modulus
MOR:	Modulus of rupture
RUL:	Refractoriness under load
T_{qc}:	Critical quench temperature
T_{q}:	Quenching temperature
wt%:	Weight percentage
Ywof:	Work of fracture
$MgAl_2O_4$:	Spinel
L:	Liquid
MS_pI:	MgO, β-Ca_2SiO_4, $C_{12}A_7$, $C3A_3$, $CaSO_4$, C_3A, C_4AF
MS_pII:	MgO, β-Ca_2SiO_4, $CaZrO_3$, $MgAl_2O_4$, $Ca_{20}A_{13}M_3S_3$, $C_{12}A_7$, $C_3A_3.CaSO_4$, C_4AF
C_7A_3Z:	$Ca_7Al_6ZrO_{18}$

EDX:	Energy dispersive x-ray spectrometry
R:	Thermal shock resistance parameter
(C_6A_4 (M, F) S):	Ca_6Al_8 (Mg, Fe) SiO_{23}
C_2 (A, F):	Calcium alumina-ferrite
C_3A:	$Ca_3Al_2O_6$
C_3A_3Z:	$Ca_7Al_6ZrO_{18}$
C_2S:	Ca_2 [SiO_4]
C_3S:	Ca_3 [SiO_4] O
C_3MS_2:	Ca_3Mg [SiO_4]$_2$
M_2S:	Mg_2 [SiO_4]
CMS:	CaMg [SiO_4]
MZ:	Magnesia-zirconia
MSp:	Magnesia-spinel
C_4AF:	Ca_2AlFeO_5
$C_{12}A_7$:	$Ca_{12}Al_{14}O_{21}$
$C_3A_3.CaSO_4$:	$Ca_4Al_6O_{12}$ (SO_4)

CHAPTER ONE

1 INTRODUCTION

South Africa produces approximately 25 million tonnes of cement a year and one of the major processes in the production of cement is the manufacture of clinker. Clinker is produced through the burning of limestone, iron ore and shale by coal in a rotary kiln. The kiln has a burning zone (see figure 3-2) where clinkerisation takes place between 1450°C and 1500°C. After clinkerisation the clinker flows through a lower transition zone (see figure 3-2) where the temperature drops off in order to contain the clinker phases. The bricks used in the burning zone are basic magnesia-spinel and magnesia-fused spinel and those for the lower transition zone are high-alumina. The main objective of this study is to identify the causes of refractory-lining failure in cement kilns and examine the burning and lower transition zones.

Many cement plants suffer from unpredictable failure of the kiln refractory lining, which results in down time and loss of revenue. The cement plant cost of replacing the refractory lining is in a region of R100 000 per metre in a kiln of 4.6m diameter. This amount represents only the cost of the refractory itself and includes neither the added expense of installation, nor the hidden cost associated with a loss in production, extra fuel required for pre-heating and maintaining the kiln temperature. The kiln in this study had a poor availability owing mainly to refractory lining failure, which averages around 75% over the last 5 years, 70% in the last two years and 65% in the year 2011 (up to June).

Six refractory lining failures occurred in the burning zone between 2010 and 2011.

Peray and Waddell (1972) concluded that the refractory lining failures in rotary cement kilns are caused by thermal shock, chemical attack and mechanical failure. For instance, the refractory-lining failure in rotary cement kilns occurs when the kiln shell becomes overheated. The refractory lining can then be either entirely lost or reduced to a thinner layer resulting in inadequate protection of the kiln shell. The overheating of the kiln shell increases the probability of the steel shell to warp to such an extent that a replacement of the entire kiln shell section becomes necessary.

Szczerba (2010) found that the main cause of refractory-lining failure is the chemical attack of the spinel phase in basic refractories by sulphur and chlorine contained in the kiln feed. The sulphur and chlorine can react with the spinel phase to form low melting aluminate phases of $Ca_{12}Al_{14}O_{33}$, $Ca_3Al_2O_6$, Ca_6Al_8 (Mg, Fe) SiO_{23} and $Ca_4Al_6O_{12}$ (SO_4) (Szczerba, 2010).

Peray and Waddell (1972) also reported that refractory-lining failure occurs due to repeated kiln shutdown and start-up, or severe operating upset which usually create large temperature changes in the kiln and subject the lining to thermal shock.

Failure of basic refractories might occur from excessive thermal expansion owing to lower spinel content. It was found that addition of 20 wt% spinel

content will result in a gradual decrease in thermal expansion and will greatly improve refractoriness under load and increase retained strength after thermal shock (Ghosh et al. 2004)

Pena et al. (2007) showed that the chemical corrosion of refractory lining by clinker diffusion into the refractory brick is associated with the failure mechanism that affects rotary cement kilns. In general, the mechanism of the attack of refractory (corrosion) of the refractory lining materials by clinker is explained by a matter diffusion of the liquid clinker phase through the grain boundaries and open pores into the refractory materials (Pena et al. 2007).

Bartha and Sodje (2001) found that redox burning conditions represent a low proportion of the overall volume of cases of wear, but can occur more frequently where alternative fuels are used. The mechanism of this failure is by formation of sulphate salts or sulphides resulting in the structural weakening of the affected brick horizons (brick phase).

In this study, post-mortem samples collected from industrial kilns provide opportunities to investigate the potential mechanisms of failure, whereas experimental tests, under controlled conditions in the laboratory, were carried out to investigate only one failure mechanism at a time.

Furthermore the chemical attack and thermal shock were investigated by studying the chemical compositions and microstructures of unused and used refractory lining materials collected from an industrial kiln. The partial pressure

of oxygen was measured to determine the conditions in the kiln (oxidising or reducing) which in turn affect the stability of Mn_3O_4 and Fe_3O_4 phases of the brick.

The main research objectives of this work and research questions that this work will attempt to answer are provided in section 1.1 and 1.2 respectively.

1.1 Research objectives

The research objectives of this work was to determine the causes of the refractory lining failures considering the effect of feed and kiln conditions. This is summarised as follows:

a. To identify the causes of refractory lining failures in an industrial cement kiln
b. To understand the effects of impurities on the refractory lining materials
c. To understand the effects of cement kiln operating conditions on the refractory lining materials
d. To generate data for use in kiln operations

1.2 Research questions

This research was conducted to answer the questions on how the refractory lining was prematurely failing and the questions were summarised as follows:

a. What are the failure mechanisms that resulted in premature refractory lining failure?

b. What are the effects of the alkalis in the refractory lining?
c. What are the effects of the gaseous sulphur trioxide and chlorine in the refractory lining?
d. What is the effect of oxygen partial pressure in the refractory lining?

The approach which was adopted for this research involved investigating all possible failures and is describe in section 1.3.

1.3 Approach

The majority of refractory lining failure research has been conducted by reacting prepared refractory sample materials with either kiln feed or clinker in a laboratory furnace or hot stage microscope for the investigation of chemical corrosion through analysis and microstructural studies. In the case of thermal shock studies the prepared refractory materials of different compositions are fired to set temperatures (1200°C, 1400°C and 1500°C) and subjected to different tests and analysis such as thermal expansion, strength and Young's modulus, refractoriness under load (RUL) and factography. This research however took a different approach by collecting the used refractory lining materials from the industrial cement kiln which allowed the investigation of more than one refractory lining failure. This research investigated lining failure by chemical and thermal attack using the same samples collected in the industrial kiln. The kiln operating condition during the period at which samples were

collected was also investigated to determine the influence of oxygen partial pressure on the stability of Mn_3O_4 and Fe_3O_4 phases on the refractory.

CHAPTER TWO

2 LITERATURE REVIEW

2.1 Introduction

The clinker production process occurs at higher temperatures (1400 -1500°C) inside the kiln. It is therefore a requirement that the kiln shell is protected with a refractory. Failure to provide protection would lead to shell disintegration (Peray and Waddell., 1972).

Many cement plants suffer from unpredictable failure of the kiln refractory lining, which results in down time and loss of revenue.

The clinker formation occurs at the burning zone of the kiln at approximately 1450°C. Due to higher temperature exposure, frequent refractory lining replacement is required. The life of refractory lining applied at the rotary kiln varies from different operators depending on factors at which it is exposed to. Some of the common factors that have an adverse effect towards the refractory lining are the mineral composition of the feed, type of fuel used, kiln operating conditions and the mechanical integrity of the kiln (Peray and Waddell, 1972).

2.2 Refractory materials

A refractory is a material, usually non-metallic, that is used to withstand high temperature. Refractory materials must be chemically and physically stable at high temperatures. Depending on the operating environment, they need to be

resistant to thermal shock, be chemically inert and/or have specific ranges of thermal conductivity and of the coefficient of thermal expansion (Peray and Waddell, 1972).

The oxides of aluminium (alumina), silicon (silica) and magnesium (magnesia) are the most important materials used in the manufacturing of refractories.

Refractories must be chosen according to the conditions they will face. Some applications require special refractory materials. Zirconia is used when the material must withstand high temperatures.

This study examined refractory materials that contain magnesia, alumina and silica oxides.

2.2.1 The alumina-silica refractory

The two main components in these refractories are alumina and silica. Usually an increase in the alumina content will result in higher refractoriness. In addition, the spalling resistance, conductivity and strength are also enhanced. Its limitation could however be a greater reversible expansion and lower slag resistance than that of basic brick (Peray and Waddell, 1972).

2.2.2 The basic refractory

The basic refractories are manufactured mainly from periclase (MgO phase), aluminate, dead burned magnesite, and chrome ore. The basic refractories

have a greater resistance to chemical attack by ash, slag, alkalies at higher temperatures. However these materials have a poor spalling resistance compared to alumina bricks. Nowadays a spinel of magnesia-alumina refractory brick is recommended to address the poor spalling resistance. Periclase gives the basic refractory a higher refractoriness and volume stability. This refractory is preferred in the burning zone of the rotary cement kiln because of its ability in forming coating which protects the refractory (Peray and Waddell, 1972.).

This study looked at alumina refractory materials applied at the lower transition zone and magnesia refractory materials applied at the burning zone.

2.3 Refractory lining failures

The refractory lining failure of rotary cement kilns may result from the chemical attack, thermal shock attack or mechanical failures.

The chemical attack occurs as a result of chemical reaction between refractory materials and impurities in kiln feed materials and fuel used (whatever gas, slag or metal is likely to be encountered) (Gilchrist., 1977). The dust and alkalies entrained in the gases can adhere to the bricks in the burning zone and react with the refractory materials (Peray and Waddell, 1972). The corrosion of refractories by cement kiln materials involves chemical reactions between the refractories, clinker and the volatile materials in the kiln (Szczerba., 2010, Bartha and Sodje., 2001, Kunnecke., 1998 and Potgieter et al., 2004).

The chemical corrosion also occurs through diffusion of clinker through grain boundaries and the residual porosity of the refractory lining (Pena et al., 2007, Serena et al., 2004 and Cabarello et al., 2009).

The thermal attack of the refractory materials in rotary cement kilns is caused by the effect of thermal expansion and fracture behaviour of the refractory materials under the working temperature (Gilchrist., 1977 and Peray and Waddell., 1972).

2.4 Chemical corrosion behaviour by clinker diffusion

2.4.1 Introduction

The behaviour and mechanism of corrosion by clinker have been investigated by Pena et al., 2007, Serena et al., 2004 and Caballero et al., 2009. Their works extensively focussed on studying the reaction behaviour at the interface of cement / refractory materials. In addition, they also studied the microstructural characteristics of the reaction interface between the cement clinker and refractory materials after corrosion treatment.

2.4.2 Sample preparation and analysis

Prepared refractory materials of different composition are placed in contact with the clinker and thermally heated to temperatures up to 1500ºC for the corrosion reaction to take place. The chemical reaction between the refractory and clinker

results in a mass product transport that allows the corrosion to take place. After firing process samples are cut perpendicular to the clinker-ceramic interface.

There are numerous ways to analyse the corrosion reaction. Pena et al., 2007 conducted analyses of the crystalline phases using reflected light optical microscopy (RLOM) and SEM. Furthermore microanalysis of new layer formed at the reaction-interface was carried out by SEM-EDS and grain size measurements of the different crystalline phases were carried out using the linear interception method on representative SEM micrographs. Serena et al., 2004 and Caballero et al., 2009 performed microstructural and phase identification through optical microscopy and SEM-EDS.

2.4.3 Clinker corrosion of $MgAl_2O_4$, MgO and MgO-$CaZrO_3$-calcium silicate materials.

Pena et al., 2007 investigated the corrosion of MgO-$CaZrO_3$-calcium silicate materials by looking at phase formation at the interface and in the bulk of the MgO-$CaZrO_3$-calcium silicate materials taking into account the phase equilibrium data of the MgO-Al_2O_3-CaO and MgO-CaO-SiO_2-ZrO_2 systems compared with MgO and $MgAl_2O_4$ ceramic materials.

The results showed that clinker-$MgAl_2O_4$ pair reaction took place at temperature of 1450ºC. Whilst the reaction of clinker and MgO or MgO-$CaZrO_3$-calcium silicate materials only occurred at 1600ºC (Pena et al., 2007). The

microstructure shows the presence of a devitrified glassy phase, liquid at 1500 ºC which was produced by the chemical reaction between clinker and $MgAl_2O_4$ (see figure 2-1).

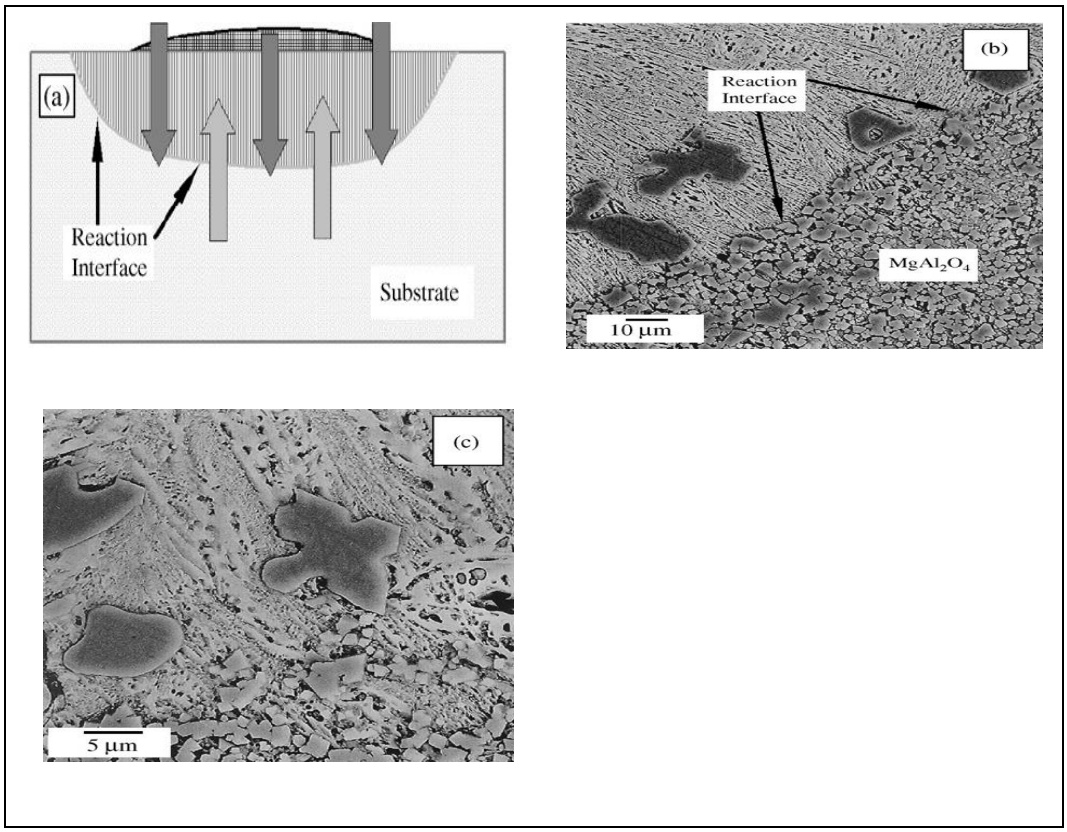


Figure 2-1. SEM micrographs for the clinker–$MgAl_2O_4$ interface of the sample fired at 1500 °C for 1 min

(a) Sketch of the reaction mechanism; typical SEM micrographs, (b) and (c), of the cross-section for the clinker–$MgAl_2O_4$ interface of the sample fired at 1500 °C for 1 min

It was observed that the liquid must gradually dissolve the spinel substrate (Pena et al., 2007). The dissolution of spinel by this glassy phase (liquid clinker)

continues until it reaches equilibrium. At this point, 30% of liquid, L_R, might coexist with $MgAl_2O_4$ as indicated by the following equation:

$MgAl_2O_4 + LC_3A$ {Ca, Al, Si, Fe} $\rightarrow 30\%L_R + 70\%MgAl_2O_4$ (Pena et al., 2007)

The reaction at the MgO/clinker interface indicated that a small quantity of clinker diffused into the MgO substrate (partial diffusion) which is in contrast to the results observed with the reaction of $MgAl_2O_4$/clinker interface (Pena et al., 2007). Pena et al. (2007) found that periclase substrate at temperature higher than 1500ºC revealed an extension of reaction with clinker where small amounts of liquid phases, rich in Ca^{2+}, Al^{3+}, Si^{4+} and $Fe^{2+,3+}$ penetrated through periclase grain boundaries.

Pena et al. (2007) found that the clinker/MgO reaction is slightly faster than that of clinker/MgO-$CaZrO_3$-calcium silicate materials. The dissolution of $CaZrO_3$ increases Zr^{4+} in the liquid, which in turn increases the liquid viscosity and hinders the liquid phase diffusion resulting in a high corrosion resistance of these materials.

Pena et al., 2007 then proposed that the corrosion resistance of the Mg-based ceramic increases in the following sequence:

$MgAl_2O_4$ < MgO-$CaZrO_3$-calcium silicate based materials < MgO

2.4.4 Corrosion behaviour of MgO/CaZrO3 matrix by clinker

Serena et al., 2004 investigated corrosion behaviour of MgO/$CaZrO_3$ refractory matrix by clinker and discussed the reaction between refractory materials and clinker in terms of the MgO-CaO-ZrO_2-SiO_2 system and more specifically on the quaternary system MgO-$CaZrO_3$-C_3S-C_2S (C_3S = Ca_3SiO_5 and C_2S = Ca_2SiO_4).

The porosity in both refractory substrates was reported to mainly be intergranular (Serena et al., 2004). Substrates consisted of a matrix of MgO grains with $CaZrO_3$ located at grain boundaries and triple points. At the initial step of the corrosion process, the liquid of clinker penetrated to the refractory substrate through the open porosity and grain boundaries. This effect produced a decrease in the porosity in the reaction zone, partial dissolution of MgO grains, total dissolution of $CaZrO_3$ and precipitation of C_3S in a limited region of the substrates surface. The dissolution of $CaZrO_3$ grains caused the enrichment of the liquid phase in ZrO_2, increasing its viscosity. MgO grains grew in the presence of liquid, causing the formation of a layer of sintered MgO with liquid triple point. Once this point was reached, the corrosion process ended. The liquid phase showed low Fe_2O_3 and Al_2O_3 content due to their preferential diffusion into the refractory substrates.

2.4.5 Interaction between Clinker-MgO-$CaZrO_3$

Caballero et al., 2009 studied the system of Clinker-MgO-$CaZrO_3$ and its application to the corrosion behaviour of $CaZrO_3$/MgO refractory matrix by clinker. Considering an experimental isothermal section at 1500ºC of the Clinker-MgO-$CaZrO_3$ system and the refractory substrate composition of 20% MgO and 80% $CaZrO_3$, it was found that the refractory material substrate maintains their microstructure and only a small quantity of liquid phase diffuses through grain boundaries and pores.

The corrosion of the refractory substrate can also be illustrated in terms of the connection line between the clinker and the substrate which passes through (C_3S + L), (C_3S + $CaZrO_3$ + L) and (C_3S + $CaZrO_3$ + MgO + L) phase fields. The corrosion process is driven by the penetration of the clinker liquid phase into the substrate through the open porosity and grain boundaries. According to the predictions of the isothermal section, MgO is fully dissolved in a very narrow zone on the substrate surface while $CaZrO_3$ is only partially dissolved. At this point, the interaction between clinker and substrates lies on the line which separates the (C_3S + L) and (C_3S + $CaZrO_3$ + L) phase fields. Corrosion continues with the dissolution of MgO and $CaZrO_3$ until the liquid is saturated with the dissolution of more MgO, CaO and ZrO_2. At this point the liquid composition is in equilibrium with C_3S, MgO and $CaZrO_3$ and consequently the corrosion attack process ends. The dissolution of MgO in a narrow area of

refractory substrate leads to the formation and sintering of $CaZrO_3$ layer, with liquid phase in triple points.

2.4.6 Conclusion

From post-mortem microstructural study, Pena et al. (2007) reported that the corrosion occurs by a diffusion mechanism of the clinker liquid phase through the grain boundaries and open pores in all the studied refractory substrate materials. The liquid phase partially dissolves the $MgAl_2O_4$, $Ca_3Mg\ (SiO_4)_2$, $CaZrO_3$ and MgO phases. In the $CaZrO_3$ bearing materials, the reaction with the clinker liquid phase allows the formation of a zirconium containing silicate liquid boundary layer. The presence of Zr^{4+} increases the liquid phase viscosity and hinders the liquid phase diffusion enhancing the corrosion resistance of these materials. In contrast, the aluminium magnesia spinel materials are markedly dissolved, up to 30%. The good corrosion resistance of the derived MgO-$CaZrO_3$-calcium silicate materials makes them an attractive material to produce binder fine filler for chrome-free magnesia refractory bricks, which are used at the burning zone of rotary cement kilns.

Serena et al., 2004 concluded that the corrosion process is slowed by formation of MgO sintered layer on the refractory substrates. The formation of MgO sintered layer stops the progress of corrosion attack. The studied matrix presented a clinker layer with good adherence that should prevent the corrosion

of the refractory brick in work conditions, improving the corrosion resistance. The good corrosion behaviour of the studied material justifies their use as a matrix in chrome-free magnesia bricks for the burning zone of rotary cement kilns.

Caballero et al., 2009 concluded that the corrosion attack does not cause the formation of cracks inside the refractory substrate in any step of the process. Calcium zirconate must be added to refractory matrices to saturate liquid phase in zirconium oxide in order to increase its viscosity and therefore hindering the liquid phase diffusion through the grain boundary and porosity of the refractory material. The corrosion process of refractory matrices of 20% MgO – 80% $CaZrO_3$ by clinker yields a $CaZrO_3$ sintered layer at the interaction zone.

2.5 Chemical corrosion by cement kiln materials

2.5.1 Introduction

The chemical corrosion by volatile cement kiln feed materials were studied by Szczerba (2010) Bartha and Sodje (2001), Kunnecke (1998) and Potgieter et al. (2004).

2.5.2 Sample preparation and chemical analysis

Szczerba (2010) studied the chemical corrosion between volatile cement kiln feed materials by using a laboratory electric furnace. The temperatures were

set between 1200ºC and 1450ºC. Refractories were tested with cement kiln feed materials which was rich in sulphur and chlorine and the Portland clinker (rich in sulphur). The kiln feed materials volatile components were K_2O 1.7%, Na_2O 0.1%, SO_3 4.9% and Cl^- 3.5%. Portland clinker volatile components were K_2O 1.1%, Na_2O 0.1% and SO_3 2.5%.

The refractory mixtures of magnesia spinel identified as MSpI (MgO 92.1%, Al_2O_3 5.5% and SiO_2 0.3%), MSpII (MgO 82.7%, Al_2O_3 12% and SiO_2 0.4%) and MZII (MgO 82%, ZrO_2 11%, CaO 5.5% and SiO_2 0.3%), were mixed with kiln feed materials or Portland clinker in a mass ratio of 3:1 (Refractory: kiln feed or Portland clinker). The mixed materials samples were ground (polished) and pressed. The samples were then heated between 1200ºC - 1400ºC. Identification of phases was done through XRD analysis.

The refractory sample disks for test work were made from refractory brick mixtures. These disks were then polished before being pressed with the hot kiln feed or with the Portland clinker. The samples were then heated to 1300ºC - 1450ºC. The prepared micro sections were observed by SEM equipped with EDS chemical micro analyser.

Potgieter et al. (2004) investigated the corrosion scales which were collected from the shells of the long (140m) dry-process kiln with one pre-heater and the short (85m) kiln fitted with five pre-heater stages. In both kilns, dolomite bricks were used and the corrosion products were found in the transition zone, about

30 m from the burning zone. Furthermore the corrosion scales were brittle and porous and their colour varied from brown to black. In some areas, KCl salt crystals were observed. The chemical and phase compositions of the corrosion products were analysed by X-ray fluorescence (XRF) and X-ray diffractometry (XRD) technique, respectively. Scanning electron microscopy (SEM) equipped with energy dispersive x-ray spectrometry (EDX) was used for mapping and microanalysis.

2.5.3 The chemical corrosion of magnesia-spinel and magnesia-zirconia

Szczerba (2010) reported XRD results of the reaction product between refractory materials and kiln feed materials. The results indicated new phases that are formed as a result of chemical reactions which were calcium sulphate aluminate $Ca_4Al_6O_{12}$ (SO_4) ($C_3A_3.CaSO_4$) (in MSpI, MSpII and MZ samples) and calcium zirconate $CaZrO_3$ (in MSpII and MZ). The formation of the $C_3A_3.CaSO_4$ phase was probably due to reactions between the spinel and kiln feed. The spinel from the bricks and kiln feed materials with volatile components (e.g. $CaSO_4$ and CaO) or kiln feed materials with volatile components, $CaSO_4$, $Ca_3Al_2O_6$, CaO and SiO_2 and ZrO_2 from the MZ brick, reacted according to the following equations:

$CaSO_4 + 3CaO + 3MgAl_2O_4 \rightarrow Ca_4Al_6O_{12}(SO_4) + 3MgO$ E.q 2-1

$CaSO_4 + 3Ca_3Al_2O_6 + 2SiO_2 + 2CaO + 4ZrO_2 \rightarrow Ca_4Al_6O_{12}(SO_4) + 2Ca_2[SiO_4] + 4CaZrO_3$ E.q 2-2

The $C_3A_3.CaSO_4$ phase is stable up to temperature of 1350ºC. The $CaZrO_3$ is the result of the chemical reaction between the zirconia from the MSpII brick and the CaO from the hot kiln feed. The phases identified with XRD from the reactions between components of the Portland clinker and of basic bricks at 1300ºC were calcium aluminate ($C_{12}A$), calcium sulphate aluminate ($Ca_4Al_6O_{12}(SO_4)$ or $C_3A_3.CaSO_4$) and calcium zirconate ($CaZrO_3$). The formation of calcium sulphate aluminate in the samples with the Portland clinker at the temperature of 1300ºC probably occurred due to the reactions between spinel (from the bricks), C_3S, C_3A and SO_3. The products of these reactions, K_2SO_4 and $CaSO_4$, dissolve in the cement phases from the clinker, in the presence of the liquid phase.

The SEM-EDS tests results of the refractory mixture with kiln feed materials indicated that new phases are formed: mayenite ($C_{12}A_7$), calcium alumina-ferrite ($C_2(A, F)$), calcium sulphate aluminate ($C_3A_3.CaSO_4$) and the quaternary Ca_6Al_8 (Mg, Fe) SiO_{23} phase. The corrosion reaction proceeded in the presence of the liquid phase. The formation of $C_3A_3.CaSO_4$ phase could proceed in the same way as the chemical corrosion reaction (Eq. 2-1).

The Ca_6Al_8 (Mg, Fe) SiO_{23} phase was also a new phase found in the SEM-EDS test results between refractory mixture and Portland clinker. The presence of this phase was probably due to the higher temperature dissociation of Fe_2O_3 under low oxygen partial pressure. The Ca_6Al_8 (Mg, Fe) SiO_{23} that incongruently melted at the temperature of 1380ºC was also found in the post-mortem magnesia-spinel bricks.

The high-refractory calcium zirconate and the calcium zirconium aluminate $Ca_7Al_6ZrO_{18}$ (C_7A_3Z) could be formed in the magnesia-spinel bricks as the reaction products with the hot kiln feed and Portland clinker. It was described as a new phase in the magnesia-spinel brick with the ZrO_2 oxide.

Szczerba (2010) summarised that the new phases in the tested bricks are calcium sulphate aluminate, binary, ternary and quaternary phases of calcium aluminates and calcium alumina-ferrites and silicates phases. The formation of the calcium sulphate aluminate ($C_3A_3.CaSO_4$) was due to the presence of sulphur in the hot meal and Portland clinker. The formation of the quaternary phase of the calcium alumina-ferrites (C_6A_4 (M, f) S) was due to a dissociation of the iron oxide (Fe_2O_3) at a higher temperature and low partial pressure of oxygen. The formation of the new phases in the sample with the magnesia-zirconia bricks are clinker phases (β-C_2S, C_3A and C_2 (A, F) / C_4AF) and C_7A_3Z phase. The $CaZrO_3$ and C_7A_3Z phases were formed by chemical reaction between the zirconia from the bricks and the CaO from the cement kiln

materials. The presence of zirconia in magnesia-spinel bricks determined the formation of high-refractory $CaZrO_3$ phase and aluminate $Ca_7Al_6ZrO_{18}$ phase.

2.5.4 High-temperature chemical corrosion.

Potgieter et al. (2004) studied high-temperature chemical corrosion in the short and long kilns. The XRF analysis showed higher concentration of sulphur in the short kiln. This indicates that the corrosion that took place was sulphur dominant. The long dry kiln analysis showed a higher concentration of chloride and potassium which points to a chlorine type of attack of the kiln shell. The EDX spectra of each corrosion scale (Figure 2-1 and 2-2) confirmed the analysis from XRF. The X-ray map images of the individual elements indicated high levels of K and Cl with respect to other elements.

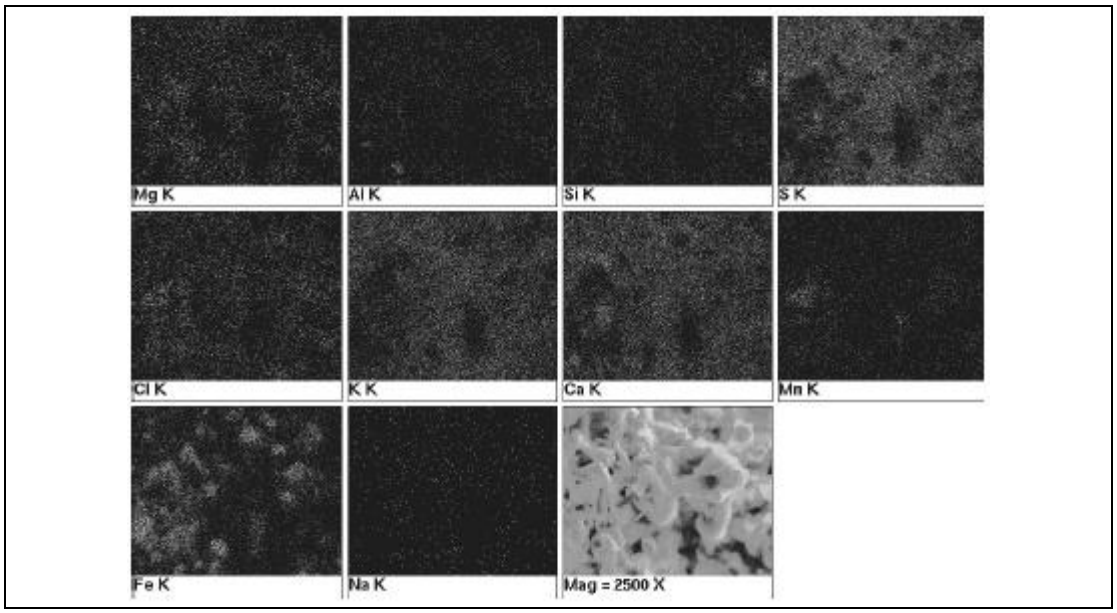


Figure 2-2. X-ray maps of corrosion scale from case 1 kiln

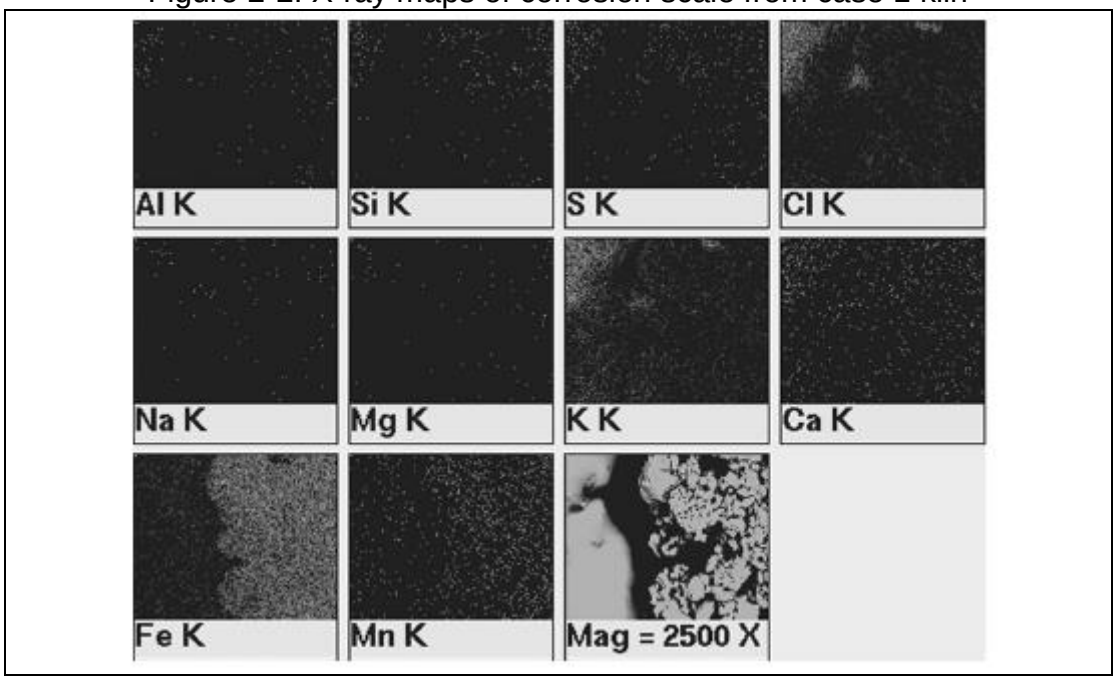


Figure 2-3. X-ray maps of corrosion scale from case 2 kiln

XRD results from the short kiln revealed the presence of various sulphur compounds. A further microscopic examination of the piece showed a tiny KCl crystal along the fissure boundaries. Sulphur from fuel can react in the oxidizing

atmosphere of the kiln to produce acidic gases according to the following reactions:

$\frac{1}{2}S_2$ (g) + O_2 (g) → SO_2 (g) E.q 2-3

SO_2 (g) + $\frac{1}{2}O_2$ (g) → SO_3 (g) E.q 2-4

In the oxygen-restricted environment between the refractory lining and the kiln shell, it is conceivable that SO_2 and SO_3 can act as the oxygen donors and react with iron according to the following reaction

5Fe (s) + 2SO_2 (g) → Fe_3O_4 (s) + 2FeS (s) E.q 2-5

The study found that there was a chemical reaction between SO_2 and SO_3 and the dolomite component of the refractory bricks in the lining. This was confirmed by the XRD results which showed $CaSO_4$ phase. The observed corrosion product could be explained by an access of sulphur oxides present in the kiln atmosphere and their penetration through the refractory lining.

The XRD results for the long kiln indicated that the concentration of KCl in the corrosion scale is high. Whereas chlorine gas can react with the kiln shell, the alkali metal oxides K_2O and Na_2O cannot. The alkalis can only penetrate the refractory brick lining as part of a potassium-salt or sodium-salt melt. The formation of corrosion product KCl was caused by the hot corrosion where a liquid phase normally takes part in the corrosion reaction. The chlorine build-up

in the kiln seems to be the main culprit which causes the observed corrosion in the kiln.

2.5.5 The wear phenomena of refractory linings in the burning zone

Kunnecke (1998) described the chemical wear resulting from gaseous alkali salt compounds that migrate into the bricks and filling the brick pores. Consequently the bricks will increase in volume. This phenomena could be caused by the deposits of mainly K_2SO_4 in lower transition zone and burning zone, along with KCl in the upper transition zone. It was also reported that this wear problem could be resolved by reducing the alkali salt content and balancing alkali / sulphate ratio (refer to appendix C) in the recommended range of 0.8 – 1.2 (Kunnecke, 1998).

2.5.6 The refractories corrosion in cement rotary kilns fired with waste fuels

Bartha and Sodje (2001) reported that the common reason for the degeneration of the refractory lining is the complex influence of alkalis, metal compounds and SO_2/SO_3, Cl_2 and CO_2/CO. These conclusions were based on the results of comprehensive post mortem analyses of refractory materials carried out in the various zones of modern cement kilns using waste materials for firing. The formation of mineral phases and their influence on the degradation of the refractory lining where then studied.

The infiltration by alkali and alkali-earth salts and trace elements in the refractory lining were found to be influenced by prevailing temperatures, oxygen partial pressure, and especially alkali sulphate ratio in the various zones in the kiln. The alkali salts are in a balanced ratio when the ASR value = 1 (recommended 0.8-1.2), ASR value > 1 when there is excess of alkali and ASR value < 1 when there is excess of SO_2/SO_3 (Bartha and Sodje, 2001).

In the case of balanced ASR, alkali sulphate reacts in kiln gas atmosphere to form alkali chloride and alkali sulphate salts, which are bonded in the clinker or infiltrate into the brickwork.

Under oxidising conditions, excessive alkali in the kiln atmosphere leads to reaction of the refractory materials forming alkali sulphates. The formation of these sulphates is accompanied by a significant volume increase (up to 30%) in the refractory which results in structural weakening of the brick hot face.

Excessive sulphur oxides in the kiln atmosphere could promote the occurrence of alkali sulphate and alkali chloride salt filtration and the remaining free sulphate oxides can react either with the clinker or the components of the brick lining. In the case of dolomite bricks, CaO (one main component of the brick grade) is reformed into $CaSO_4$ or CaS. These reactions are accompanied with an increase in volume, leading to weakening of the physical properties of the affected brick horizons (brick phase), and finally to a destruction of the brick texture.

The CaO-containing silicates, in low concentrations in basic brick grades, react with SO_2/SO_3 to form lower melting silicates, such as merwinite (C_3MS_2) and monticellite (CMS). Consequently the magnesia of the brick is also corroded. Under the influence of continued SO_2/SO_3 attack, the formation of forsterite (M_2S) can additionally occur. As a result, sulphate salt $CaSO_4$ is formed, densifying the brick structure in deeper brick horizons (brick phase). The silicate corrosion leads to a weakening of the refractory brick, compromising its refractoriness and structural flexibility.

2.5.7 Conclusion

Szczerba (2010) concluded that the application of alternative, rich in sulphur fuels in the cement kilns intensifies the chemical corrosion of the spinel phase in basic refractories. It leads to the creation of low-melting aluminate phases ($Ca_{12}Al_{14}O_{21}$, $Ca_3Al_2O_6$, Ca_6Al_8 (Mg, Fe) SiO_{23} or $Ca_{20}Al_{26}Mg_3SiO_{68}$ and calcium sulphate aluminate $Ca_4Al_6O_{12}$ (SO_4). The presence of ZrO_2 and $CaZrO_3$ in magnesia refractory materials should improve their resistance to chemical corrosion by cement clinker materials.

Potgieter et al. (2004) established that the practice of recirculating kiln dust with high alkali content from the electrostatic precipitators, the composition of the raw materials and the type of refractory brick used could all potentially have contributed to the corrosion that occurred. Then the use of the dense brick was

recommended in order to resist infiltration by aggressive chemical species could be the solution. Magnesia-zirconia bricks could also be considered since this refractory brick type has good resistance to corrosion by alkali salts.

2.6 Thermal shock of refractory materials

2.6.1 Introduction

The thermal shock behaviour of magnesia-spinel refractory materials were extensively investigated by Ghosh et al. (2004); Aksel et al. (2004a); Aksel et al. (2004b) and Riley et al. (2002).

2.6.2 Sample preparation and thermal shock analysis

Ghosh et al. (2004) studied the thermal shock behaviour of a spinel prepared from stoichiometrically mixing calcined magnesia and alumina. The spinel was further mixed with the sintered magnesia for brick making. The batches of magnesia containing 0, 10, 20 and 30 wt. % spinel mixture were then prepared and fired at optimum temperature (sintering). The sintered products were characterized by linear thermal expansion up to 1400 ºC, cold strength (as modulus of rupture: MOR), refractoriness under load (RUL), hot strength (as MOR) at different temperatures (1000, 1200 and 1400 ºC) and retainment of cold MOR after thermal shock. The chemical and mineral compositions of sintered products were respectively analysed using the scanning electron

microscopy and XRD technique. All firing processes were performed in an electrically heated programmable furnace.

Aksel et al. (2004a) prepared different batches of MgO with 10, 20, 30 wt. % of spinel content, which were hot-pressed at optimum pressure and temperature to produce discs. The discs were then cut into bars which were characterized by strength and Young's modulus measurement, fracture toughness and work of fracture measurement and fractography by SEM-EDX. Secondary electron images were used to indicate the size and shape of grains exposed in fracture surfaces, back scattered electron images were used to indicate the presence and position of spinel particles.

Aksel et al. (2004b) also studied the thermal shock resistance based on a set of dense magnesia–spinel composites of systematically varied spinel particle size and loading. The set of thermal shock resistance parameters, *R* and *R'''*, were used and expresses the conditions for failure by crack initiation. These parameters are defined:

$R = \frac{\sigma_f(1-v)}{E\alpha}$ and $R''' = \frac{E}{\{\sigma(1-v)\}}$

Where v = Poisson ratio, α = mean thermal expansion, E = elastic modulus and σ = infinite surface stress.

R defines the minimum temperature difference to produce fracture and *R'''* expresses the degree of thermal shock damage in materials with similar crack propagation properties, that is, similar values of work of fracture (γ_{wof}).

These parameters were assessed for the prediction of the behaviour under thermal shock. Parameter *(R)* relates to the instantaneous temperature difference ΔT required to create a stress equal to the strength of the material, when failure would be expected to occur. While parameters *(R''')* is applicable to the case of severe thermal environments, where the thermal stress fracture cannot be avoided and the major requirement is to minimize the extent of crack propagation. The examination of the materials was conducted through optical microscopy for surface cracks and SEM for fracture faces.

Riley et al. (2002) prepared MgO-spinel mixtures by mixing together pure MgO materials with 5, 10, 20 and 30 % by weight of spinel. After blending, firing and densification, discs were produced and cut into bars for tests. This study consisted of measurements of bend strength, Young's modulus and fracture toughness. Grain boundaries were examined by SEM and mean grain size was calculated using standard mean intercept method from photographs of samples. Secondary electron images were used to examine the size and shape of grain exposed in fracture surfaces and back scattered images were used to identify the presence and position of spinel particles.

2.6.3 The effect of spinel content on the properties of magnesia-spinel composite.

Ghosh et al. (2004) showed a gradual reduction of the thermal expansion value with increasing amount of spinel. This is due to the much lower thermal expansion behaviour of spinel phase than magnesia. For instance, an addition of 30 wt. % spinel in the pure MgO material resulted in a decrease in thermal expansion from 1.66 % to 1.36 % at 1400 ºC.

RUL results showed that the addition of spinel to the pure MgO material greatly improves the RUL values. The optimum spinel addition was found to be 20 wt. %. Further addition of spinel did not improve RUL. The addition of spinel into the magnesia replaces fine grains of magnesia which reduce the chances of low melting phase of impurities diffusing through the magnesia. The spinel addition therefore reduces the probability of deterioration of the magnesia brick and increases its strength against deformation. Thermal expansion discrepancy between magnesia and spinel phases results in microcracking in the body that helps to restrict the crack propagation by interlinking during failure. The extent of microcracking enhances with higher amounts of spinel. The addition of 30 wt. % spinel resulted in higher extent of microcracking which starts reducing the strength of the refractory due to the propagation of the existing cracks present in large numbers. Whilst the addition of 20 wt. % spinel enhanced the properties

of the refractory, in addition, spinel can also absorb Fe_2O_3 into its structure (Ghosh et al., 2004).

It was also found that retained strength after thermal shock and cold strength (MOR) of the batches nearly have similar strength values for refractory materials containing up to 20 wt. % spinel (Ghosh et al., 2004). The magnesia refractory without spinel showed a drastic fall in strength value after thermal shock. The presence of impurities in the periclase (MgO) might have resulted in the formation of a viscous phase during sintering at higher temperature and cracks during the thermal shock, resulting in poor retained strength capacity. The addition of spinel greatly improves the retained strength value. Microcracks present in the spinel containing batches prevent the propagation of crack generated during thermal shock, strengthening the body and increasing the retained strength.

In this study, the periclase grain size was 6 µm and addition of 20 wt. % spinel resulted in periclase grains growth to 18 µm.

2.6.4 Fracture behaviour of magnesia and magnesia-spinel composites.

Aksel et al. (2004b) studied the microstructural changes and fracture behaviour of both pure MgO and MgO–spinel composites, as a function of spinel addition before and after thermal shock testing.

The fracture mechanism in MgO–spinel refractories was based on the development of microcracks that allow easy crack initiation, but make propagation more difficult due to the fracture that occurs in a quasi-static manner (Aksel et al., 2004b).

The microstructure studies found that there was a significant increase in the extent of microcracking with increasing spinel content and also significant changes in the grain size for the different materials (Aksel et al., 2004b). Composites with 10wt % spinel addition commonly showed a smaller amount of microcracking compared to composites with higher spinel content. For instance, longer micro-cracks (both transgranular and intergranular) were observed in the composites containing 20% spinel, and the average MgO grain size was 50 μm. At 30% spinel addition interlinked transgranular and intergranular radial cracks in the MgO matrix appeared. The crack length increased significantly while MgO grain size reduced to 40 μm.

The fractography before thermal shock showed that the fracture is mostly transgranular and changes to intergranular with spinel addition (Aksel et al., 2004b). The presence of spinel particles at the grain boundaries promoted the intergranular fracture. Spinel particles were found to be uniformly located at the grain boundaries and within the MgO grains. In the composites with 30 wt. % spinel addition, the proportion of intergranular fracture increased significantly. The results also showed that the 30 wt. % spinel addition composites had

mostly intergranular fracture after quenching. Hence the higher the spinel content the greater the amount of intergranular fracture (Aksel et al., 2004b).

The addition of spinel also increases the energy required for fracture to occur and results in resistance to crack propagation and further thermal shock damages. The change in fracture path from transgranular to more intergranular fracture at higher spinel addition is likely to be the reason behind the increase in work of fracture values. It was established that more energy will be required for fracture at higher spinel than for lower spinel loadings (Aksel et al., 2004b).

The strength of materials before thermal shock showed that the pure MgO materials have higher strength than the composites. However the results obtained after thermal shock showed a significant percentage drop in strength of the pure MgO than that of the composites with addition of spinel. In the composites with 20% and 30% spinel content, there was no loss of strength. The retained strength dropped at temperatures higher than 600 ºC for the pure MgO materials whereas composites materials showed higher retained strength.

After the test, spinel composites showed high resistance to thermal shock and a slow progressive loss of strength. The 30 % spinel composite showed the highest retained strength after thermal shock.

2.6.5 Thermal shock behaviour of magnesia-spinel composites.

Aksel et al., 2004a also studied the fracture behaviour of magnesia and magnesia-spinel composite before and after thermal shock. The SEM analysis showed that the composites were extensively microcracked. The cracks were predominately intergranular. In general, cracking is described as grain boundary separation. The larger spinel particles appeared to have a major function of providing the connectivity between MgO grains. Microcracks generation was attributed to the large difference in thermal expansion coefficient between MgO and spinel, coupled with strong tendency for the small spinel crystals to be precipitated at MgO-MgO grain boundaries. Fracture in the composites predominantly followed grain boundaries.

This study found that it is more reasonable to view the system of the present set of materials from the standpoint of the enhancement of damage by stable, slow, crack propagation (Aksel et al., 2004a). The R''' parameters indicated that there should be reduced thermal shock damage compared with that in pure MgO. The R''' parameters increased steadily with increasing spinel loading, and the largest spinel particles have the greatest effect. The best material in this set would be that containing 20% of 22 μm spinel. It is clear that the effect is directly proportional to spinel loading, and the larger the spinel particles, the better.

The work of fracture showed that there was an increase by 50% on the work of fracture values of the composites materials in comparison to the pure MgO.

However the work of fracture values was not sensitive to spinel loadings and particle size.

The Young's modulus test showed that pure MgO will have higher strength until the critical quench temperature (T_{qc}) of 600 ºC where there is an abrupt drop in strength. However the composite materials steadily loose the strength with increasing quench temperature with the stronger composite materials being the most influenced.

Fracture surfaces of pure MgO quenched at temperature T < 575 ºC showed a higher proportion of transgranular cracks formed by grain cleavage. Low magnification observation aided by the use of dye penetrant on polished faces showed no large scale of cracking. At a quenching temperature (T_q) of 575 ºC there was a small increase in the proportion of intergranular fracture. At the critical quench temperature of 625 ºC, however, there was a marked change in the appearance of the fracture surface, which now contained a high proportion of facetted grains produced by intergranular cracking. At quenching temperatures higher than T_{qc} more extended cracks were evident. There was no detectable major cracks in the 20% 22 µm composite for T_q < 600 ºC. For higher temperatures (T_q > 600 ºC), crack density increased with increasing T_q. However new cracks appeared not to have extended even at T_q. The distance of crack penetration remained small, consistent with the small reductions seen in strength.

2.6.6 The mechanical properties of magnesia-spinel composites

Riley et al. (2002) studied the mechanical properties of magnesia-spinel composites. It was found that MgO grain size is dependent on spinel additions and particle size. The MgO grain size increased with the spinel additions of 5 – 10%. Further addition of spinel (> 10%) resulted in the reduction of MgO particle size as it was observed in the case of pure MgO.

This study found that the bend strength of composite uniformly decreases with increasing spinel content and spinel particle size. The Young's modulus (*E*) showed similar general trend to that of strength.

The observed changes in composite strength with increasing spinel loading and particle size are consistent with the generation of microcracks. These microcracks are the result of the large thermal expansion discrepancy between the MgO matrix grains and spinel particles. The microcracking becomes more extensive at higher spinel content.

Fracture faces of pure MgO showed pronounced transgranular fracture (see figure 2-4), with clear grain faceting. Meanwhile composites showed a significant tendency towards intergranular fracture, which is more noticeable with higher spinel additions (see figure 2-5).

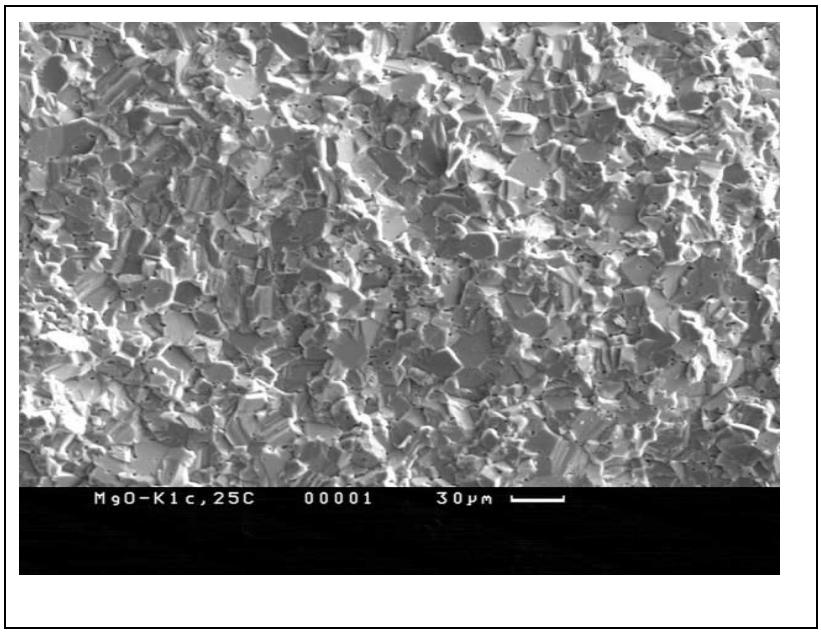


Figure 2-4. SEM photograph of a fracture face of pure MgO, showing pronounced transgranular fracture.

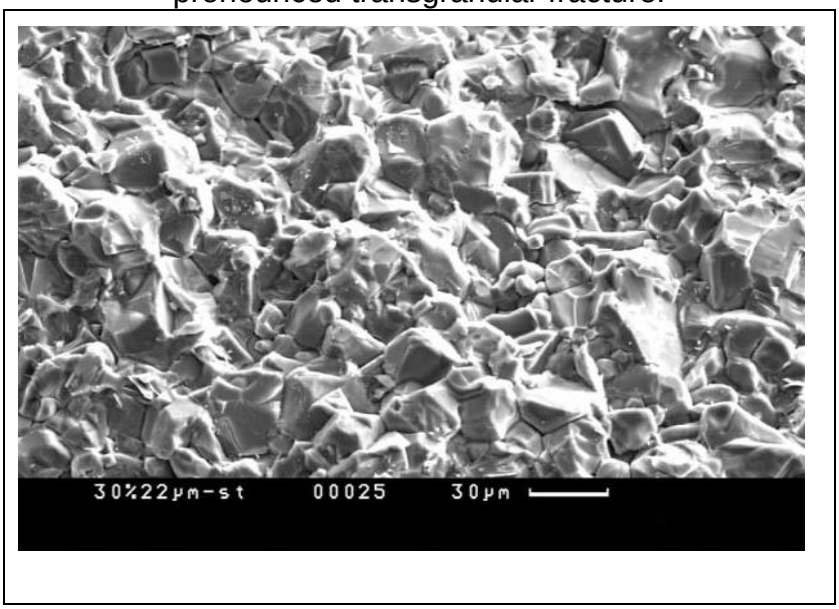


Figure 2-5. SEM photograph of a fracture face of 20% 22 µm spinel composites, showing predominantly intergranular fracture.

The decrease in strength of the spinel composites is therefore, more likely to be related to a decrease of fracture toughness with decreasing Young's modulus and fracture energy.

This study also showed that the stress generation is a result of thermal expansion disparity between the matrix and included particles. Further analysis was done on the stress generation in a glass matrix that contains crystalline particles. It was found that the absolute stress at a given distance from the spinel particle increases with an increase in the particle size. Intergranular cracks would thus be likely to interlink under these conditions, to form a network of sharp intergranular cracks. The continued decrease in strength at higher spinel loadings may be attributed to crack lengthening, by linking and propagation across MgO grains.

2.6.7 Conclusion

Ghosh et al. (2004) concluded that there is a gradual decrease in thermal expansion of the periclase with an increase in spinel content up to 20 wt. %. The addition of spinel greatly improved the refractoriness under load, retained strength after thermal shock and hot modulus of rupture characteristics for the periclase body. The microstructure showed spinel as intergranular particles in between the periclase grains as well as the exsolved phase on the periclase grains. Spinel addition also caused significant growth for the periclase grains.

The addition of 20 wt. % spinel showed superior properties whilst 30 wt. % spinel addition showed relatively lower mechanical/thermo-mechanical properties due to the large extent of microcracking, which causes extension/propagation of existing microcracks in the body at a relatively lower stress level.

Aksel et al. (2004b) concluded that the higher the spinel content, the greater the crack length occurred due to the discrepancy of thermal expansion between MgO and spinel. At 30 % spinel loading, a large number of interlinked cracks in the MgO matrix appeared, and the critical crack length increased significantly. Intergranular fracture along the smaller MgO grains at higher spinel loading, required much more energy for fracture than that for lower spinel loading, indicating higher work of fracture values. The fracture analysis of pure MgO was found to be mostly transgranular while a large proportion of intergranular fracture was observed on the MgO materials with spinel content. The intergranular fracture of the MgO materials increased with an increase in spinel content. In composites with higher spinel content, the change in fracture path from transgranular to more intergranular fracture was described as the main reason for an increase in work of fracture energy. Pre-existing connected cracks appeared not to be able to propagate easily in the 20 % and 30 % spinel materials. For this reason more energy was required to connect the cracks for propagation after thermal quenching. Therefore, the cracks propagate only a

short distance and become arrested. The composite containing 30 % spinel in general showed the greatest resistance to crack propagation, and to further thermal shock damage.

Aksel et al. (2004a) also established that the critical quench temperature of the pure dense MgO is 600 º C. Above this temperature, strength and Young modulus fell brusquely to 20 % of the as-sintered values. The existing microcracks weakened MgO-spinel composites which progressively lost strength and Young's modulus with increasing quench temperature. There was no critical quench temperature for the composites materials. The composite materials generally had a much higher proportion of retained strength after thermal shock than pure MgO. The composites formed with coarse spinel particles had better resistance to thermal shock damage than those formed with fine particles. Spinel loading improved thermal shock characteristics, however no benefit was evident for more spinel addition (> 30 % spinel). This study found the smallest relative loss of strength on quenching by the addition of 20 % of 22 µm spinel. The improved resistance to thermal shock damage of the microcracked MgO-spinel composites was attributed to the increased difficulty of developing the strain energy required to propagate the thermal expansion.

Riley et al. (2002) also concluded that microcracking and grain boundary separation with origins at the MgO-spinel interface occurs in these dense MgO composite materials. This is due to the thermal expansion mismatch between

the two phases and the crystallization of secondary spinel during cooling. These cracks are the critical defects that cause failure on loadings. The loss of strength and Young's modulus are more significant when the spinel particles are larger because of the increased extent of the local tensile stress field. Crack interlinking is favoured at high spinel loadings, when inter-spinel particle distances become much smaller than the MgO grain size.

2.7 The effect of partial pressure of oxygen or CO_2/CO gas mixtures

2.7.1 Introduction

At a given temperature and standard pressure (ambient; 1 atm), the stability of a pure metal and oxide depends on the partial pressure of oxygen or CO_2/CO ratio in the atmosphere. If the two phases (metal/metal oxide or metal suboxide/metal oxide) are in equilibrium, the incumbent oxygen partial pressure is recognized as the equilibrium partial pressure. According to the Gibbs phase rule, on either side of this unique oxygen partial pressure, at a given temperature, one of the two coexisting phases must disappear (Azad, 2006).

The oxygen partial pressure in the vicinity of two phases can also be determined by the CO_2/CO ratio in a buffer mixture. At equilibrium, oxygen partial pressure can be related to the ratio of CO_2/CO using the following equations:

$$CO + \frac{1}{2}O_2 = CO_2$$ E.q 2-6

For which:

$$\Delta G° = -RTln\frac{PCO_2}{PCOPO_2{}^{½}}$$ E.q 2-7

This gives:

$$PO_2 = \left(\frac{PCO_2}{PCO}\right)^2 \frac{1}{e^{-2\Delta G°/RT}}$$ E.q 2-8

where $\Delta G° (J)$ according to Azad (2006) is expressed as follows:

$$\Delta G° (J) = -282{,}400 + 86.81T$$ E.q 2-9

The equation 2.6 can be rewritten as follows:

$$2CO_{(g)} + O_{2(g)} = 2CO_{2(g)}$$ E.q 2-10

For this reaction, the equilibrium constant K is:

$$K = \frac{P^2CO_2}{P^2COPO_2}$$ E.q 2-11

In practice, the stability of a metal or oxide is studied by considering three chemical reactions of oxidation: metal into metal oxide, carbon into carbon monoxide and carbon into carbon dioxide and transformation of CO into CO_2. The oxygen partial pressure and CO_2/CO ratio (at equilibrium) can then be determined by using thermodynamic calculations. As with any chemical

reaction prediction based on purely thermodynamic grounds, the oxide with the more negative ΔG will be formed and the one with less ΔG will be reduced.

In this study, the stability of oxides (Fe_3O_4 and Mn_3O_4) will be investigated as they are significantly involved in the reactions between clinker and refractory materials.

Hayes (2003) reported that a large number of oxides can be readily reduced in CO_2/CO gas mixture. Stable oxides can be reduced by either solid carbon or another metal corresponding to more stable oxides (For instance Al and Si).

2.7.2 Stability of Fe_2O_3 and Mn_2O_3

The most commonly used iron ore is in the form of hematite, Fe_2O_3. In the presence of CO_2/CO mixtures, this oxide may be reduced to iron in a number of stages. Similarly manganese oxide, Mn_2O_3 can also be reduced in CO_2/CO gas mixture. For each oxide, reaction temperature and a critical CO_2/CO ratio in the gas mixture must be exceeded before the reduction reaction proceeds.

Hayes (2003) showed that the carbon monoxide gas generated in the blast furnace acts as a reducing agent that captures oxygen from metal oxides. Each of the reducing steps takes place in a different part of the furnace and at different temperatures. Typically the reduction of Fe_2O_3 and Fe_3O_4 occurs between 200 – 250°C, and a minimum CO_2/CO ratio of approximately $\frac{1}{10^4}$ is

required. Fe_3O_4 is reduced to FeO between 500 - 900°C, FeO is reduced to Fe at temperatures between 900 - 1300°C.

2.7.3 Redox burning conditions

Bartha and Sodje (2001) found that magnesioferrite ($MgFe^{3+}{}_2O_4$), contained in the alpine magnesia brick, is reduced to magnesiowusite ((Mg, Fe^{2+}) O) and this involves a significant reduction of volume (>20%). If redox burning cycles occur, there are frequent changes between magnesioferrite and magnesiowusite, resulting in the structural weakening of the affected brick horizons. This can lead to a premature wear as a result of spallings of the redox-subjected brick horizons. If additional infiltrated sulphate salts are present in the structures of the refractory lining, and particularly under the influence of sulphur excess, sulphide compounds can form from these under strongly reducing conditions. The sulphides of K_2S, oldhamite (CaS), K_2S_3, $KFeS_2$ were determined in analysed used brick samples. When oxidizing conditions predominate again, an oxidation of the sulphides takes place, accompanied by a significant volume increase. This leads to expansion of the brick structure resulting in the destruction of the brick.

Bartha and Sodje (2001) gave examples of reaction equations in burning conditions of the rotary cement kilns as follows:

Reducing burning conditions:

$$MgO.Fe_2O_3 + CO = MgO + 2FeO + CO_2$$ E.q 2-12

$$K_2SO_4 + 4CO = K_2S + 4CO_2$$ E.q 2-13

$$K_2SO_4 + 8CO + 2SO_2 = K_2S_3 + 8CO_2$$ E.q 2-14

$$MgFe_2O_4 + K_2SO_4 + 13CO + 3SO_2 =$$

$$2KFeS_2 + MgO + 13CO_2$$ E.q 2-15

Oxidising burning conditions

$$MgO.2FeO + \frac{1}{2}O_2 = MgO.Fe_2O_3$$ E.q 2-16

$$2KFeS_2 + 8O_2 = K_2SO_4 + Fe_2(SO_4)_3$$ E.q 2-17

CHAPTER THREE

3 EXPERIMENTAL PROCEDURE

This chapter details the materials, sample preparations, data collection and analytical methods used in this study. Computational thermochemistry which was used to construct phase diagrams is also discussed. The sampling and examination procedure summary are schematically shown in Figure 3-1.

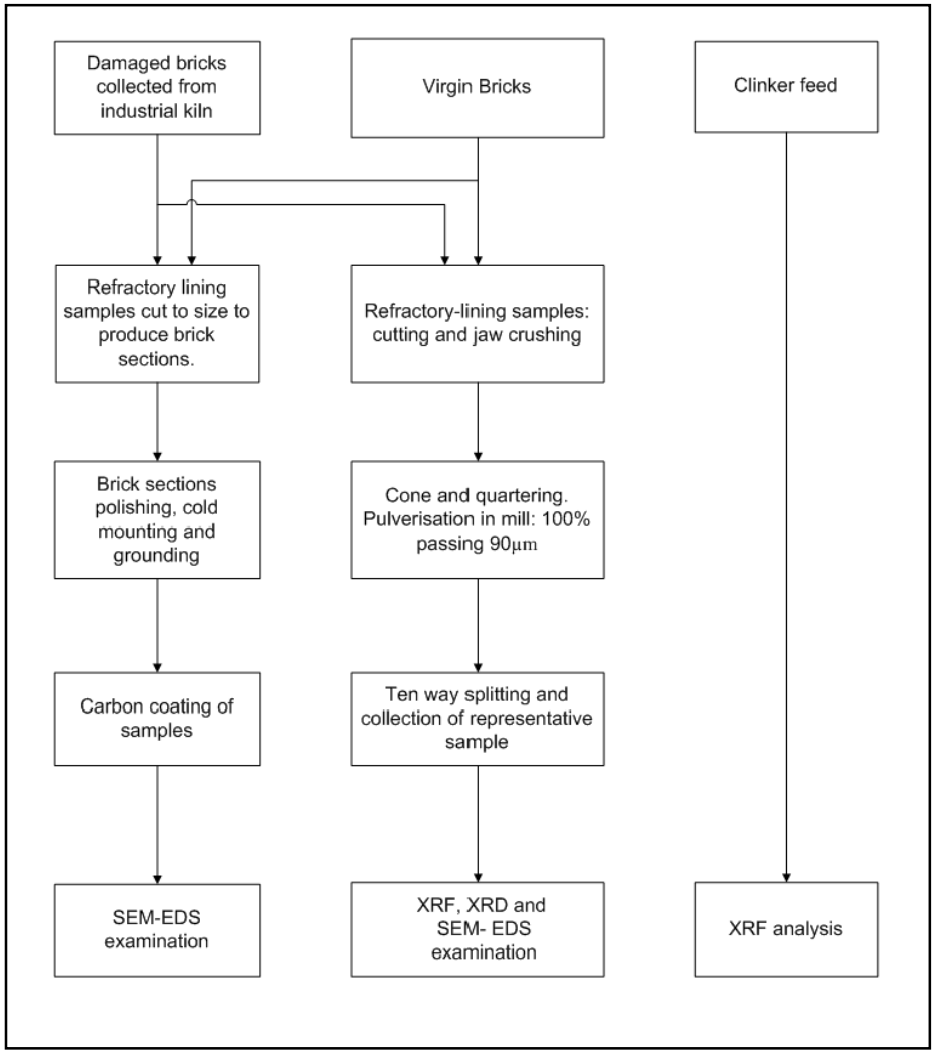


Figure 3-1 Experimental procedure for sample preparation and analysis

3.1 Materials

Three types of sample were collected: the unused refractory lining, used or damaged refractory lining from the industrial kiln and kiln feed materials. The used and unused samples comprised of magnesia and alumina bricks which were applied in the burning and lower transition zone of the industrial kiln.

3.1.1 The unused brick

The unused bricks comprised of magnesia-spinel, magnesia-fused spinel and high-alumina. These materials were made available by AfriSam (Ulco cement plant, South Africa) and were used as received from the supplier.

3.1.2 The used (damaged) brick

The used or damaged samples were collected from an industrial kiln (AfriSam - Ulco cement plant, South Africa). These brick samples consisted of magnesia-spinel bricks collected from burning zone and high-alumina bricks collected from lower transition zone.

Each brick sample was collected in each row of the respective zone in order to get representative sample (see Figure 3-2). These samples were collected after failure in the industrial kiln. The representative used samples were collected over a period of a year from January 2011 to December 2011.

3.1.3 The kiln feed

The chemical compositions of the kiln feed, in Table 3-1, consist of data collected over 18 months from January 2010 to June 2011 (see appendix D). The feed was analysed hourly as it enters the kiln for clinker production

Table 3-1 Industrial kiln feed chemical composition

Chemical species	Weight %
SiO_2	21.00
Al_2O_3	3.83
Fe_2O_3	2.67
Mn_2O_3	1.22
CaO	67.32
MgO	2.69
K_2O	0.54
Na_2O	0.47
TiO_2	0.22
SO_3	0.04
Cl	0.02
Total	**100.00**

3.2 The industrial kiln

The industrial kiln in this study has an effective diameter of 3.8 m and a length of 70 m. The kiln rotates at 3.1 revolutions per minute (rpm) and it is inclined at 3°. The residence time of the charge in the kiln is approximately 25 minutes (refer to appendix E) and can be calculated according to Alsop (1998) as follows:

$$T = 11.2\ L / NDS \qquad \text{E.q 3-1}$$

Where T= time in minutes, D = diameter in meters, L = Length in meters, N = revolutions per minute and S = kiln slope in degree.

The kiln reaches a daily production of 4200 tons clinker. The clinker feed and kiln off-gas flow counter-current to each other.

The schematic diagram of the kiln, in Figure 3-2, shows different kiln zones clearly marked. See notes in the diagram.

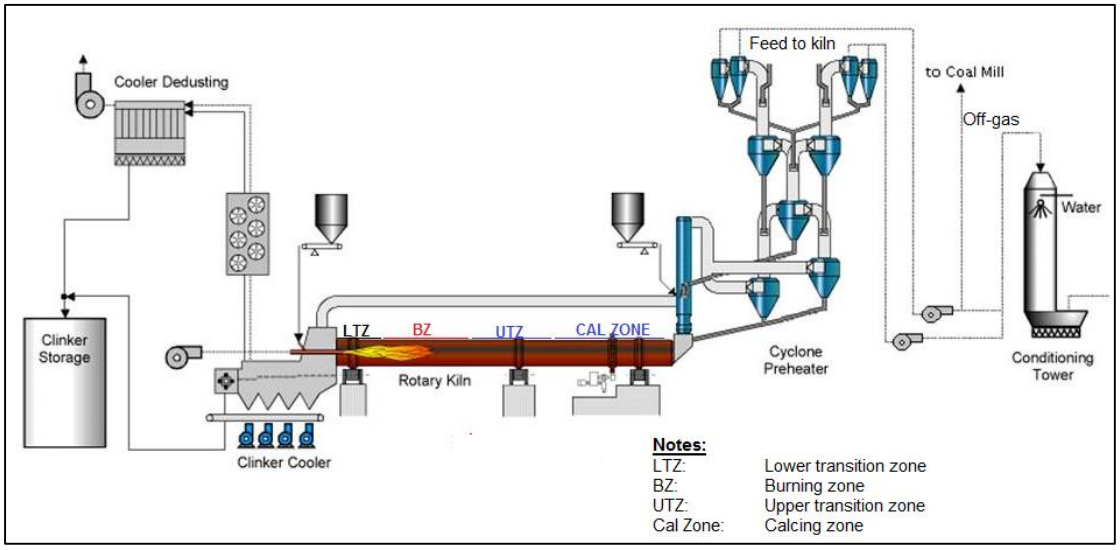


Figure 3-2 Schematic diagram of the kiln

3.3 Sample preparation

Representative brick samples were cut to a predefined size by a diamond blade in order to produce brick sections. The brick sections were then cold mounted and ground (polished) in three steps: 80, 220 and 1200 grit using the diamond discs. Two sets of samples were collected and respectively directed to fracture and chemical analysis. The brick sections for fracture analysis were fractured and analysed under SEM. The second set of brick sections was coated with

carbon to improve their conductivity under the microscope. The scanning electron microscope (SEM) equipped with electron dispersive spectrometry (EDS) was then used for microstructural and quantitative chemical analysis.

Samples of each brick were cut to size and put through the Jaw Crusher. Each of the crushed sample was cone and quartered to get a representative sample, which was pulverized for four minutes in a TS250 (™) mill to 100% passing 90 µm. The pulverized sample was split 10 ways in a riffler to collect representative samples that were then examined by X-ray fluorescence spectrometry (XRF), X-ray diffractometry (XRD) and SEM-EDS analysis. For SEM-EDS analysis the samples were placed on carbon tape and then coated with carbon to enhanced conductivity under the microscope.

3.4 Analytical methods

3.4.1 XRF

The identification and characterization of powder samples for elemental and chemical compositions was carried out by PAnalytical Axios X-ray powder fluorescence spectrometry technique (XRF). This technique was used to determine the chemical compositions of the kiln feed and used and unused refractory lining powder samples. In addition analysis of clinker for alkali sulphate ratio (ASR) values was completed through XRF. The limitation of XRF analysis is its inability to distinguish ions of the same element in different

valence states and hence XRF was used in conjunction with XRD and SEM-EDS techniques.

3.4.2 XRD

The powder samples were prepared for X-ray diffractometry (XRD) analysis using a zero background sample holder or a universal sample holder for solid metal samples. They were analysed with a PAnalytical X'Pert Pro powder diffractometry with X'Celerator detector and variable divergence and fixed receiving slits with Fe filtered Co-K radiation. The phases were identified using X'Pert Highscore plus software. The relative phase amounts (weights %) were estimated using the Rietveld method (Autoquan Program). The limitation of XRD is its inability to detect a small amount of phase in the sample.

3.4.3 SEM-EDS

The Joel JSM 6510 SEM, equipped with NSS software, was used for microstructural and qualitative chemical analysis. The refractory brick section samples were cold mounted and ground (polished) in three steps; 80, 220 and 1200 grit using the diamond discs. The samples were then coated with carbon to improve their conductivity under the microscope.

The powder samples once received were placed on carbon tape and then coated with carbon before analysis. The carbon coating of the refractory

materials limits the accuracy of measuring carbon content on the sample. In addition SEM – EDS technique is unable to measure Li, He and H content.

3.5 Computational thermochemistry (FactSage)

FactSage (EX Mente) computational thermochemistry software was used to predict interactions through phase diagrams systems. It was developed by Thermfact from Canada and GTT-Technologies from Germany. The developed phase diagrams are used to predict the effect of impurities analysed in this study. The thermodynamic predictions of the chemical reactions were performed using the software package FactSage 6.4 with the oxide and salt solutions databases (FToxid and FTsalt). The results shown by XRF, XRD and SEM-EDS analysis were accurately predicted by FactSage which confirms its suitability for this work.

3.6 Carbon monoxide / carbon dioxide (CO_2/CO) measurements

The measurements for CO and CO_2 were carried by heat resistance gas analyser probe. The measurement were taken from kiln feed entry (gas exit point). The values analysed are used for the calculations of partial pressure of oxygen.

3.7 Alkali-sulphate ratio

The clinker was analysed to determine the alkali sulphate values. The data were collected over a period of 17 months (see appendix C). In general, the collection of the samples was associated with the operating conditions where the alkali-sulphate ratio was outside the recommended range of 0.8 – 1.2 (see Figure 3-3). This could have contributed to chemical attack of the cement kiln refractory lining (Bartha and Sodje, 2001).

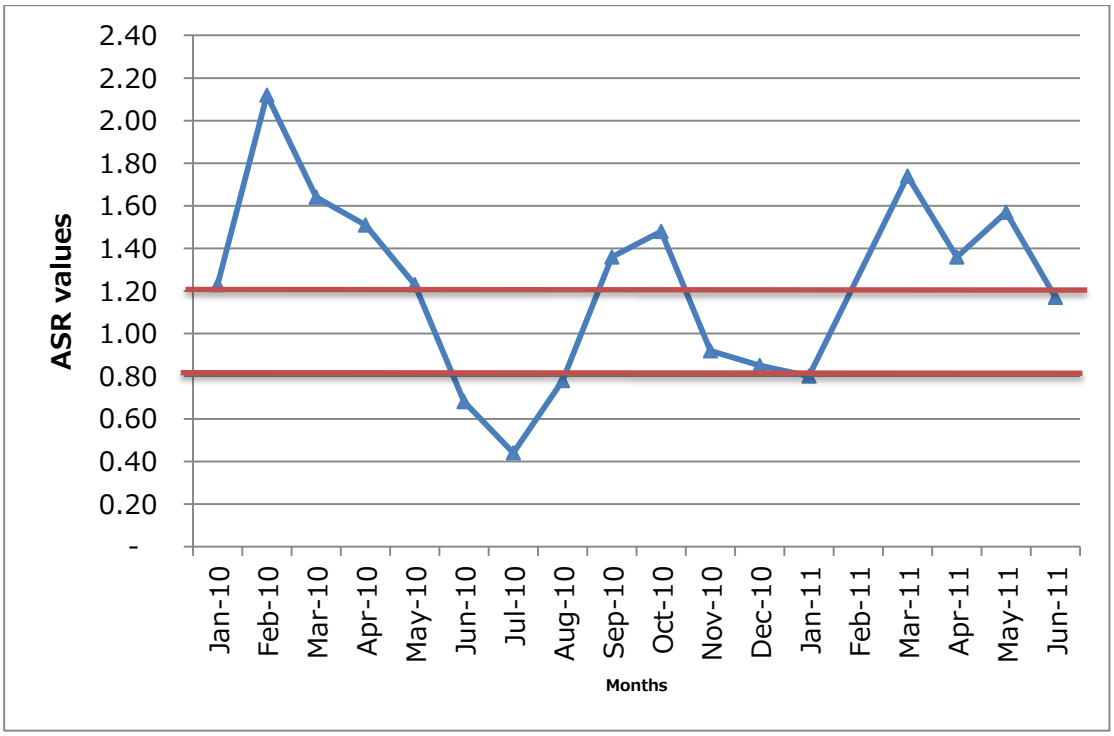


Figure 3-3. ASR of the study kiln

CHAPTER FOUR

4 RESULTS AND DISCUSSION: MAGNESIA BRICKS

4.1 Introduction

The magnesia-spinel brick type A, magnesia-spinel brick type B and magnesia-fused spinel were all applied at the burning zone of the rotary cement kiln. Analytical methods such as XRF, XRD, SEM-EDS and computational thermochemistry (phase diagrams) were used to establish the failure mechanism of the refractory lining.

4.2 Chemical analysis of the magnesia refractory lining

The data, in Table 4-1 and 4-2, represent the chemical analysis of the virgin and damaged magnesia refractory lining. It can be seen that major contaminating species in damaged lining are K_2O, Cl, SO_3, and Na_2O. In terms of chemical elements, K, Cl, S and Na are identified as the major impurities in the damaged bricks. These elements can be clearly observed in the SEM-EDS mapping of the powder sample made from each refractory brick lining (Figure 4-1, 4-2 and 4-3). However, Cl is absent in magnesia-spinel brick type B (Table 4-2 and Figure 4-2).

Based on XRD results (Table 4-3), the main phases are periclase (MgO) and spinel ($MgFe_{0.2}Al_{1.8}O_4$). Spinel phase contains MgO, Fe_2O_3 and Al_2O_3.

Table 4-1. Chemical compositions of virgin and damaged magnesia brick, based on XRF assay

Chemical species	Chemical composition (weight %).					
	Magnesia-spinel brick type A		Magnesia-spinel brick type B		Magnesia-fused spinel	
	virgin	damaged	virgin	damaged	virgin	damaged
SiO_2	0.48	0.43	0.67	0.68	1.07	0.98
Al_2O_3	16.05	14.36	14.07	15.93	18.22	16.73
Fe_2O_3	0.49	0.52	0.43	0.71	0.67	0.61
CaO	5.30	6.30	0.90	1.14	1.26	1.20
MgO	77.68	73.42	83.78	78.24	78.79	78.57
Mn_2O_3	-	0.09	0.15	0.15	-	-
SO_3	-	0.87	-	0.86	-	0.35
Na_2O	-	0.53	-	0.33	-	0.34
Cl	-	0.99	-	-	-	0.14
K_2O	-	2.49	-	1.96	-	1.08
Total	**100.00**	**100.00**	**100.00**	**100.00**	**100.00**	**100.00**

Table 4-2. Elemental composition of virgin and damaged magnesia powder sample, based on SEM-EDS analysis

Chemical composition (weight %).						
Elements	**Magnesia-spinel brick type A**		**Magnesia-spinel brick type B**		**Magnesia-fused spinel**	
	virgin	**damaged**	**virgin**	**damaged**	**virgin**	**damaged**
O	39.78	39.54	40.60	43.37	44.01	44.89
Mg	55.37	31.95	50.63	26.64	46.89	32.98
Al	1.90	1.39	5.34	4.36	4.06	4.03
Si	0.27	0.53	0.52	0.52	0.88	0.86
Ca	1.87	4.84	2.24	2.86	3.37	4.03
Mn	0.14	-	0.10	0.21	0.79	0.94
Fe	0.67	0.58	0.57	0.80		9.38
K		8.70		15.68		0.47
Cl		8.40				0.06
Na		0.46				2.36
S		3.56		5.56		
F		0.04				
Total	**100.00**	**100.00**	**100.00**	**100.00**	**100.00**	**100.00**

In the SEM-EDS figure 4-1 to 4-3 provided below, the captions a and b represents: a) Powder sample showing particle morphology, and b) Elemental mapping showing the presence of main elements.

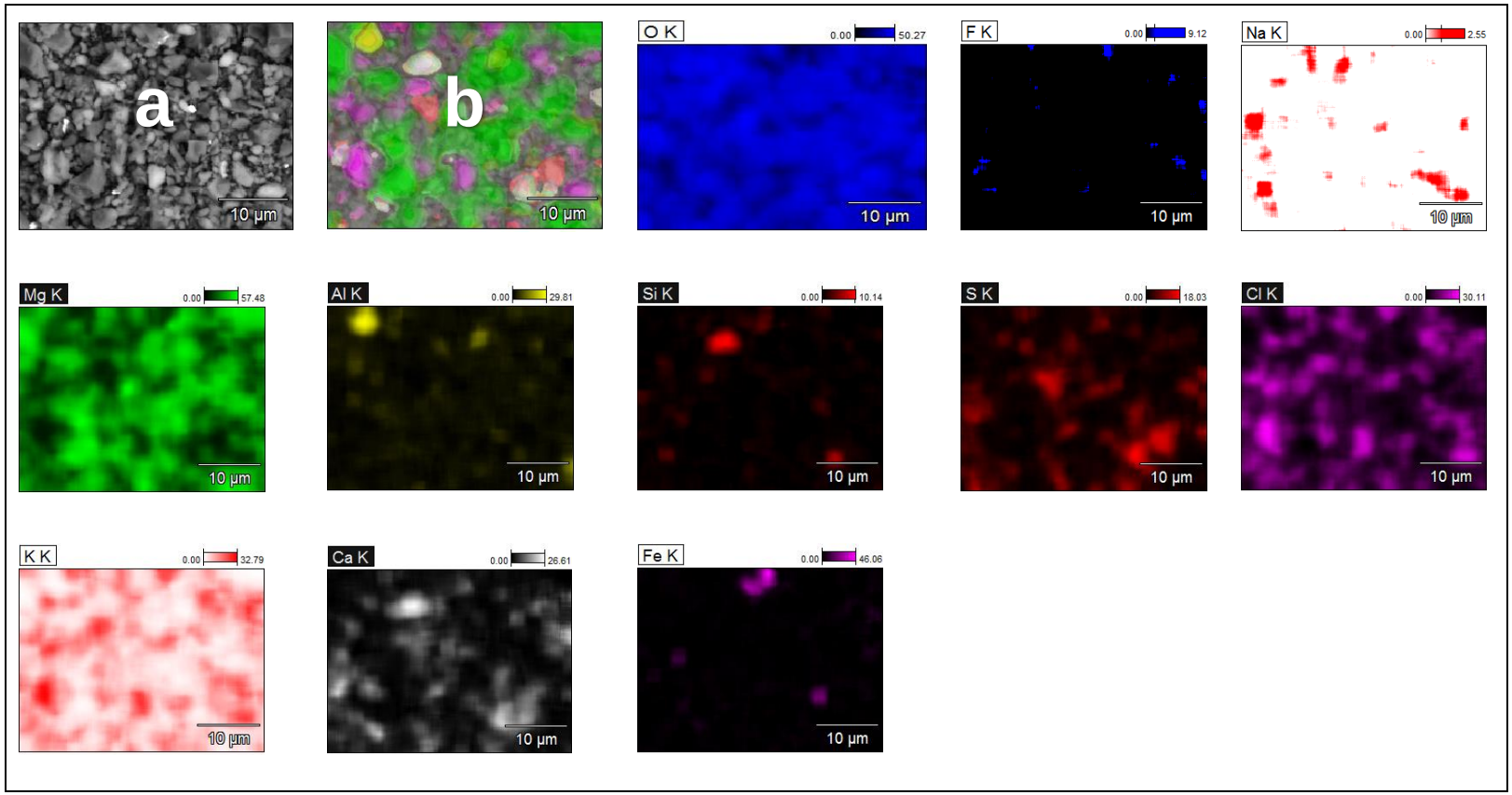


Figure 4-1. SEM-EDS mapping of magnesia-spinel brick type A

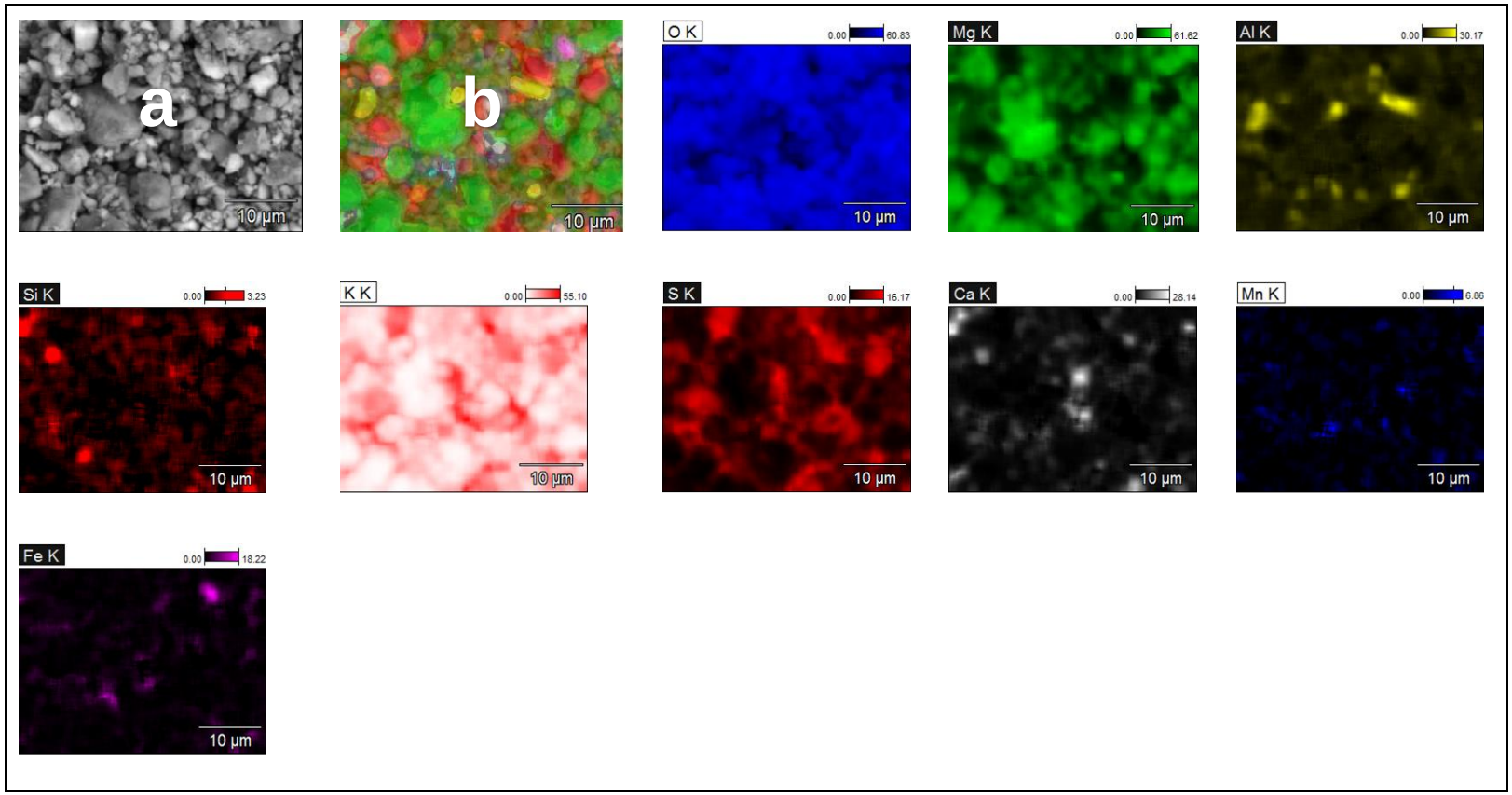


Figure 4-2. SEM-EDS mapping of magnesia-spinel brick type B

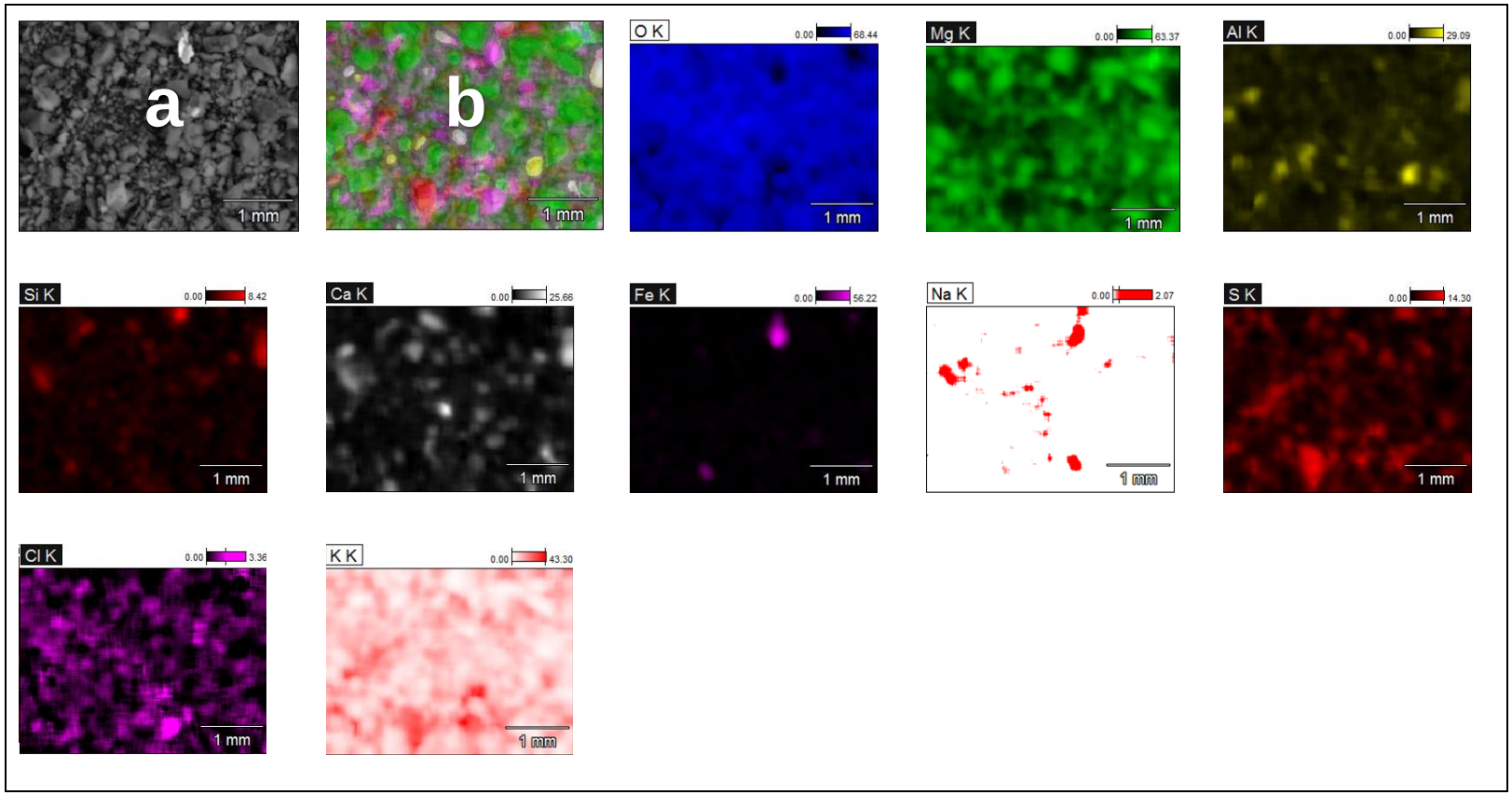


Figure 4-3. SEM-EDS mapping magnesia-fused spinel

Table 4-3. Phase composition of the virgin and damaged magnesia bricks, based on XRD analysis

Phases	Chemical composition (weight %).					
	Magnesia-spinel brick type A		Magnesia-spinel brick type B		Magnesia-fused spinel	
	virgin	damaged	virgin	damaged	virgin	damaged
MgO (periclase)	91.00	87.00	86.31	88.63	85.25	83.02
$MgFe_{0.2}Al_{1.8}O_4$ (spinel)	9.00	7.00	13.69	8.07	14.75	14.77
KCl (sylvite)	-	5.00	-	-	-	-
$CaSO_4$ (anhydrite)	-	1.00	-	-	-	-
$Na_{0.5}K_{0.5}Cl$ (sodium potassium chloride)	-	-	-	2.23	-	2.21
K_2SO_4 (arcanite)	-	-	-	1.07	-	-
Total	**100.00**	**100.00**	**100.00**	**100.00**	**100.00**	**100.00**

The XRD raw data is provided in appendix A. From Table 4-3, XRD results of the damaged refractory bricks (magnesia-spinel brick type A, magnesia-spinel brick type B and magnesia-fused spinel) showed the presence of contaminating phases such as KCl (sylvite), $CaSO_4$ (anhydrite), K_2SO_4 (Arcanite) and (Na, K) Cl (sodium potassium chloride). These phases are low melting phases. It can also be seen that there is a decrease in spinel content in the bricks of type A and B whilst the spinel content in magnesia-fused spinel practically, remains constant.

The results of XRF, SEM-EDS and XRD all confirmed the presence of impurities in the damaged magnesia lining. Evidently a chemical reaction took place between the clinker feed, the surrounding atmosphere and the magnesia lining as it was reported in the open literature (Bartha and Sodje., 2001, Kunnecke., 1998 and Potgieter et al., 2004).

4.3 Formation of impurity species in the damaged bricks

Chemical analysis identified SO_3, Cl, Na_2O and K_2O as the contaminating species in the damaged refractory lining. Furthermore, XRD analysis of the damaged bricks revealed the presence of the low-melting phases such as KCl, $CaSO_4$, (Na, K) Cl and K_2SO_4. These phases were likely formed by reactions between dust and alkalies entrained in the kiln gases and the refractory bricks in the burning zone (Peray and Waddell., 1972).

4.3.1 Formation of KCl

The potassium oxide in the feed and chlorine in the kiln gas atmosphere migrate into the brick and react together to form KCl that fills the brick pores (Kunnecke, 1998).

$$K_2O + Cl_2 \rightarrow 2KCl + \frac{1}{2}O_2 \qquad \text{E.q 4-1}$$

The formation of KCl phase compromises the refractoriness of the lining. KCl is liquid at 770°C, which is lower than clinkerization temperature (1450°C) in the burning zone, and it can migrate into the brick structure until its condensation temperature (770°C) is reached. The crystallization of this salt will lead to densification of the brick structure accompanied by a reduction of the elasticity and the thermal shock resistance of the affected parts. The formation of KCl could be accompanied by a significant volume increase (up to 30%) in refractory. This can result in a structural weakening of the brick hot face (Bartha and Sodje, 2001, Kunnecke., 1998 and Potgieter et al., 2004).

4.3.2 Formation of $CaSO_4$

The formation of $CaSO_4$ resulted from excessive sulphur in the kiln gas atmosphere. The $CaSO_4$ is formed from the chemical reaction of the components of the MgO brick, CaO reacting with the SO_3 in the kiln gas atmosphere. The formation of $CaSO_4$ is accompanied by an increase in volume,

leading to weakening of the physical properties of the affected brick horizons (brick phase), and which results in the destruction of the brick texture. The sulphur trioxide in the kiln gas atmosphere attacks the calcium silicate ($2CaO.SiO_2$) bond of the magnesia-spinel brick to form $CaSO_4$ (Bartha and Sodje, 2001 and Kunnecke., 1998).

$$2CaO.SiO_2 + SO_3 \rightarrow CaSO_4 + CaO.SiO_2 \qquad \text{E.q 4-2}$$

The formation of $CaSO_4$ weakens the lining. It forms a liquid at 1460 °C which is the clinkerization temperature (1450 °C) in the burning zone.

4.3.3 Formation of (Na, K) Cl

Based on the results found by Kunnecke (1998), sodium oxide, potassium oxide and chlorine can migrate into the magnesia lining and react together to form (Na, K) Cl, filling the brick pores (Eq. 4-3).

$$2NaO + K_2O + Cl_2 \rightarrow 2(Na, K)\,Cl + \frac{3}{2}O_2 \qquad \text{E.q 4-3}$$

4.3.4 Formation of K_2SO_4

Kunnecke (1998) also reported similar mechanism to explain the formation of K_2SO_4. Potassium oxide and sulphur trioxide react together into the magnesia-spinel brick type B and form K_2SO_4 liquid. This reaction can be written as follows:

$SO_3 + K_2O \rightarrow K_2SO_4$ E.q 4-4

In general, the crystallization of salts leads to densification of the brick structure, which is accompanied by a reduction of the elasticity and thermal shock resistance of the affected parts. It was reported that the formation of (Na, K) Cl and K_2SO_4 can significantly increase the volume of the refractory brick up to 30%. This will definitely result in the structural weakening of the brick hot face (Bartha and Sodje, 2001, Kunnecke., 1998 and Potgieter et al., 2004).

4.4 Diffusion of the clinker into the magnesia bricks

The clinker diffusion into the refractory brick was studied through chemical and microstructural analysis of the unused and damaged magnesia lining, using SEM equipped with EDS. Prepared polished brick sections were used in both analyses. The chemical compositions of damage magnesia bricks are given in Table 4-4.

Table 4-4. Elemental composition of the damaged magnesia polished brick section, based on SEM-EDS chemical analysis.

Chemical composition (Weight %).			
Elements	**damaged**		
	magnesia-spinel brick type A	**magnesia-spinel brick type B**	**magnesia-fused spinel**
O	38.85	56.63	59.55
Na	0.43	-	-
Mg	30.25	39.02	28.70
Al	1.42	0.38	8.66
Si	0.54	0.80	0.45
S	4.48	-	-
Cl	8.13	0.40	0.48
K	8.82	0.46	0.98
Ca	6.52	1.97	0.38
Fe	0.57	0.34	0.79
Total	**100.00**	**100.00**	**100.00**

The results from SEM-EDS analysis showed that there is no major increase of the main clinker elements such as Ca, Si, Al and Fe in the damaged magnesia brick. However, there is an increase in iron oxide and alumina content in the damaged magnesia-fused brick. This can be explained by the preferential

diffusion of iron oxide and alumina from clinker into the refractory (Serena et al., 2004).

The absence of the clinker diffusion into the refractory brick was also confirmed by comparing the XRD analysis of the clinker and damaged refractory bricks. From Table 4-3, the known clinker phases such as alite (Ca_3SiO_5), belite (Ca_2SiO_4), aluminate ($Ca_3Al_2O_6$) and ferrite (Ca_2AlFeO_5) do not appear among the phases identified in the damaged refractory bricks. Hence the clinker diffusion cannot explain the mechanism of refractory lining failure.

The SEM micrographs of unused and damaged magnesia bricks are respectively shown in figures 4-4a, 4-4b, 4-5a, 4-5b, 4-6a and 4-6b. All of the SEM micrographs show similar morphology and therefore no clinker diffusion took place into the damaged magnesia bricks. The clinker diffusion is likely to be present as devitrified glassy phase (see figure 2-1) in the refractory materials due to refractory-clinker chemical reaction (Pena et al., 2007). In addition, the micrographs show no existence of longitudinal or transverse cracks in the damaged magnesia bricks.

Although no clinker phase diffused into the refractory bricks, a major reduction in spinel content was observed in the magnesia-spinel bricks (type A and type B). At 1450 °C (burning zone temperature), the clinker reacted with spinel to form a liquid phase (Pena et al., 2007). In this study, the spinel content

decreased from 9% to 7% for the magnesia-spinel brick type A and from 14% to 8% for the magnesia-spinel brick type B.

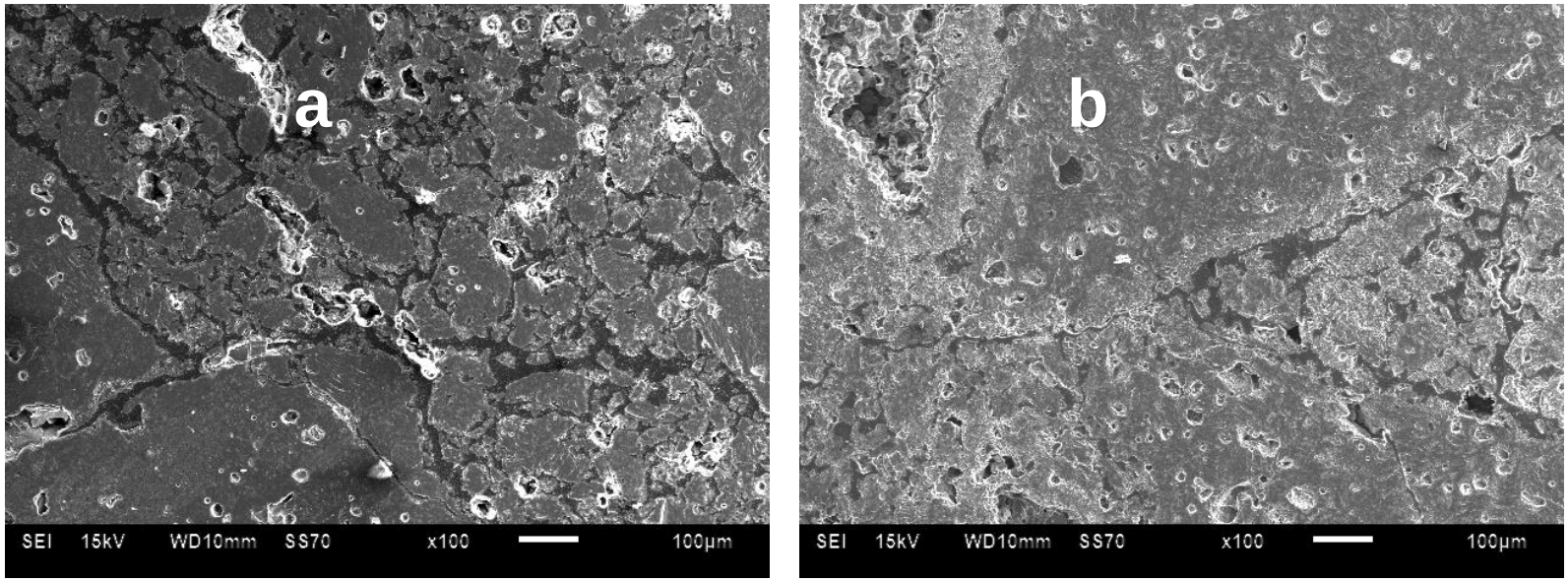


Figure 4-4. The SEM micrograph polished brick section of magnesia-spinel brick type A, a) the unused, and b) the damaged

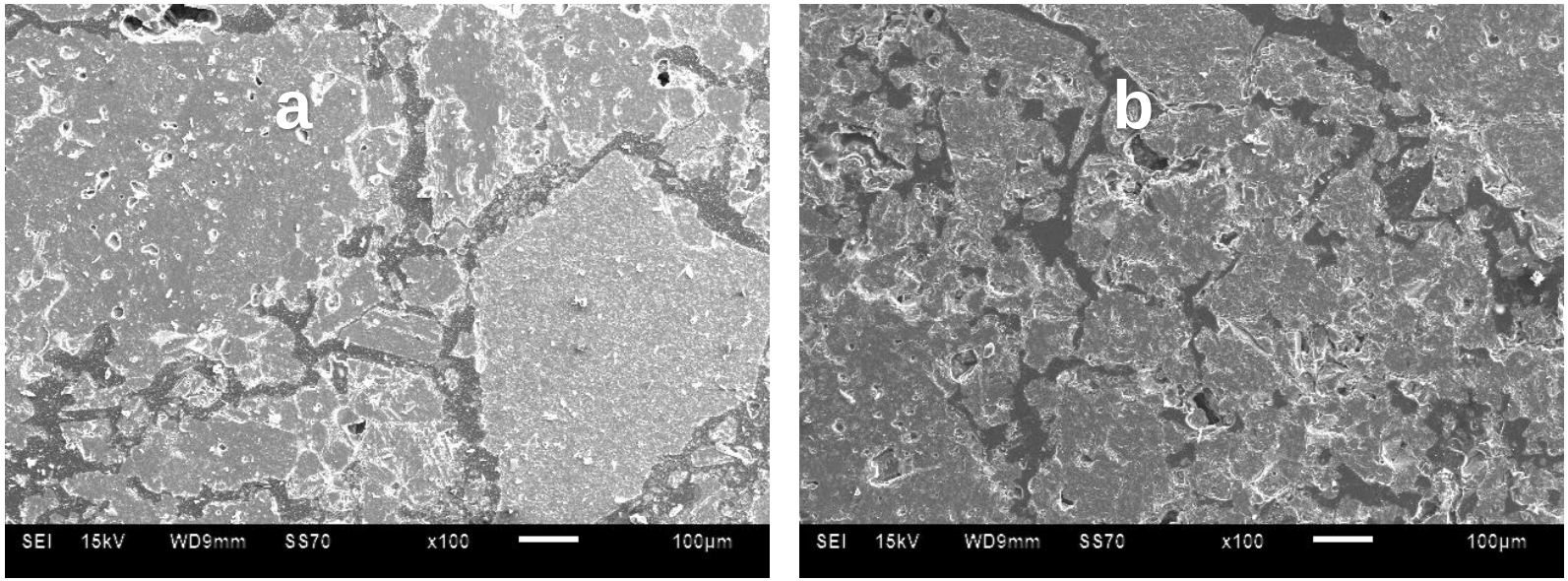


Figure 4-5. The SEM micrograph polished brick section of magnesia-spinel brick type B, a) the unused, and b) the damaged

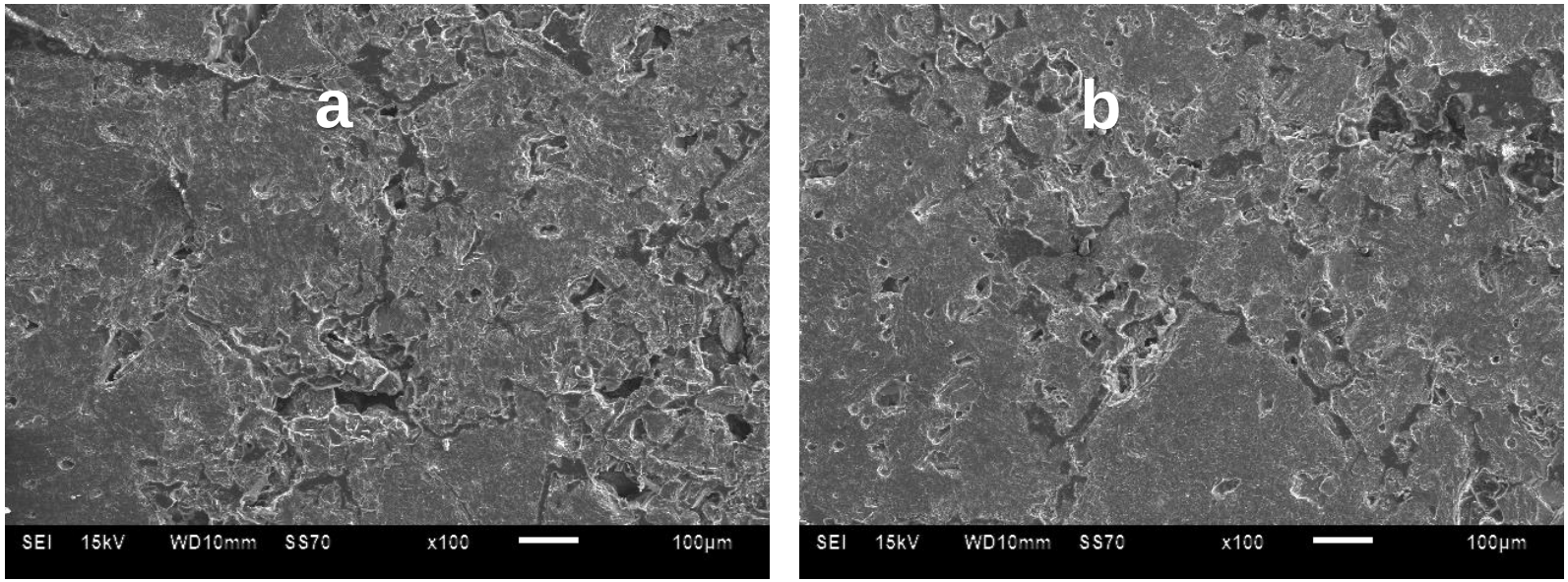


Figure 4-6. The SEM micrograph polished brick section of magnesia-fused spinel, a) the unused, and b) the damaged

4.5 Microstructural examination for thermal shock attack

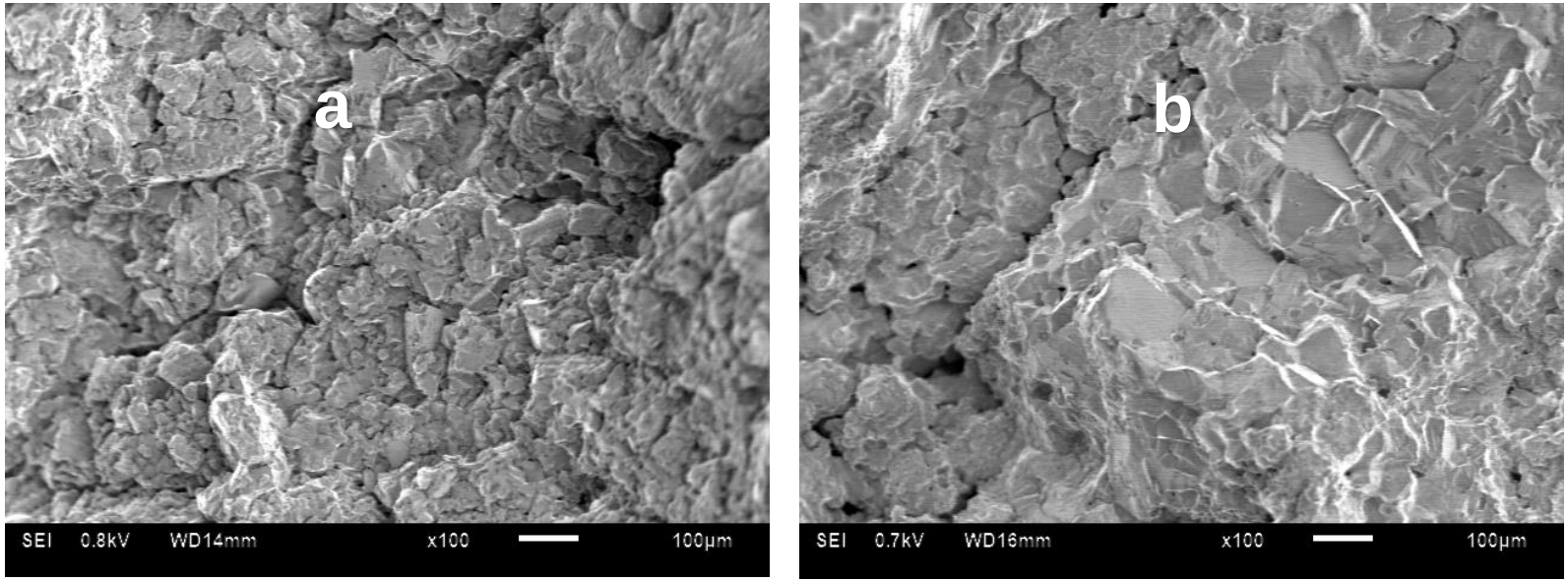


Figure 4-7. The SEM micrograph fracture of magnesia-spinel brick type A, a) the unused, and b) the damaged

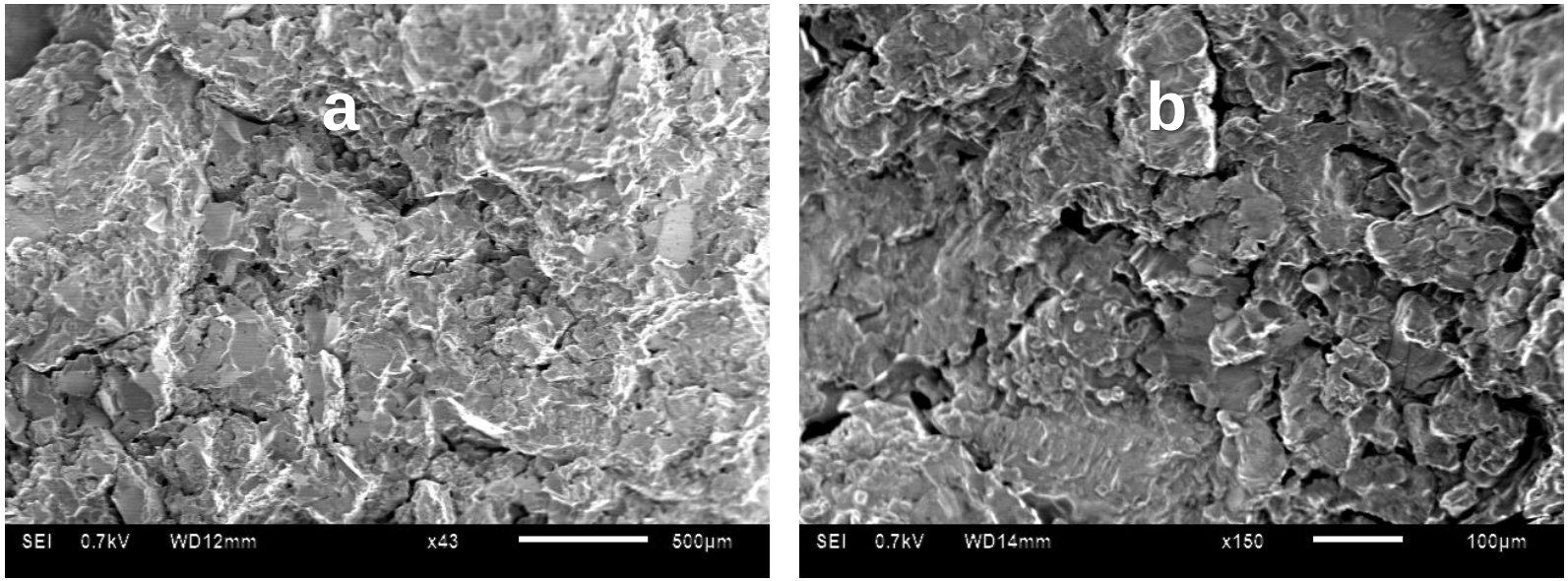


Figure 4-8. The SEM micrograph fracture of magnesia-spinel brick type B, a) the unused, and b) the damaged

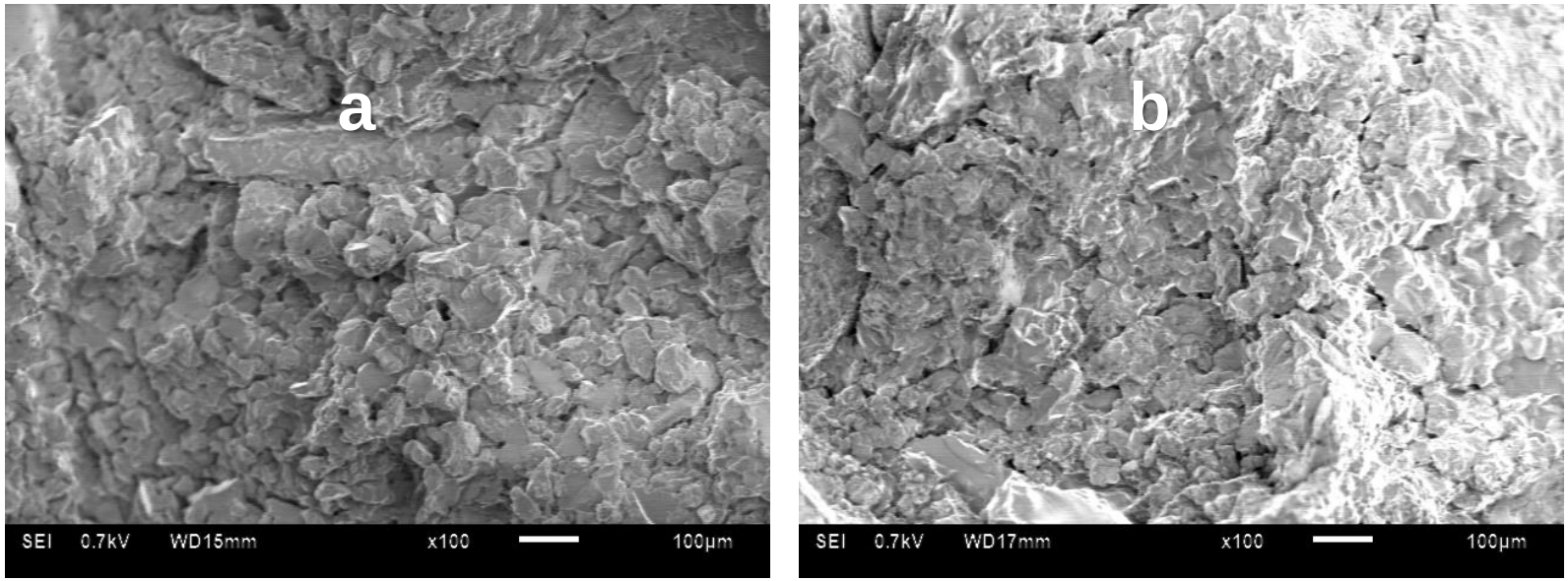


Figure 4-9. The SEM micrograph fracture of magnesia-fused spinel brick, a) the unused, and b) the damaged

The failure of the refractory brick by thermal shock attack was investigated through microstructural analysis of the polished sections of unused and damaged magnesia lining, using SEM equipped with EDS. The SEM microstructures of tested refractory bricks are given in Figure 4-7, 4-8, 4-9.

From SEM micrographs, it can be seen that there is an intergranular fracture (see figure 2-5) in all unused and damaged magnesia bricks. However, no major crack can be easily detected on all SEM microstructures. Therefore the thermal shock attack could not be described as a source of the refractory brick failure.

Ghosh et al. (2004) identified the reduction of spinel content as the cause of thermal shock attack in magnesia-spinel refractory bricks. Conversely, the SEM micrographs showed that fracture is intergranular and this hinders the cracks to easily propagate because the larger microcrack networks of intergranular fracture will permit accommodation of thermal strain and reduce thermal stresses (Aksel et al. (2004b)).

4.6 Thermodynamics (phase diagrams)

In this section, the interactions between the impurities (Cl_2, SO_3, K_2O and Na_2O) and the damaged magnesia lining are discussed based on the thermodynamic considerations. The chemical compositions of the lining were calculated (conversion of mass % to mole %) in appendix B and expressed in terms of mole percent (Table 4-5) and referred to ternary phase diagrams of impurity component – MgO – Al_2O_3 or CaO. Each phase diagram was constructed for burning zone conditions (1500ºC, 1 atm) using FactSage model.

Table 4-5. Molar composition of the damaged magnesia lining, based on XRF assay

Mole fraction %.			
Chemical species	**Damaged**		
	Magnesia-spinel brick type A	**Magnesia-spinel brick type B**	**Magnesia-fused spinel**
SiO_2	0.33	0.52	0.75
Al_2O_3	6.48	7.20	7.53
Fe_2O_3	0.15	0.20	0.18
CaO	5.18	0.94	0.98
MgO	84.45	89.40	89.41
Mn_2O_3	0.03	0.04	-
SO_3	0.50	0.49	0.20
Na_2O	0.39	0.25	0.25
Cl	1.28	-	0.18
K_2O	1.22	0.96	0.53
Total	**100.00**	**100.00**	**100.00**

4.6.1 Effect of chlorine (Cl_2)

The ternary phase diagram of the MgO-Al_2O_3-KCl system, was used to investigate the effect of chlorine on the brick properties. Chlorine gas is often associated with the formation of KCl (E.q 4-1).

In the ternary phase diagram, KCl is a vapour at 1450 - 1500^oC.

Table 4-6. Normalised composition of the damaged magnesia lining, for Cl_2 effect

	Mole %.		
Chemical species	**Damaged**		
	Magnesia-spinel brick type A	**Magnesia-spinel brick type B**	**Magnesia-fused spinel**
Al_2O_3	7.00	0	7.72
MgO	90.53	0	91.65
KCl	2.47	0	0.64
Total	**100.00**	**0**	**100.00**

The normalised compositions of the damaged magnesia-spinel refractory brick type A and magnesia-fused spinel are respectively plotted in Figure 4-10 and 4-11, and fall within the phase field of $KCl_{(g)}$ + Spinel + Monoxide ($KCl_{(g)}$ - $MgAl_2O_4$ - MgO) (point A and X). The blue lines represent the composition of the bricks.

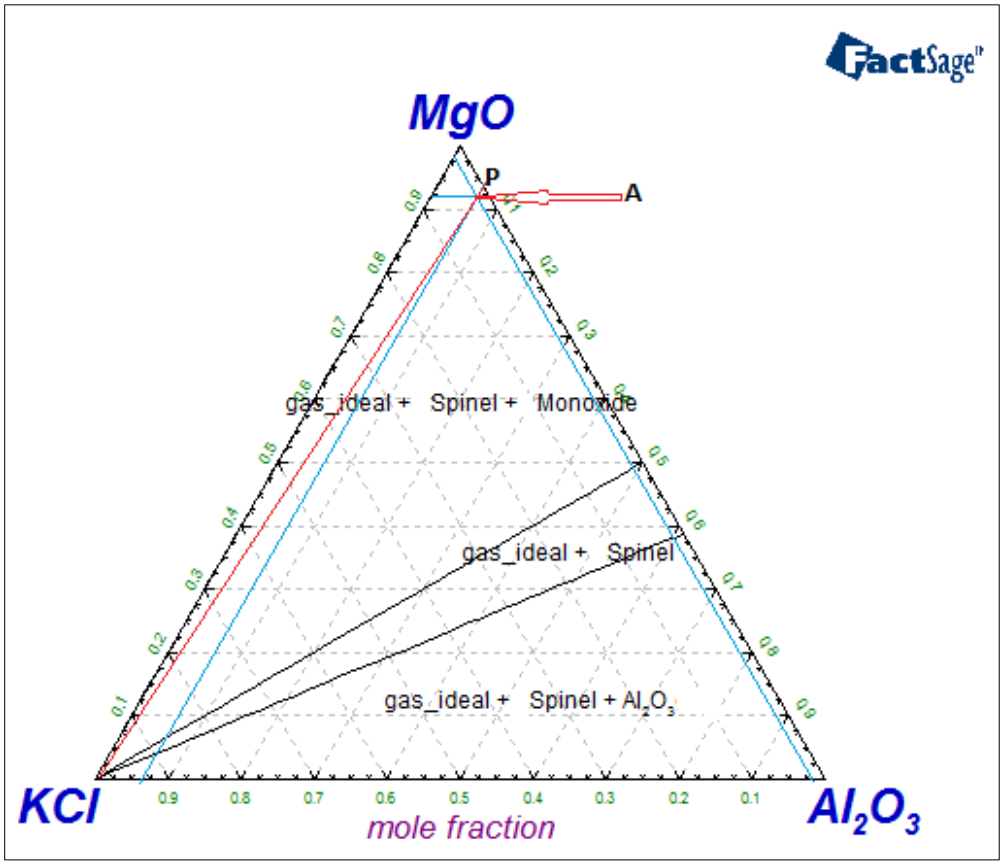


Figure 4-10. System MgO-Al_2O_3-KCl ternary phase diagram at 1500 °C and 1 atmosphere for magnesia-spinel brick type A

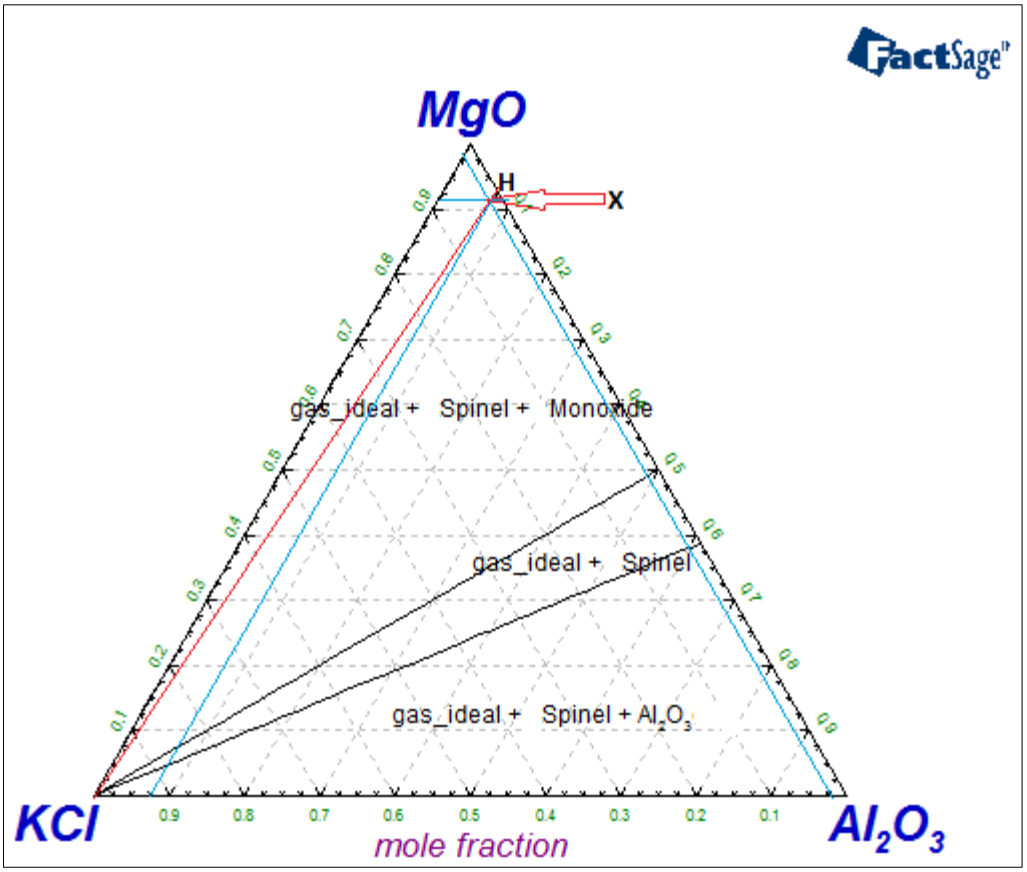


Figure 4-11. System MgO-Al_2O_3-KCl ternary phase diagram at 1500 °C and 1 atmosphere for magnesia-fused spinel

At point P (Figure 4-10) and point H (Figure 4-11), only $MgAl_2O_4$ and free MgO exist. Moving along the KCl line (red line), no phase transformation takes place. On this phase diagram prediction, the effect of KCl does not result in phase transformation and does not explain the refractory brick failure.

4.6.2 Effect of sulphur trioxide (SO_3)

The effect of sulphur trioxide was studied by considering the ternary phase diagram of MgO-CaO-SO_3 system (Figure 4-12, 4-13 and 4-14).

Table 4-7. Normalised composition of the damaged magnesia lining, for SO_3 effect

Mole %.			
Chemical species	**Damaged**		
	Magnesia-spinel brick type A	**Magnesia-spinel brick type B**	**Magnesia-fused spinel**
CaO	5.75	1.03	1.08
MgO	93.70	98.43	98.70
SO_3	0.55	0.54	0.22
Total	**100.00**	**100.00**	**100.00**

The normalised compositions of the damaged magnesia-spinel refractory brick type A and magnesia-spinel refractory brick type B and magnesia-fused spinel are respectively given in Figure 4.12, 4-13 and 4-14. The blue lines represent the composition of the bricks. All these compositions fall within the phase field of $CaSO_{4\,(liquid)}$ + $CaO_{\,(s)}$ + $MgO_{\,(s)}$ ($CaSO_{4\,(liq)}$ – $MgO_{\,(s)}$ – $CaO_{\,(s)}$) (Point B, E and V). This can be associated with the following reaction:

$$MgO + 2CaO + SO_3 \rightarrow CaSO_{4\,(liq)} + MgO_{\,(s)} + CaO_{\,(s)} \qquad \text{E.q 4-5}$$

At point J, Y and O, only CaO and MgO exist. Moving along the SO_3 line (red line), phase transformation occurs. The effect of SO_3 is the formation of liquid ($CaSO_{4\,(liquid)}$) in the magnesia-spinel bricks which compromise the refractoriness of the brick resulting in premature failure.

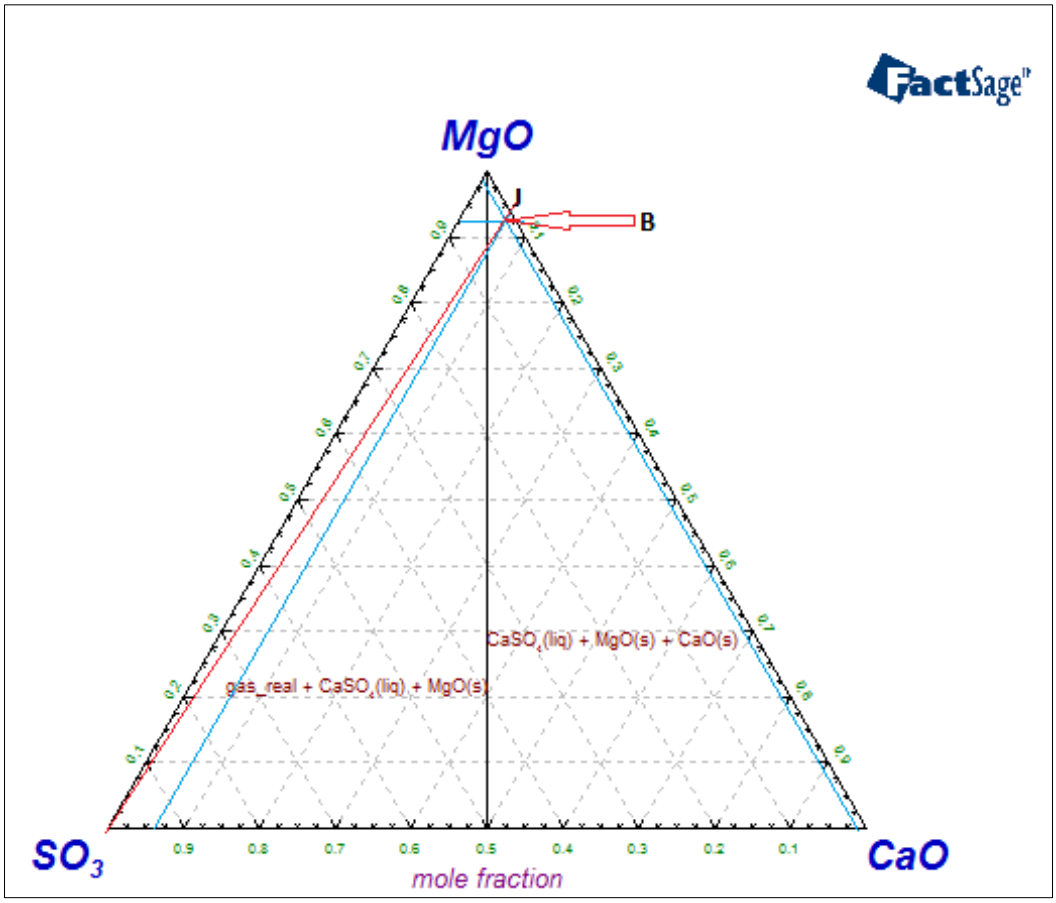


Figure 4-12. System MgO-CaO-SO_3 ternary phase diagram at 1500 °C and 1 atmosphere for magnesia-spinel brick type A

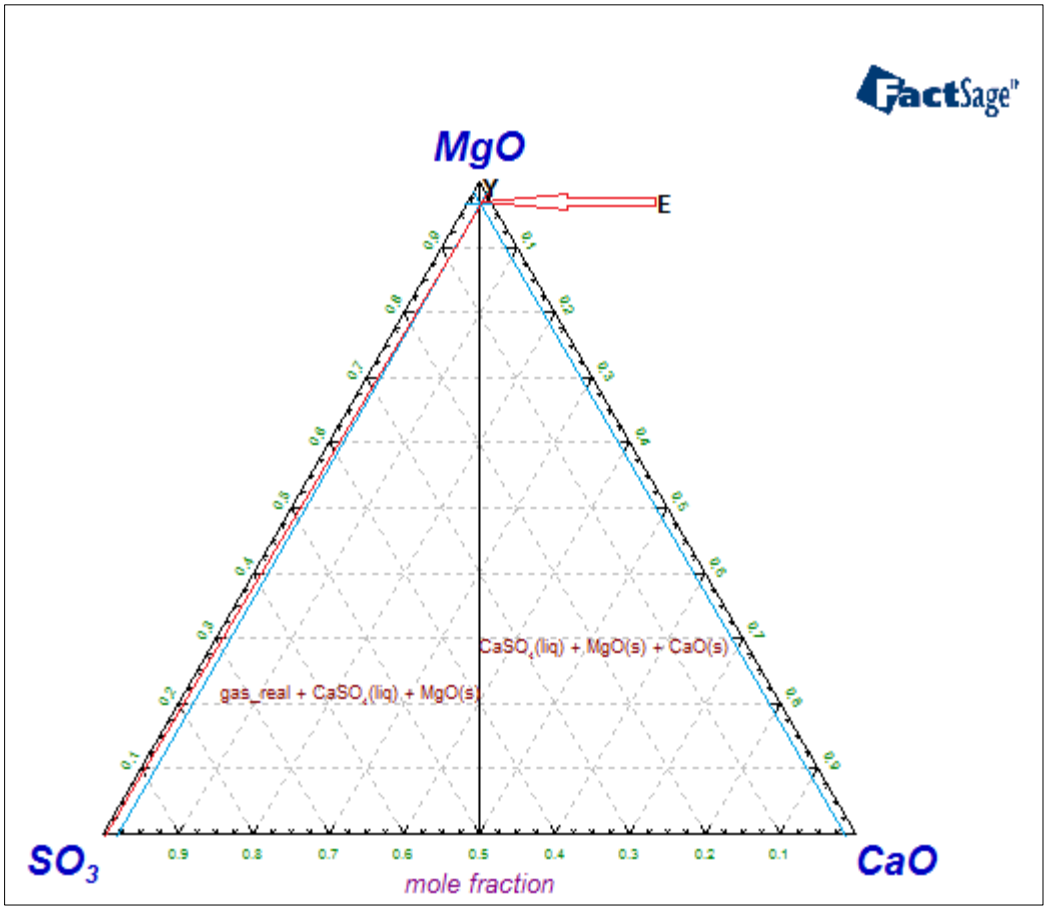


Figure 4-13. System MgO-CaO-SO_3 ternary phase diagram at 1500 °C and 1 atmosphere for magnesia-spinel brick type B

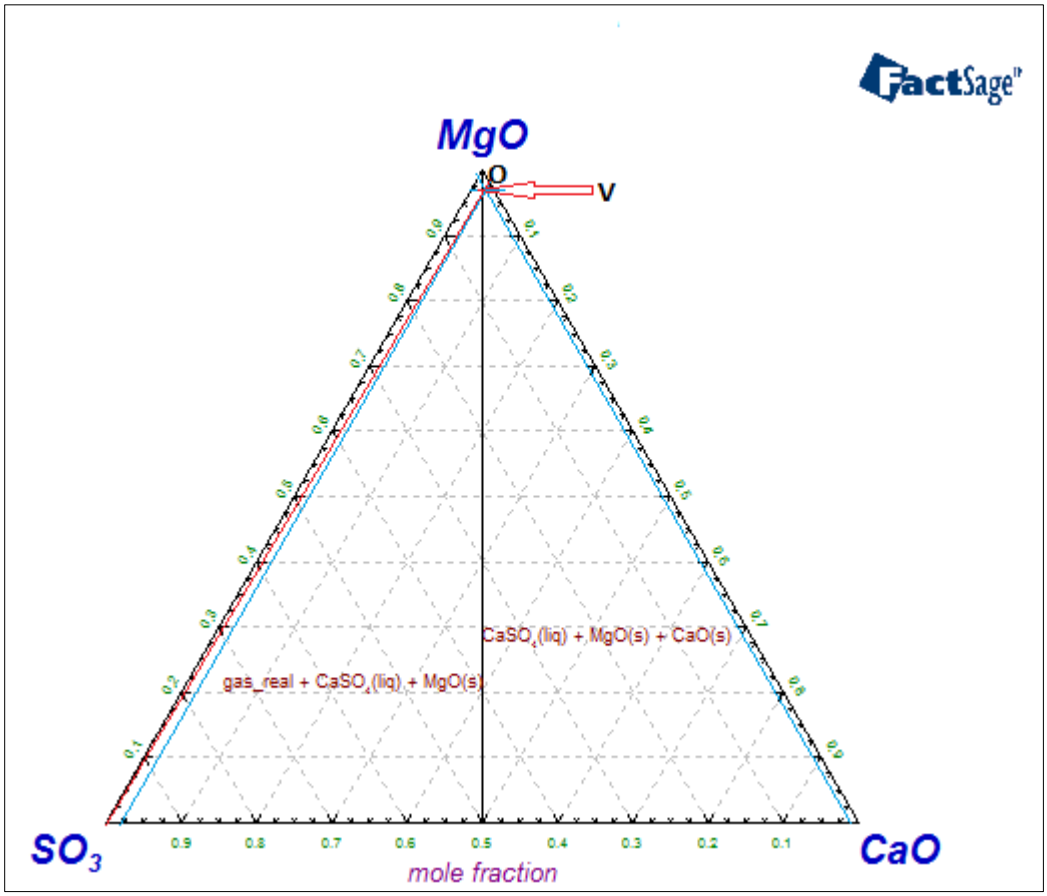


Figure 4-14. System MgO-CaO-SO_3 ternary phase diagram at 1500 °C and 1 atmosphere for magnesia-fused spinel

4.6.3 Effect of sodium oxide (Na_2O)

The effect of sodium oxide on the stability of the refractory bricks was investigated using the ternary phase diagram of MgO-Al_2O_3-Na_2O system as shown in Figure 4-15, 4-16 and 4-17. A re-drawn phase diagram is provided in Figure 4-18 for clarity.

Table 4-8. Normalised composition of the damaged magnesia lining, for Na_2O effect

Mole %.			
Chemical species	**Damaged**		
	Magnesia-spinel brick type A	**Magnesia-spinel brick type B**	**Magnesia-fused spinel**
Al_2O_3	7.08	7.43	7.75
MgO	92.48	92.31	92.00
Na_2O	0.43	0.26	0.43
Total	**100.00**	**100.00**	**100.00**

The normalised compositions of the damaged magnesia-spinel refractory brick type A, damaged magnesia-spinel brick type B and magnesia-fused spinel are respectively shown in Figure 4-15, 4-16 and 4-17. All these compositions (Point C, K and S) fall within the phase field of $NaAlO_2$ + monoxide + spinel ($NaAlO_2$ – MgO – $MgAl_2O_4$). This can be associated with the following reaction:

$$Na_2O + 2Al_2O_3 + 2MgO \rightarrow 2NaAlO_2 + MgAl_2O_4 + MgO \qquad \text{E.q 4-6}$$

At point T, R and K only $MgAl_2O_4$ and free MgO exist. Moving along Na_2O line (red line) as the amount of Na_2O increases, phase transformation occurs.

It can be concluded that the effect of sodium oxide is driving by the formation of $NaAlO_2$ which promotes liquid formation when Na_2O content increases in the magnesia refractory lining. The liquid formation will compromise the refractoriness of the brick resulting in premature failure.

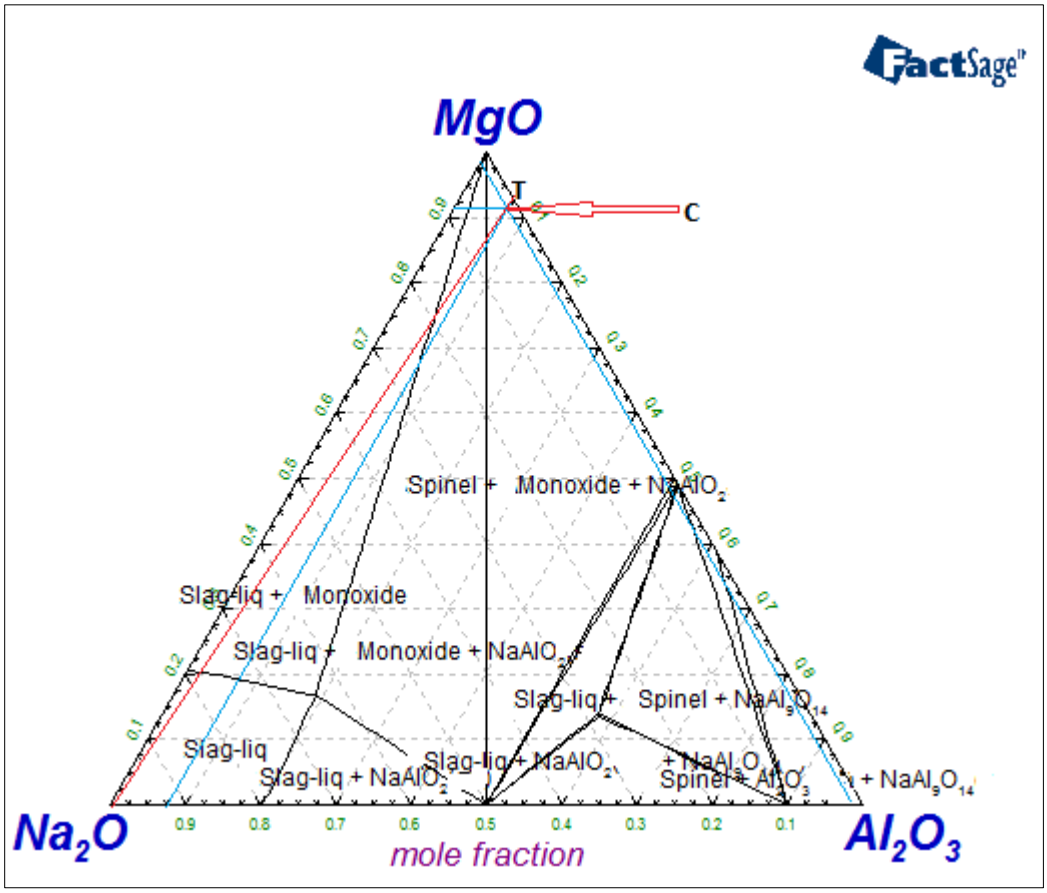


Figure 4-15. System MgO-Al_2O_3-Na_2O ternary phase diagram at 1500 °C and 1 atmosphere for magnesia-spinel brick type A

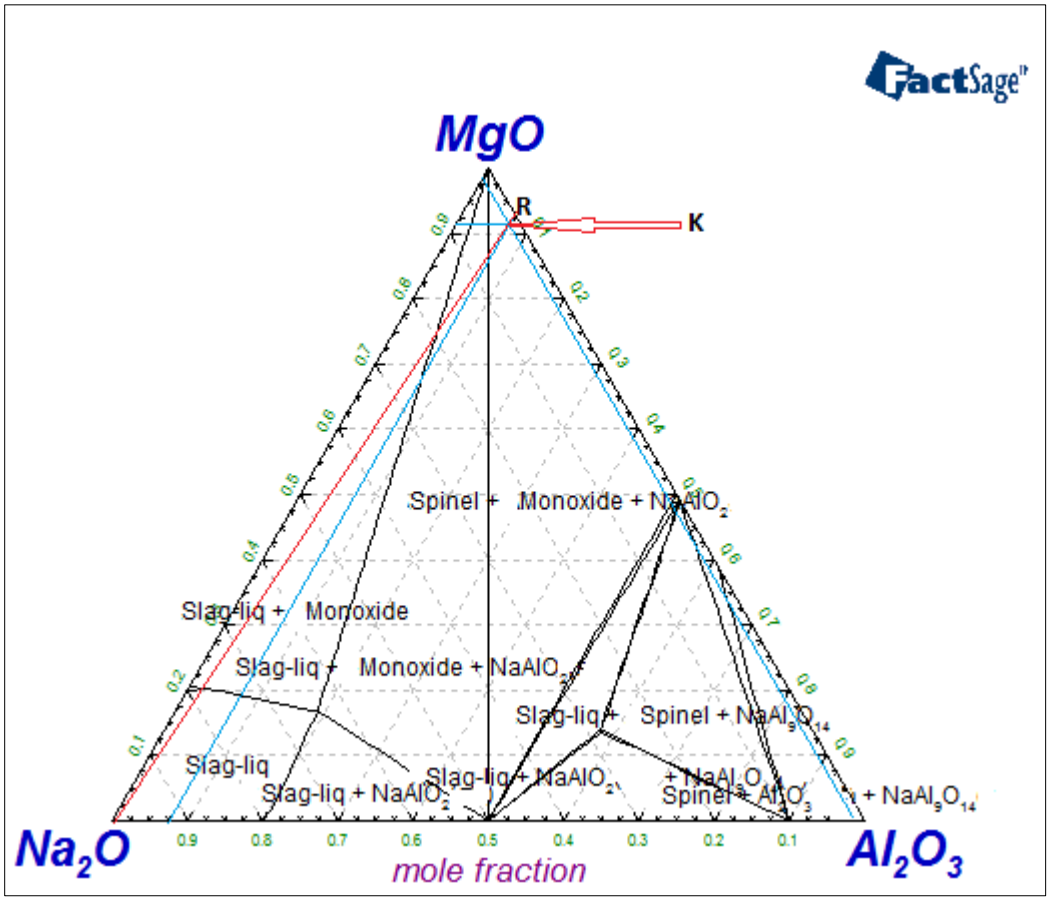


Figure 4-16. System MgO-Al_2O_3-Na_2O ternary phase diagram at 1500 °C and 1 atmosphere for magnesia-spinel brick type B

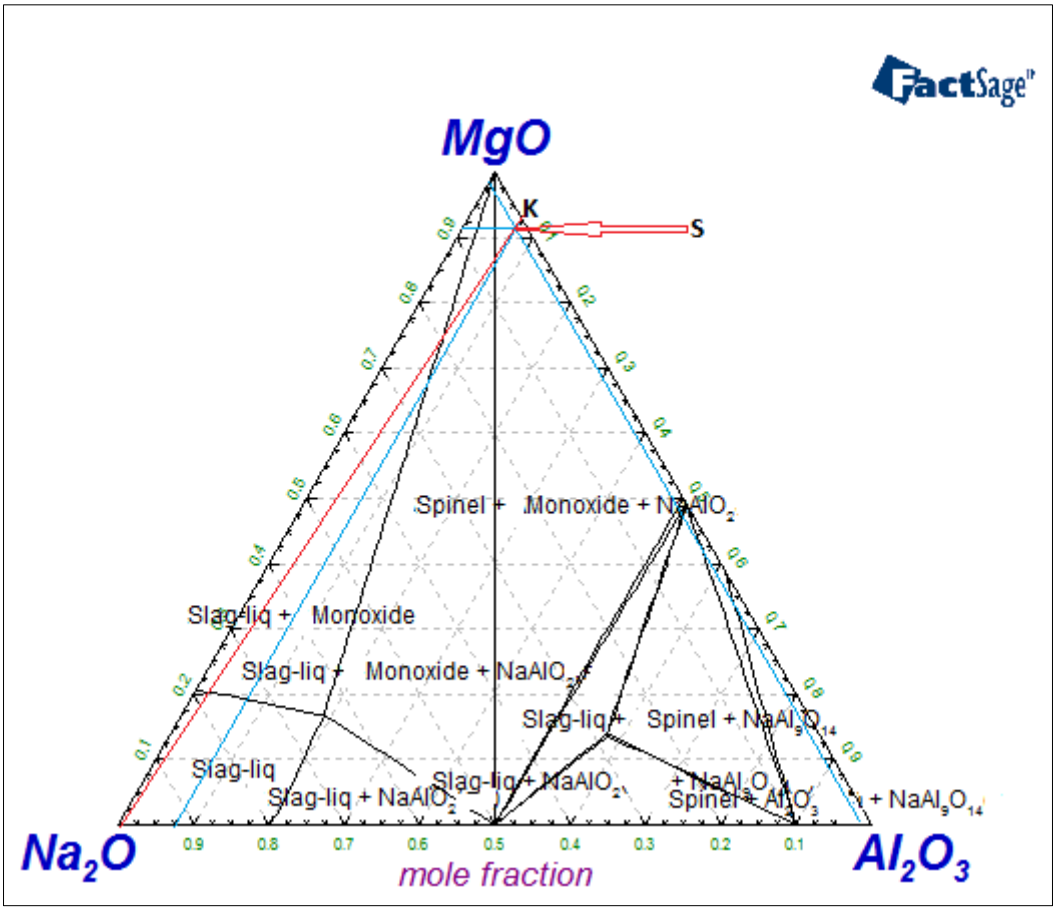


Figure 4-17. System MgO-Al_2O_3-Na_2O ternary phase diagram at 1500 °C and 1 atmosphere for magnesia-fused spinel

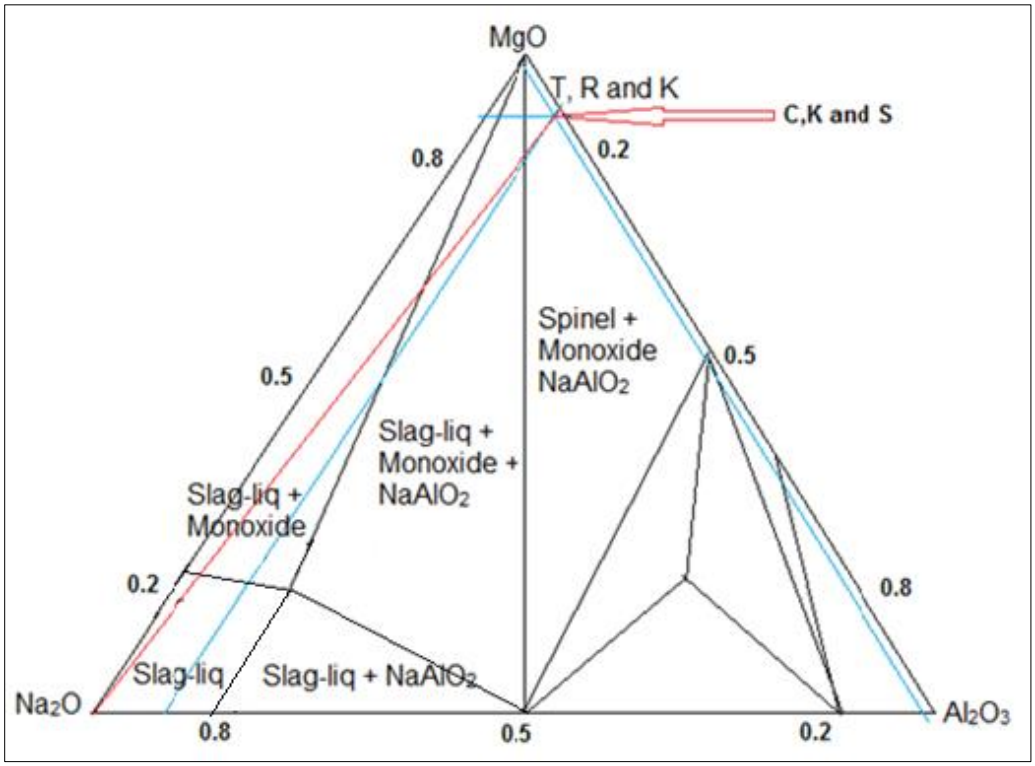


Figure 4-18. System $MgO-Al_2O_3-Na_2O$ ternary phase diagram at 1500 °C and 1 atmosphere

4.6.4 Effect of potassium oxide (K_2O)

The ternary phase diagram of MgO-Al_2O_3-K_2O (Figure 4-19, 4-20 and 4-21) was used to illustrate the effect of K_2O on the lining properties. A re-drawn phase diagram is provided in Figure 4-22 for clarity.

Table 4-9. Normalised composition of the damaged magnesia lining, for K_2O effect

Mole %.			
Chemical species	**Damaged**		
	Magnesia-spinel brick type A	**Magnesia-spinel brick type B**	**Magnesia-fused spinel**
Al_2O_3	7.03	7.38	7.73
MgO	91.65	91.46	91.73
K_2O	1.32	0.98	0.54
Total	**100.00**	**100.00**	**100.00**

Each normalised composition of the damaged bricks magnesia-spinel type A, magnesia-spinel type B and magnesia-fused spinel falls in the phase field of monoxide + spinel + $KAlO_2$ ($MgO – MgAl_2O_4$ - $KAlO_2$). At point D, Q and R, $Na_2O + Al_2O_3 + MgO$ react together according to the following reaction:

$$2MgO + 2Al_2O_3 + K_2O \rightarrow 2KAlO_2 + MgAl_2O_4 + MgO \qquad \text{E.q 4-7}$$

At point L and I only $MgAl_2O_4$ and free MgO exist. Moving along K_2O line (red line) as the amount of K_2O increases, phase transformation occurs.

It can be concluded that the effect of sodium oxide is driving by the formation of $KAlO_2$ which promotes liquid formation when K_2O content increases in the magnesia refractory lining. The liquid formation will compromise the refractoriness of the brick resulting in premature failure.

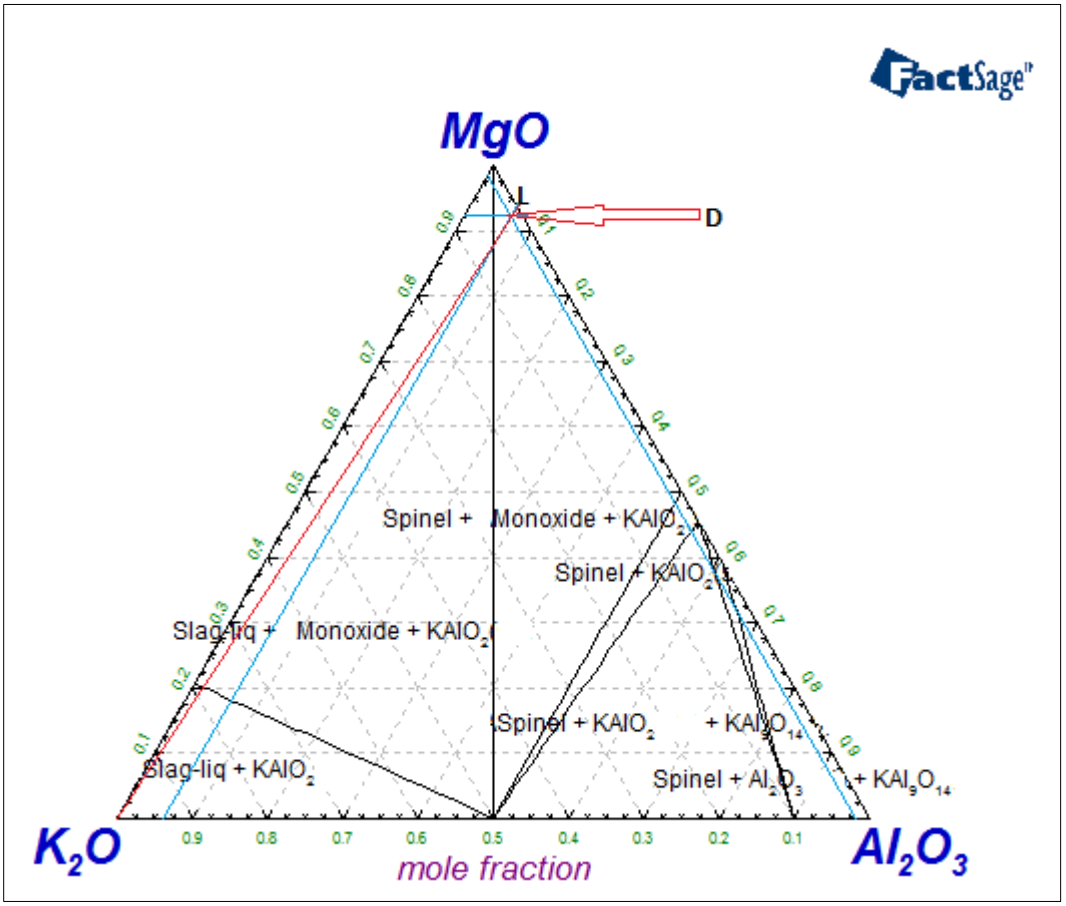


Figure 4-19. System MgO-Al_2O_3-K_2O ternary phase diagram at 1500 °C and 1 atmosphere for magnesia-spinel brick type A

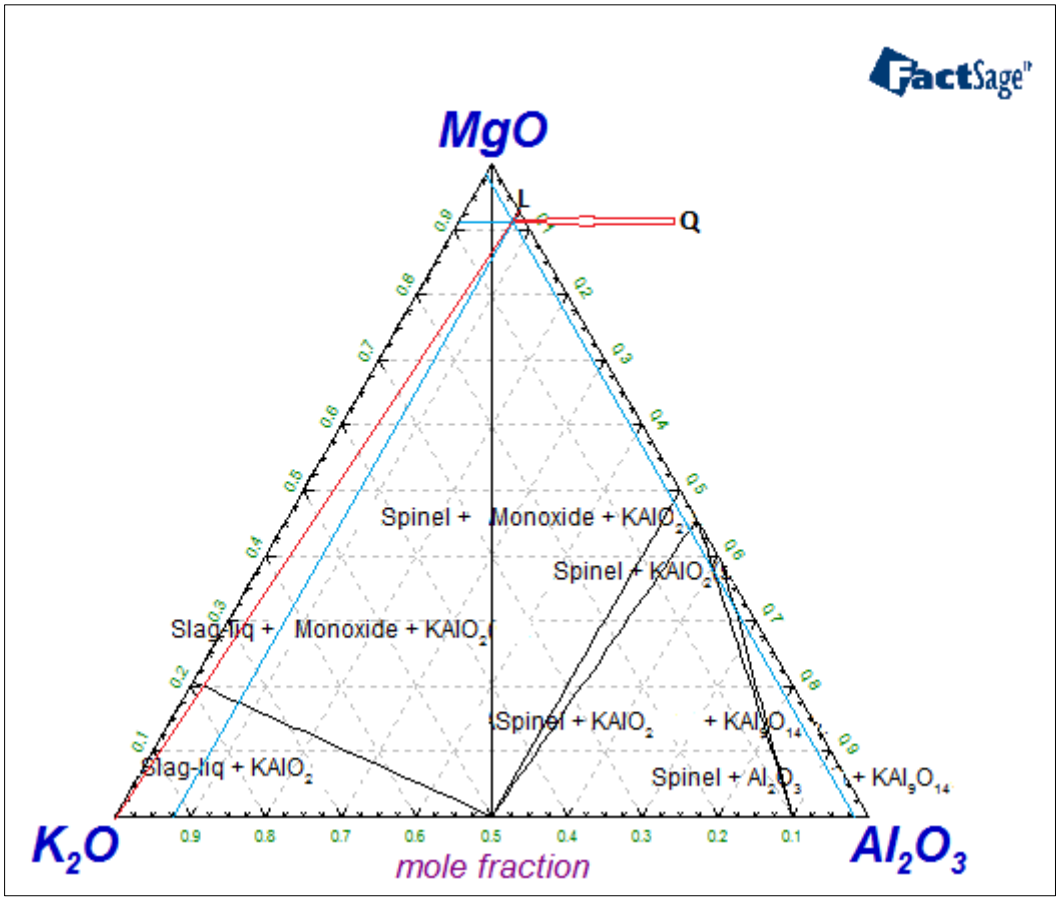


Figure 4-20. System MgO-Al_2O_3-K_2O ternary phase diagram at 1500 °C and 1 atmosphere for magnesia-spinel brick type B

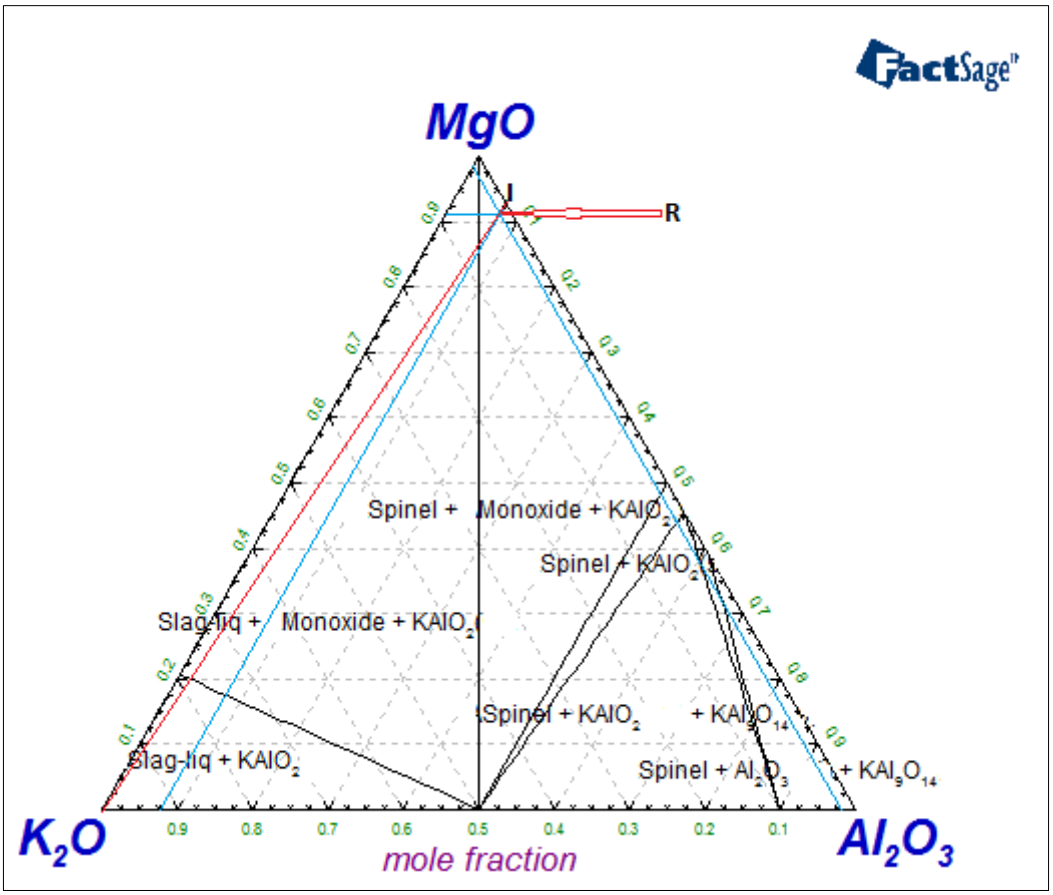


Figure 4-21. System MgO-Al_2O_3-K_2O ternary phase diagram at 1500 °C and 1 atmosphere for magnesia-fused spinel

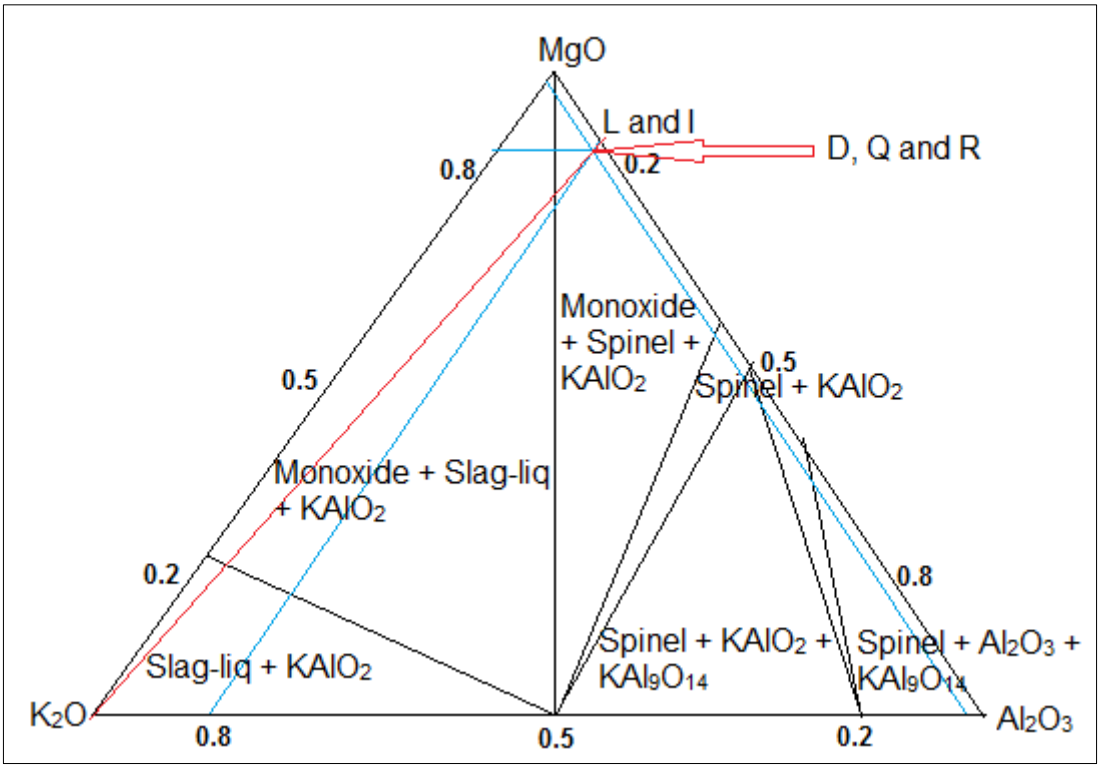


Figure 4-22. System $MgO-Al_2O_3-K_2O$ ternary phase diagram at 1500 °C and 1 atmosphere

4.7 Conclusion

The mechanisms for failure of the magnesia refractory lining were discussed based on chemical analysis, post-mortem microstructural examinations and interaction predictions by ternary phase diagrams.

Chemical analysis of damaged magnesia refractory lining revealed the presence of alkalies and gaseous impurities. The effect of these species resulted in the failure of the magnesia lining by chemical attack. Low melting phases of KCl, $CaSO_4$, K_2SO_4 and (Na, K) Cl were formed resulting in a decrease in liquidus temperature of the refractory lining. The formation of the liquid in the lining then reduced its refractoriness.

The microstructural examination of the damaged magnesia brick sections revealed no clinker phase that migrated and diffused into the brick. It is clear that the failure of the refractory lining was not driven by the clinker diffusion.

The examination of the SEM microstructures showed no major cracks in all damaged magnesia brick sections. Fracture is intergranular in all unused and damaged magnesia bricks. Despite the reduction in spinel content on the damaged magnesia-spinel bricks, the SEM micrographs showed intergranular fracture which will prevent the propagation of the cracks in all magnesia bricks. In the intergranular fracture cracks will not propagate easily.

CHAPTER FIVE

5 RESULTS AND DISCUSSION: HIGH - ALUMINA BRICK

5.1 Introduction

The high-alumina brick was applied at the lower transition zone of the rotary cement kiln. The failure mechanism of the high alumina lining was studied by using XRF, XRD, SEM-EDS and computational thermochemistry (phase diagrams).

5.2 Chemical analysis of the high-alumina refractory lining

The chemical analysis of virgin and used high-alumina lining from the kiln is shown in Table 5-1. The impurity species in used high-alumina lining are K_2O, SO_3, and Na_2O.

Table 5-1. Chemical composition of virgin and damaged high-alumina brick, based on XRF assay

Chemical composition (weight %).		
Chemical species	**virgin**	**damaged**
SiO_2	13.17	14.56
Al_2O_3	74.92	78.86
Fe_2O_3	2.57	1.74
CaO	5.85	0.68
MgO	0.48	0.31
TiO_2	3.01	3.12
SO_3	-	0.20
Na_2O	-	0.25
K_2O	-	0.28
Total	100.00	100.00

The virgin and used high-alumina refractory bricks were also analysed using SEM-EDS technique (Table 5-2). The used high-alumina refractory lining analysis identified K and Na as major impurity elements. Sulphur was not detected because of its lower concentration on the scanned area.

Table 5-2. Elemental composition of virgin and damaged high-alumina powder sample, based on SEM-EDS analysis

Chemical composition (weight %).		
Elements	**Virgin**	**Damaged**
O	45.48	47.09
Mg	0.14	0.79
Al	38.61	36.60
Si	9.48	8.84
Ca	0.99	0.70
Fe	2.44	1.94
Ti	2.87	3.37
K	-	0.53
Na	-	0.14
Total	**100.00**	**100.00**

The SEM-EDS mapping of the powder sample made from the used lining is shown in Figure 5-1. It is clear that K and Na are present as impurities and will likely react with the clinker feed, the surrounding atmosphere and the high-alumina lining.

In the SEM-EDS Figure 5-1, the caption a and b represents: a) Powder sample showing particle morphology, and b) Elemental mapping showing the presence of main elements.

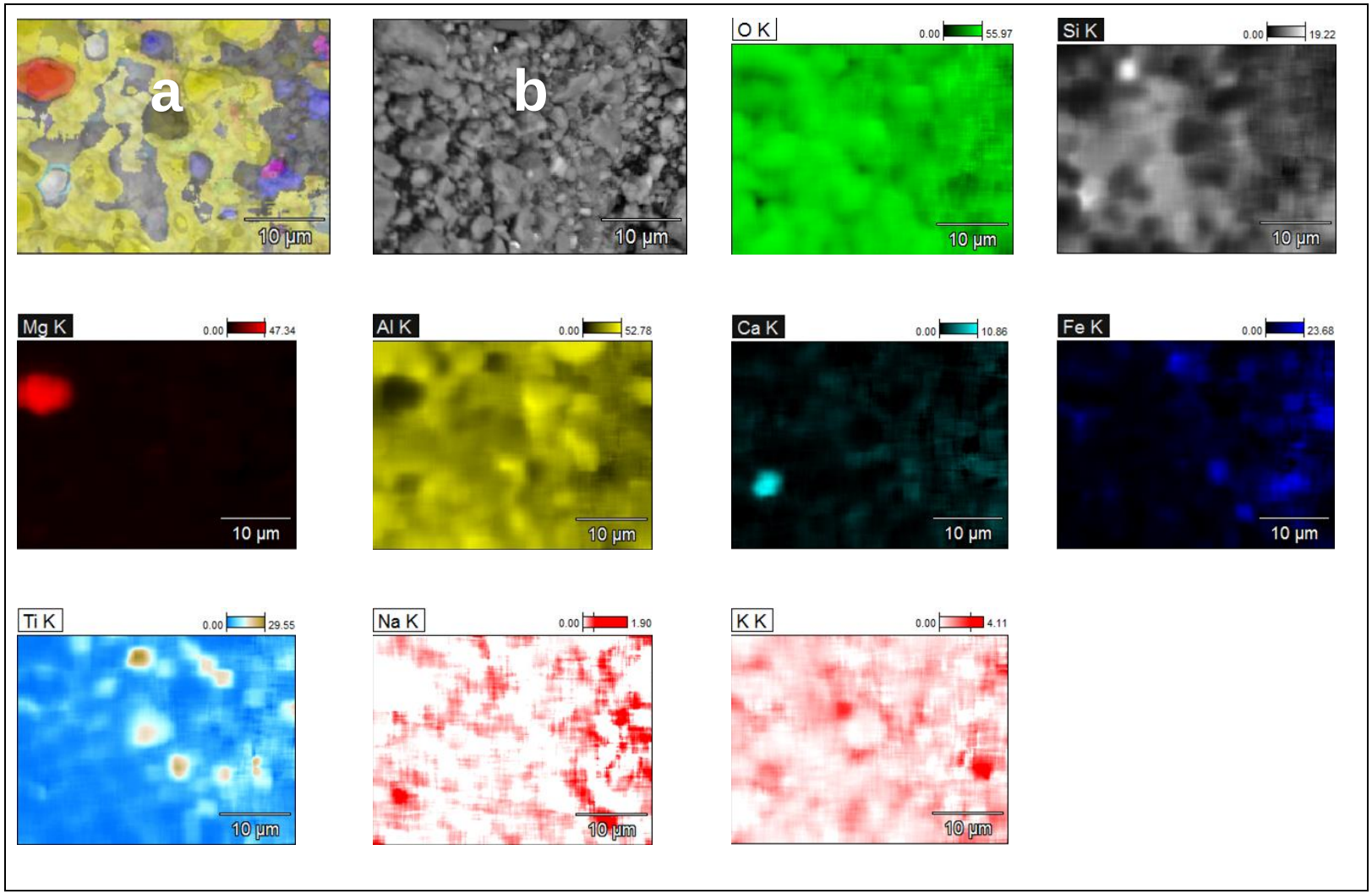


Figure 5-1. SEM-EDS mapping of the damaged high-alumina powder sample

The high-alumina refractory lining XRD raw data is provided in appendix A. The phase analysis of the virgin and used high-alumina oxide lining is shown in Table 5-3. The main phases are aluminium oxide, mullite (alumina and silica), quartz (silica), cristobalite (silica) and silimanite (alumina and silica).

Table 5-3. Phase composition of the virgin and used high-alumina lining, based on XRD analysis

Chemical composition (weight %).		
Phases	**virgin**	**damaged**
Aluminium Oxide (Al_2O_3)	35.84	42.48
Mullite ($Al(Al_{0.69}Si_{1.22})O_{4.85}$)	39.33	-
Mullite ($Al_{2.4}Si_{0.6}O_{4.8}$)	-	22.76
Cristobalite (SiO_2)	5.34	8.02
Quartz (SiO_2)		10.39
Andalusite ($Al_2(SiO_4)O$)	-	6.20
Potassium magnesium silicate ($K_2(MgSi_5O_{12})$)	-	10.16
Silimanite (Al_2SiO_5)	19.49	-
Total	**100**	**100**

Table 5-3, XRD results of the damaged high-alumina refractory brick showed the presence of contaminating phase of potassium magnesium silicate ($K_2(MgSi_5O_{12})$). This phase is a low melting phase.

The results of XRF, SEM-EDS and XRD all confirmed the presence of impurities in the damaged high-alumina lining. Evidently a chemical reaction took place

between the clinker feed, the surrounding atmosphere and the high-alumina lining as it was reported in the open literature (Bartha and Sodje., 2001, Kunnecke., 1998 and Potgieter et al., 2004).

5.3 Formation of impurity species in the damaged high-alumina brick

Chemical analysis identified SO_3, Na_2O and K_2O as the contaminating species in the damaged high-alumina refractory lining. Furthermore, XRD analysis of the damaged bricks revealed the presence of the low-melting phase $K_2(MgSi_5O_{12})$. These phase is likely formed by reaction between dust and alkalies entrained in the kiln gases and the refractory bricks in the lower transition zone (Peray and Waddell., 1972).

5.3.1 Formation of $K_2(MgSi_5O_{12})$

Potassium oxide react with the part of components of high-alumina brick and form $K_2(MgSi_5O_{12})$. This reaction can be written as follows:

$$MgO + 5SiO_2 + K_2O \rightarrow K_2(MgSi_5O_{12}) \qquad \text{E.q 5-1}$$

In general, the crystallization of salts leads to densification of the brick structure, which is accompanied by a reduction of the elasticity and thermal shock resistance of the affected parts. It was reported that the formation of $K_2(MgSi_5O_{12})$ can significantly increase the volume of the refractory brick and this

will result in the structural weakening of the brick hot face (Bartha and Sodje, 2001, Kunnecke., 1998 and Potgieter et al., 2004).

5.4 Diffusion of clinker into the high-alumina brick

SEM-EDS analysis of polished sections (Table 5-4) and powder samples (Table 5-2) and XRD results (Table 5-3) were used to investigate the mechanism of the diffusion of the liquid clinker through the grain boundaries and open pores into the used high-alumina brick the lining.

Table 5-4. Elemental composition of the damaged high-alumina polished brick section, based on SEM-EDS chemical analysis

Elements	Weight %
O	62.38
Na	0.11
Mg	0.09
Al	26.58
Si	6.30
S	0.05
K	0.44
Ca	0.50
Ti	2.52
Fe	1.03
Total	**100.00**

From Table 5-2 and 5-4, the chemical analysis of powder samples and polished sections show no presence of major clinker elements since there is no increase in Ca, Si, Al and Fe in the used refractory brick. In addition, XRD results confirm that no clinker phase diffused through in the brick. Hence, the failure of the brick cannot be explained by the clinker diffusion mechanism.

Further analysis of SEM micrographs, in Figure 5-2, revealed that no clinker diffusion into the refractory lining took place. The clinker diffusion is likely to be present as devitrified glassy phase (see figure 2-1) in the refractory materials due to refractory-clinker chemical reaction (Pena et al., 2007). There were also no longitudinal or transverse cracks in the polished sections of the used high-alumina refractory brick.

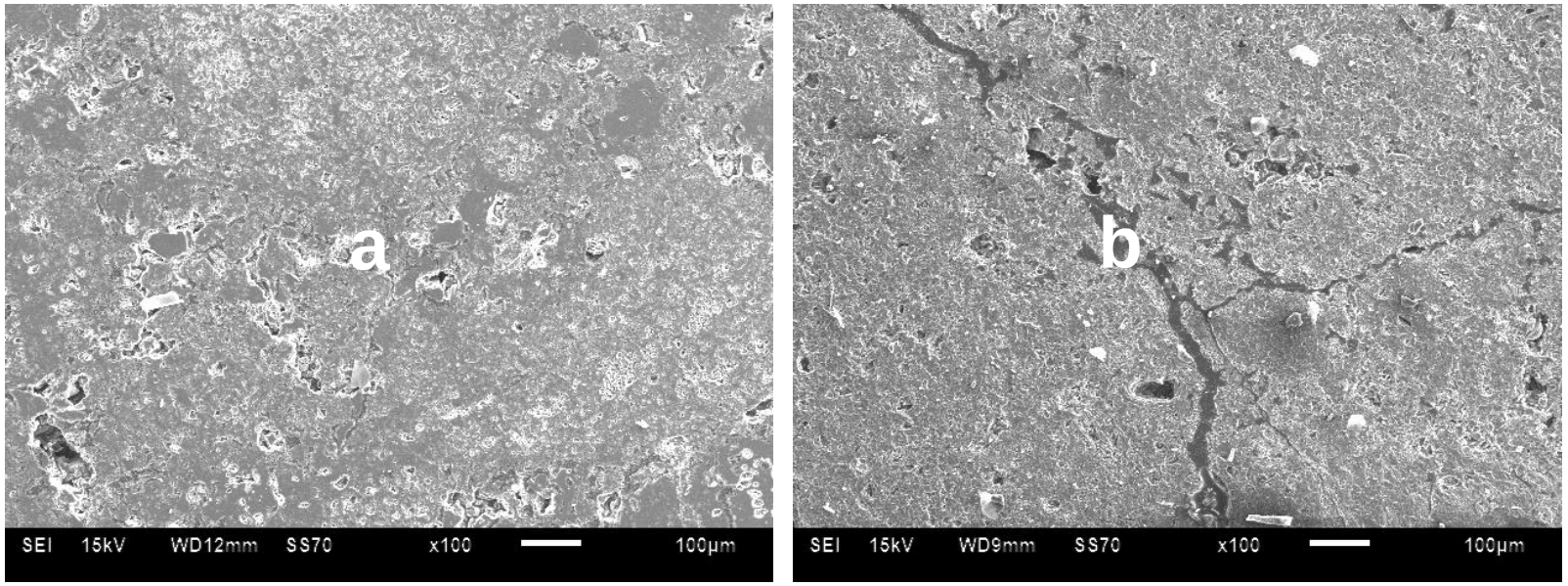


Figure 5-2. The SEM micrograph of high-alumina polished brick section, a) the unused, and b) the damaged

5.5 Microstructural examination and analysis for thermal shock attack

The thermal shock attack was studied based on SEM fracture analysis of the brick microstructures (Figure 5-3). It can be seen that there are no major cracks in both unused and used high-alumina brick sections. Fracture analysis shows similar microstructure of both unused and used high-alumina brick, they are both transgranular fracture (see Figure 2-4). The absence of micro cracks excludes thermal shock attack as a failure mechanism for the high-alumina brick.

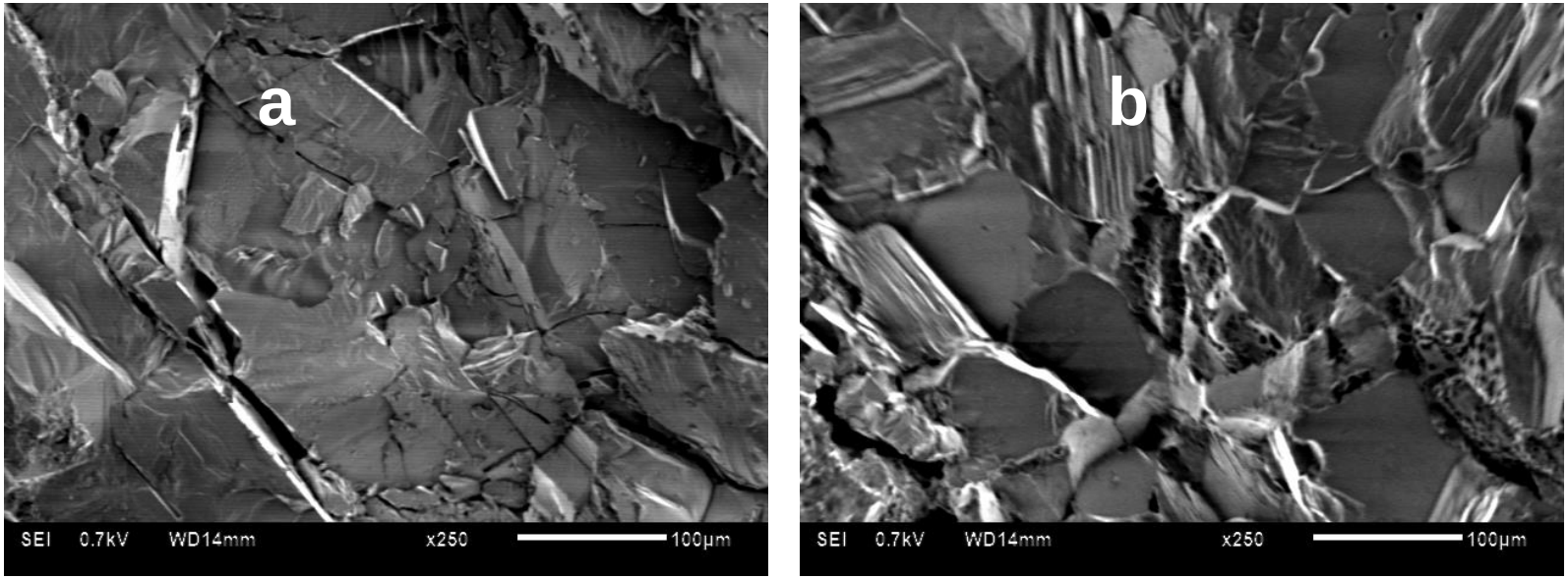


Figure 5-3. The SEM micrograph of fracture high-alumina brick, a) the unused, and b) the damaged

5.6 Thermodynamics (phase diagrams)

XRF analysis of the used high-alumina brick revealed the presence of the contaminating species SO_3, Na_2O and K_2O (Table 5-1). This led to investigate their interactions with the high-alumina refractory lining. The chemical compositions of the lining were calculated (conversion from mass % to mole %) in appendix B and expressed in terms of mole percent (Table 5-5) and referred to ternary phase diagram of impurity component – Al_2O_3 – SiO_2 or CaO.

Table 5-5 Molar composition of the damaged high-alumina lining, based on XRF assay

Mole percent.	
Chemical species	**Used high-alumina brick**
SiO_2	22.13
Al_2O_3	70.63
Fe_2O_3	0.99
CaO	1.11
TiO_2	0.70
MgO	3.57
SO_3	0.23
Na_2O	0.37
K_2O	0.27
Total	**100.00**

5.6.1 Effect of sulphur trioxide (SO_3)

The ternary phase diagram of Al_2O_3-CaO-SO_3 system at 1200^oC, in Figure 5-4, was used to illustrate the effect of SO_3 on the lining properties.

Table 5-6. Normalised composition of the damaged high-alumina brick, for SO_3 effect

Mole %.	
Chemical species	**Damaged High-alumina brick**
Al_2O_3	98.14
CaO	1.54
SO_3	0.32
Total	**100.00**

The normalised composition of the damaged high-alumina lining falls within the phase field $Al_2O_{3\,(s)}$ + $CaAl_{12}O_{19\,(s)}$ + $CaSO_{4\,(s)}$ (Point P).

At point L, only $CaAl_{12}O_{19}$ and Al_2O_3 exist. Moving along the SO_3 line (red line) there is phase transformation. The effect of SO_3 is the formation of $CaSO_{4\,(s)}$ which compromise the refractoriness of the high-alumina brick.

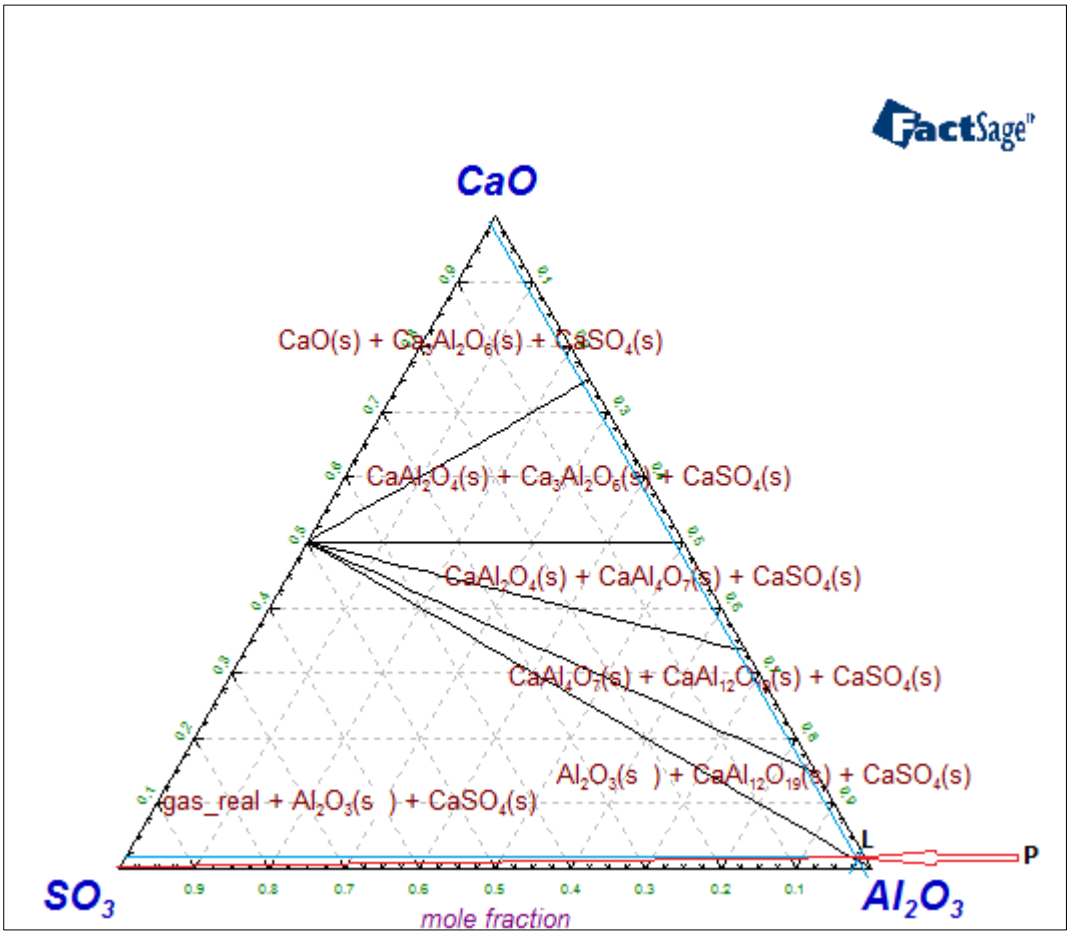


Figure 5-4. System Al_2O_3-CaO-SO_3 ternary phase diagram at 1200ºC and 1 atmosphere

5.6.2 Effect of sodium oxide

The interaction of sodium oxide with the refractory lining was studied by using the ternary phase diagram of Al_2O_3-SiO_2-Na_2O system at 1200^oC (Figure 5-5). The re-drawn phase diagram for clarity is provided in Figure 5-6.

Table 5-7. Normalised composition of the damaged high-alumina brick, for Na_2O effect

Mole %.	
Chemical species	**Damaged High-alumina brick**
Al_2O_3	75.84
SiO_2	23.76
Na_2O	0.40
Total	**100.00**

The normalised composition of the damaged high-alumina lining falls within the phase field of Al_2O_3 + $Al_6Si_2O_{13}$ + $Na_2O_{(liq)}$ (Point E). At point E, Al_2O_3, SiO_2 and Na_2O react to form Na_2O (liquid), $Al_6Si_2O_{13}$ and free Al_2O_3, the reaction is:

$$4Al_2O_3 + 2SiO_2 + Na_2O \rightarrow Na_2O\ (liquid) + Al_6Si_2O_{13} + Al_2O_3 \qquad \text{E.q 5-2}$$

At point F only $Al_6Si_2O_{13}$ and free Al_2O_3 exist. Moving along Na_2O line (red line) through composition at point E, a phase transformation occurs as the amount of Na_2O increases. The free Al_2O_3 and $Al_6Si_2O_{13}$ decreases with an increase in Na_2O, forming liquid slag.

The presence of Na_2O content at any given concentration in the high-alumina brick automatically result in liquid formation in the brick. This liquid formation will result in premature failure of the high-alumina brick.

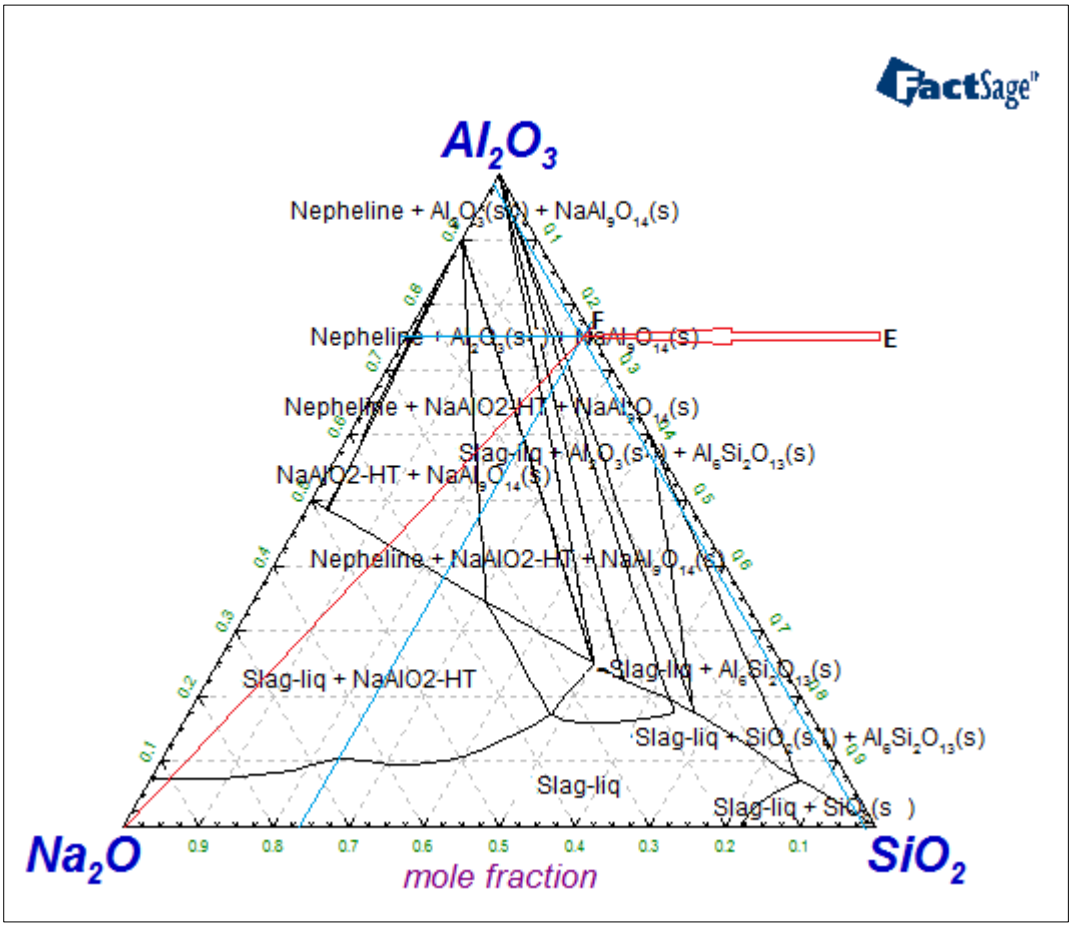


Figure 5-5. System Al_2O_3-SiO_2-Na_2O ternary phase diagram at 1200ºC and 1 atmosphere

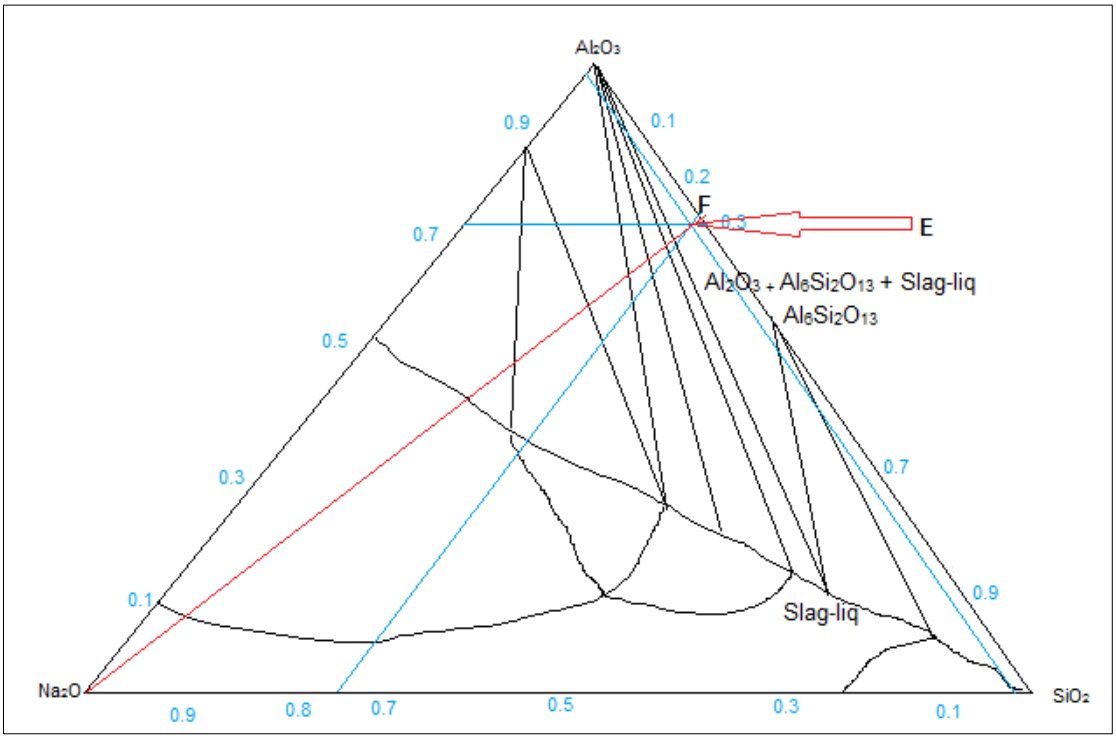


Figure 5-6. System Al_2O_3-SiO_2-Na_2O ternary phase diagram at 1200ºC and 1 atmosphere

5.6.3 Effect of potassium oxide (K_2O)

The normalised composition of the damaged high-alumina refractory lining was plotted in the Al_2O_3-SiO_2-K_2O system in order to investigate the effect of potassium oxide on the properties of the lining. The re-drawn phase diagram for clarity is provided in Figure 5-8.

Table 5-8. Normalised composition of the damaged high-alumina brick, for K_2O effect

Mole %.	
Chemical species	**Damaged High-alumina brick**
Al_2O_3	75.92
SiO_2	23.79
K_2O	0.29
Total	**100.00**

The composition falls within the phase field of Al_2O_3 + $Al_6Si_2O_{13}$ + $KAlSi_2O_6$ (Point K). At point K, Al_2O_3, SiO_2 and K_2O react to form Al_2O_3, $Al_6Si_2O_{13}$ and $KAlSi_2O_6$, the reaction is:

$$5Al_2O_3 + 6SiO_2 + K_2O \rightarrow Al_2O_3 + Al_6Si_2O_{13} + 2KAlSi_2O_6 \qquad \text{E.q 5-3}$$

At point R, only $Al_6Si_2O_{13}$ and Al_2O_3 exist. Moving along K_2O line (red line) through composition point K, a phase transformation occurs as the amount of K_2O increases. The free Al_2O_3 and $Al_6Si_2O_{13}$ decreases with an increase in K_2O, forming $KAlO_2$ and liquid-slag.

The effect of potassium oxide is affected by the formation of $KAlSi_2O_6$ which promotes liquid formation when K_2O content increases in the high-alumina

lining. These phase transformations to slag-liquid result in premature failure of the high-alumina brick.

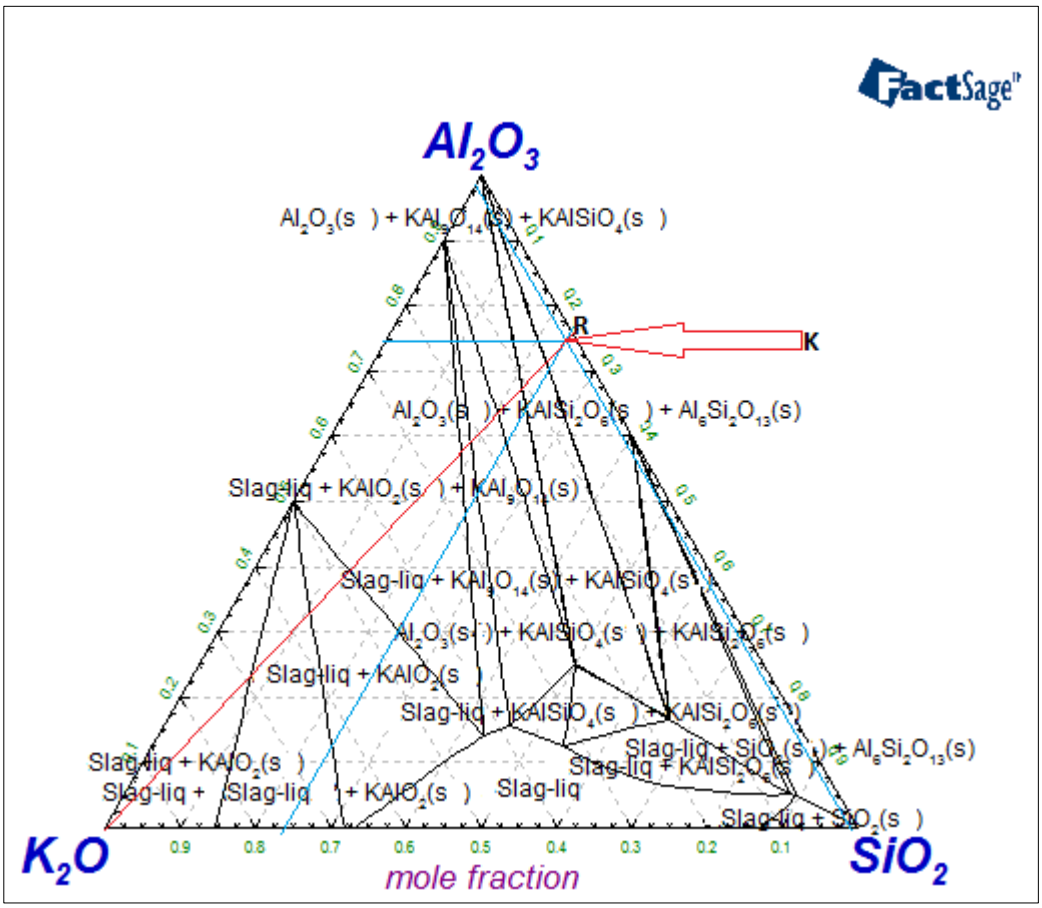


Figure 5-7. System Al_2O_3-SiO_2-K_2O ternary phase diagram at 1200ºC and 1 atmosphere

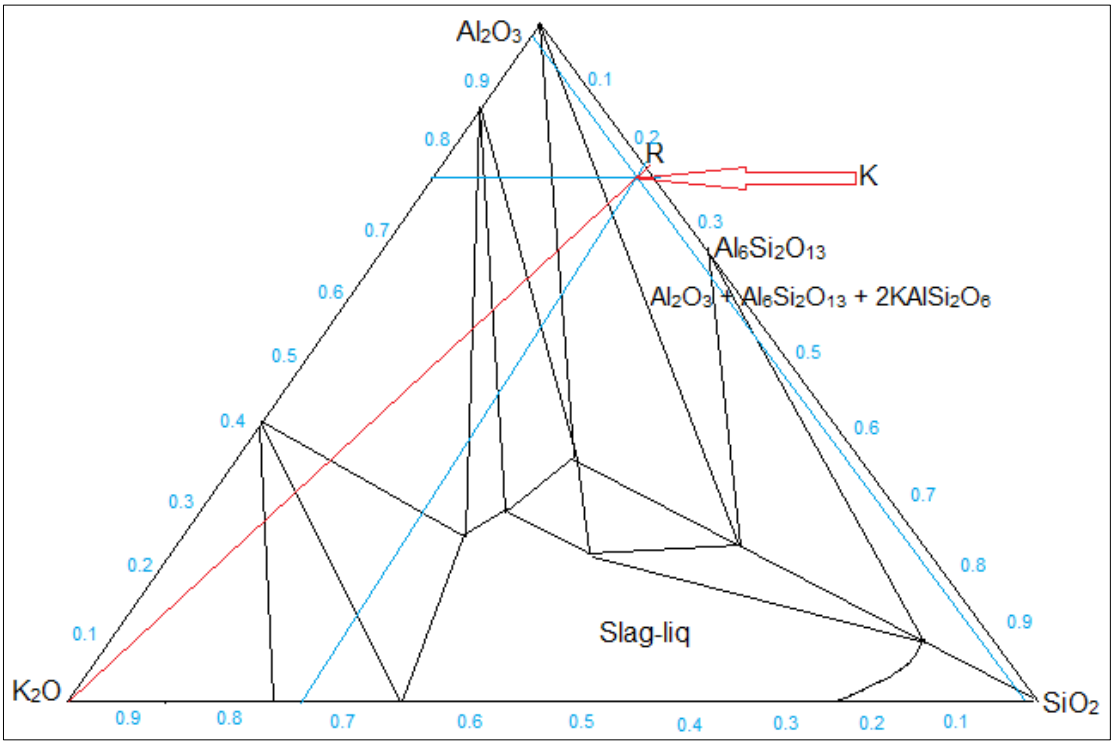


Figure 5-8. System Al_2O_3-SiO_2-K_2O ternary phase diagram at 1200ºC and 1 atmosphere

5.7 Conclusion

The mechanisms for failure of the high-alumina brick were established from chemical analysis, post-mortem microstructural examinations and ternary phase diagram predictions.

Chemical analysis of used high-alumina lining revealed the presence of alkalis and sulphur impurities. Phase diagram predictions indicated that the presence of sodium at any given concentration automatically results in liquid formation in the brick. It is evident that chemical attack can be one of the causes of the high-alumina brick failure.

The microstructural examination of the used brick sections showed an absence of clinker in the used high-alumina brick. Hence the failure of the brick cannot be caused by clinker diffusion mechanism.

Further microstructural examination revealed there was no change in the fracture mode of the brick which remains transgranular. No major cracks were observed. Therefore the thermal shock cannot explain the failure mechanism of the high-alumina brick.

CHAPTER SIX

6 RESULTS AND DISCUSSION: EFFECT OF PARTIAL PRESSURE OF OXYGEN

6.1 Introduction

The operating conditions in the kiln were investigated through the effect of partial pressure of oxygen on the behaviour of the refractory lining. The oxygen potential is very important to regulate the stability of the oxides that are the main components of the refractory materials. For instance, low oxygen partial pressure can lead to the reduction of some oxides into a lower oxide or even to metal element, resulting in the failure of the lining structure.

6.2 Calculation of the oxygen partial pressure

The partial pressure of oxygen influences oxidation or reduction of oxides in the refractory lining. It is evident that high oxygen partial pressure is associated with oxidizing conditions while low values of oxygen partial pressure are referred to as reducing environment. In practice, partial pressure of oxygen is determined by the ratio of two gaseous species in a buffer mixture, such as CO_2/CO (Azad, 2006).

In the burning zone (1500ºC), the oxygen partial pressure defined by these two gases via $2CO_{(g)} + O_{2(g)} = 2CO_{2(g)}$ (E.q 2-10)

Hence, oxygen partial pressure can be expressed as follows:

$$PO_2 = \left(\frac{PCO_2}{PCO}\right)^2 \frac{1}{e^{-2\Delta G^\circ/RT}} \qquad \text{E.q 6-1}$$

where ΔGº is the free energy change of CO, CO_2 and O_2 gases as given in equation 2-9 ($\Delta G^\circ\ (J) = -282{,}400\ + 86.81T$) (Azad, 2006).

In this study, the calculation of the oxygen partial pressure was firstly based on the ratio of the two gases taken at the kiln back end where the temperature is about 800°C. The average ratio of CO_2 to CO at 800°C is given in Table 6.1.

Table 6-1: Volume percent of CO_2 and CO, measured from industrial kiln

Gas	%
CO_2	7.06
CO	0.1
CO_2/CO	70.6

The partial pressure of oxygen at 800ºC is calculated as follows:

$$\Delta G^\circ\ (1073) = -282{,}400\ + 86.81T$$

$$\Delta G^\circ\ (1073) = -189\ 252.87\ J/mol$$

Given in E.q 2-7,

$$\Delta G^\circ = -RTln\frac{PCO_2}{PCOPO_2{}^{½}}$$

Therefore, the partial pressure of oxygen is:

$$-189\ 252.87\ = -8.312 \times 1073\ln(\frac{7.06}{0.1}\ \times \frac{1}{PO_2{}^{½}})$$

$$21.2196 = \ln\left(\frac{7.06}{0.1}\right) - \ ½\ln PO_2$$

$$½\ln PO_2 = \ -16.96256986$$

$$PO_2 = \ 1.8471 \times 10^{-15}\ atm$$

The partial pressure of oxygen at 1500ºC is calculated as follows:

$$\Delta G°\ (1773) = -282{,}400\ + 86.81T$$

$$\Delta G°\ (1773) = -128\ 485.87\ J/mol$$

Given in E.q 2-7,

$$\Delta G° = -RTln\frac{PCO_2}{PCOPO_2{}^{½}}$$

Therefore, the partial pressure of oxygen is:

$$-128\ 485.87\ = -8.312 \times 1773\ln(\frac{7.06}{0.1}\ \times \frac{1}{PO_2{}^{½}})$$

$$8.7185 = \ln\left(\frac{7.06}{0.1}\right) - \ ½\ln PO_2$$

$$½\ln PO_2 = \ -4.4615$$

$$PO_2 = \ 1.3330 \times 10^{-4}\ atm$$

It is clear that the reactions of reduction are predominant in the burning zone due to lower value of oxygen partial pressure.

6.3 Stability of oxides in the refractory lining

In burning zone, the oxides that are likely to be instable in the refractory materials are Fe_2O_3 and Mn_2O_3. These oxides can be involved in oxidation reaction where the oxygen partial pressure is the determinant factor.

To assess the stability of these oxides, Standard Gibb's free energy change at equilibrium and that of the oxidation reaction were compared for burning zone conditions (1500ºC).

6.3.1 Reduction of Hematite (Fe_2O_3)

The reaction for the reduction of hematite is given in equation 6-2

$$2Fe_3O_4 + ½O_2 = 3Fe_2O_3 \qquad \text{E.q 6-2}$$

To determine the free energy change, $\Delta G°$ or the reaction the following equations were used.

$$3Fe + 2O_2 = Fe_3O_4 \qquad \text{E.q 6-3}$$

$\Delta G° = -1103120 - (-307.378T)$ J/mol (Hayes, P.C. (2003))

$$\Delta G° = -558138.806\, J/mol$$

$$2Fe + \frac{3}{2}O_2 = Fe_2O_3$$ E.q 6-4

$\Delta G° = -815023 - (-251.117T)$ J/mol (Hayes, P.C. (2003))

$\Delta G° = -369792.552\, J/mol$

Thus the Standard Free Energy for reaction 6-2 at 1773K will be:

$\Delta G° = 3 \times \Delta G°(E.q\ 6-4) - 2 \times \Delta G°(E.q\ 6-3)$

$\Delta G° = -1109377.656 + 1116277.612$

$\Delta G° = 6899.956\, J/mol$

The generalized statement can be represented by a generalized Gibb's free energy change, $\Delta G°$ for a system not at standard condition, but whose reaction quotient is Q. Obviously, the formulation is

$$\Delta G = \Delta G° + RTlnQ$$ E.q 6-5

$\Delta G = 6899.956 + 8.312 \times 1773\ln(\frac{1}{PO_2{}^{½}})$

$\Delta G = 6899.956 + 8.312 \times 1773\ln\frac{1}{(1.3330\times10^{-4})^{½}}$

$\Delta G = 72649.19\, J/mol$

The reaction for the oxidation of magnetite to hematite cannot take place when the oxygen partial pressure is 1.3330 × 10^{-4} at 1773K but obviously the reverse reaction should be feasible, i.e. reduction of hematite to magnetite.

6.3.2 Reduction of Mn_2O_3

The reaction for the reduction of Mn_2O_3 is given in equation 6-6

$$2Mn_3O_4 + ½O_2 = 3Mn_2O_3 \qquad \text{E.q 6-6}$$

To determine the free energy change, $\Delta G°$ or the reaction the following equations were used.

$$3Mn + 2O_2 = Mn_3O_4 \qquad \text{E.q 6-7}$$

$\Delta G° = -1384904 - (-344.427T)$ J/mol (Hayes, P.C. (2003))

$\Delta G° = -774234.929\, J/mol$

$$2Mn + \frac{3}{2}O_2 = Mn_2O_3 \qquad \text{E.q 6-8}$$

$\Delta G° = -953952 - (-255.224T)$ J/mol (Hayes, P.C. (2003))

$\Delta G° = -501439.848\, J/mol$

Thus the Standard Free Energy for reaction 6-6 at 1773K will be:

$\Delta G° = 3 \times \Delta G°(E.q\ 6-8) - 2 \times \Delta G°(E.q\ 6-7)$

$$\Delta G° = -1504319.544 + 1548469.858$$

$$\Delta G° = 44150.314\, J/mol$$

The generalized statement can be represented by a generalized Gibb's free energy change, $\Delta G°$ for a system not at standard condition, but whose reaction quotient is Q. Obviously, the formulation is

$$\Delta G = \Delta G° + RTlnQ \qquad \text{E.q 6-9}$$

$$\Delta G = 44150.314 + 8.312 \times 1773 \ln\left(\frac{1}{PO_2{}^{½}}\right)$$

$$\Delta G = 44150.314 + 8.312 \times 1773 \ln \frac{1}{(1.3330 \times 10^{-4})^{½}}$$

$$\Delta G = 109915.370\, J/mol$$

The reaction for the oxidation of Mn_3O_4 to Mn_2O_3 cannot take place when the oxygen partial pressure is 1.3330×10^{-4} at 1773K but obviously the reverse reaction should be feasible, i.e. reduction of Mn_2O_3 to Mn_3O_4.

6.3.3 Conclusion

The partial pressure of oxygen is low in the vicinity of the burning zone. This means that the reactions of oxidation magnetite to hematite and Mn_3O_4 to Mn_2O_3 cannot take place and affect the failure of the refractory.

CHAPTER SEVEN

7 CONCLUSIONS AND RECOMMENDATIONS

7.1 Introduction

In the cement industries, the refractory materials are required to have specific qualities to sustain the operating conditions in the rotary kiln. The refractory materials must be able to resist high temperatures and chemical attack. In addition the refractory must be able to resist spalling and abrasion. The main objective of this work was to establish the main causes of the refractory material failure.

Previous works identified the failures of refractory materials in rotary cement kilns under controlled conditions in the laboratory. However, this study took a different approach by investigating the failure mechanisms using post-mortem refractory materials samples collected from the industrial kiln. The results of the current research provided a framework where the failure of the refractory brick cannot be explained by a single mechanism rather by different mechanisms such as effect of impurities, effect of kiln operating conditions and alkali sulphate ratio.

7.2 Effect of impurities

XRF and SEM-EDS analysis revealed that the tested refractory materials are contaminated by four major impurities: sodium, potassium, chlorine and sulphur.

The XRD analysis of the damaged magnesia-spinel and magnesia-fused spinel refractory bricks which were applied at the burning zone revealed that the refractory bricks suffered chemical attack. Most damaged magnesia-spinel and magnesia-fused spinel showed the presence of low-melting phases (KCl, (Na, K) Cl, $CaSO_4$ and K_2SO_4), which have adverse effects on the refractoriness of the magnesia bricks.

Based on the ternary phase diagrams, the interactions between impurities and refractory bricks indicated a decrease in the refractoriness of the refractory materials. Even at low concentration, the presence of different impurities in the bricks reduced the liquidus temperature of the refractory by forming liquid-slag phases. The formation of these low meting point phases resulted in chemical attack of the magnesia bricks.

The chemical analysis of the used high-alumina refractory brick which was applied at the lower transition zone showed sodium, potassium and sulphur as impurities. XRD analysis showed the presence of low-melting phase (K_2 ($MgSi_5O_{12}$) which compromises the refractoriness of the high-alumina brick. The interactions between impurities and the refractory lining indicated that the presence of sodium oxide resulted in liquid formation in the high-alumina brick. It was also found that that higher sulphur and potassium content compromise the refractoriness of the lining. This brick also suffered chemical attack.

7.3 Thermal shock attack

The failure by thermal shock attack was essentially studied based on the SEM microstructure of polished cross-sections of different bricks. The SEM micrographs showed no major cracks in all damaged magnesia brick sections. Fracture is intergranular in all magnesia bricks. Hence cracks does not easily propagate and thermal shock attack could not be described as a major source of the refractory bricks failure

In the high-alumina brick, SEM micrographs of polished sections showed clearly that there are no major cracks observed. The fracture is transgranular in all high-alumina bricks. Without evidence of major cracks in the high alumina brick, thermal shock attack could not be described as a major source of the high-alumina brick failure.

7.4 Corrosion by clinker

Microstructural examination and analysis of all unused, damaged and used refractory materials (magnesia-spinel, magnesia-fused spinel and high-alumina) revealed no evidence of clinker diffusion. No clinker phases could be observed in the refractory materials. In addition there was no observation made of longitudinal or transverse cracks. It can be concluded that the failure of all the refractory materials was not influenced by the clinker diffusion.

7.5 Effect of kiln operating conditions

The partial pressure of oxygen is low in the vicinity of the burning zone. Therefore the reactions of oxidation magnetite to hematite and Mn_3O_4 to Mn_2O_3 are not possible. It was established that the stability of these oxides (Fe_3O_4 and Mn_3O_4) will positively contribute to that of the entire refractory brick.

7.6 Alkali sulphate ratio

The alkali sulphate ratio was mostly outside the recommended range of 0.8-1.2. This indicates that the kiln was operated in conditions where chemical attack was favoured.

7.7 Recommendations

This study found that the refractory materials investigated suffered chemical attack due to impurities that were analysed in the rotary cement kiln feed materials.

The following are recommendations to address the refractory lining failure:

i. The alkali sulphate ratio (ASR) must be controlled at a recommended range of 0.8-1.2 to continuously prevent chemical attack.
ii. The feeding of materials with impurities (Cl, S, Na and K) must be avoided or minimized to prevent the formation of low-melting phases.

iii. The refractory lining selection must be guided by its properties and the area of application in the rotary cement kiln. The refractory must be able to resist chemical and thermal shock attack.

iv. The partial pressure of oxygen in the kiln must be controlled to prevent phase transformation of refractory materials which weakens the refractory brick structure.

v. Magnesia zirconia brick is recommended for use in the burning zone. This brick has far superior properties compared to that of magnesia bricks. The use of Magnesia-zirconia brick will prevent chemical attack and thermal shock attack.

vi. The high-alumina brick was the least affected brick in this study and it is recommended to be used in the lower transition zone.

REFERENCES

Aksel, C., Rand, B., Riley, F.L., Warren, P.D. (2004a). Thermal shock behaviour of magnesia–spinel composites. *Journal of the European Ceramic Society*, no. 24, pp. 2839-2845.

Aksel, C., Riley, F.L. (2003). Effect of the particles size distribution of spinel on the mechanical properties and thermal shock performance of MgO-spinel composites. *Journal of the European Ceramic Society*, no. 23, pp. 3079-3087.

Aksel, C., Warren, P.D., Riley, F.L. (2004b). Fracture behaviour of magnesia and magnesia-spinel composites before and after thermal shock. *Journal of the European Ceramic Society*, no. 24, pp. 2407-2416.

Alsop, P. A., (1998). *The cement plant operations*. 2nd Edition, Tradeship Publications Ltd., Houston.

Azad, A. (2006). Fine-tuning of ceramic-based chemical sensors via novel microstructural modification. Part II: Low level CO sensing by molybdenum oxide, MoO_3. *Sensors and Actuators B 120*, pp. 25-34.

Bartha, P., Sodje, J. (2001). *Degradation of refractories in cement rotary kilns fired with waste fuels*. Report no.61, Vol.5, pp. 64-72, Refratechnik, Gottingen.

Caballero, A., Serena, S., Sainz, M.A. (2009). The system Clinker-MgO-$CaZrO_3$ and its application to the corrosion behaviour of $CaZrO_3$/MgO refractory matrix by clinker. *Journal of the European Ceramic Society*, no. 29, pp. 2199-2209.

Ghosh, A., Sarkar, R., Mukherjee, B., Das, S.K. (2004). Effect of spinel content on the properties of magnesia–spinel composite refractory. *Journal of the European Ceramic Society*, no. 24, pp. 2079–2085.

Gilchrist, J.D. (1977). *Fuels, Furnace and Refractories*. Pergamon press, Newcastle.

Hayes, P.C. (2003). *Process principles in minerals and materials production.* Third edition, Hayes publishing co., Queensland.

Kunnecke, M. (1998). *Wear phenomena of refractory linings in the burning zone of rotary cement kilns*. Report no.5, Refratechnik, Gottingen.

Obregon, A., Rodriquez-Galicia, J.L., Lopez-Cuevas, J., Pena, P., Baudin, C. (2011). MgO-CaZrO3-based refractories for cement kilns. *Journal of the European Ceramic Society*, no. 31, pp. 61-74.

Pena, P., Rodriguez-Galicia, J.L., De Aza, A.H., Rendon-Angeles, J.C. (2007). The Mechanism of corrosion of MgO-$CaZrO_3$-calcium silicate materials by cement clinker. *Journal of the European Ceramic Society*, no. 27, pp. 79–89.

Peray, K.E., Waddell, J.J. (1972). *The rotary cement kiln*. Chemical publishing Co., New York., pp. 1 – 23.

Potgieter, J.H., Godoi, R.H.M., Van Grieken, R. (2004). A case study of high-temperature corrosion in rotary cement kilns. *Journal of the South African Institute of Mining and Metallurgy*, pp. 603–606.

Riley, F.L., Aksel, C., Rand, B., Warren, P.D. (2002). Mechanical properties of magnesia-spinel composites. *Journal of the European Ceramic Society*, no. 22, pp. 745-754.

Serena, S., Sainz, R.M., Caballero, A. (2004). Corrosion behaviour of $MgO/CaZrO_3$ refractory matrix by clinker. Journal of the European Ceramic Society, no. 24, pp. 2399–2406.

Szczerba, J. (2010). Chemical corrosion of basic refractories by cement kiln materials. Ceramic International, no. 36, pp. 1877-1885.

Taylor, H.F., 1997. *Cement chemistry*. 2nd Edition, Thomas Telford Services Ltd, Aberdeen.

APPENDICES

APPENDIX A: XRD RESULTS

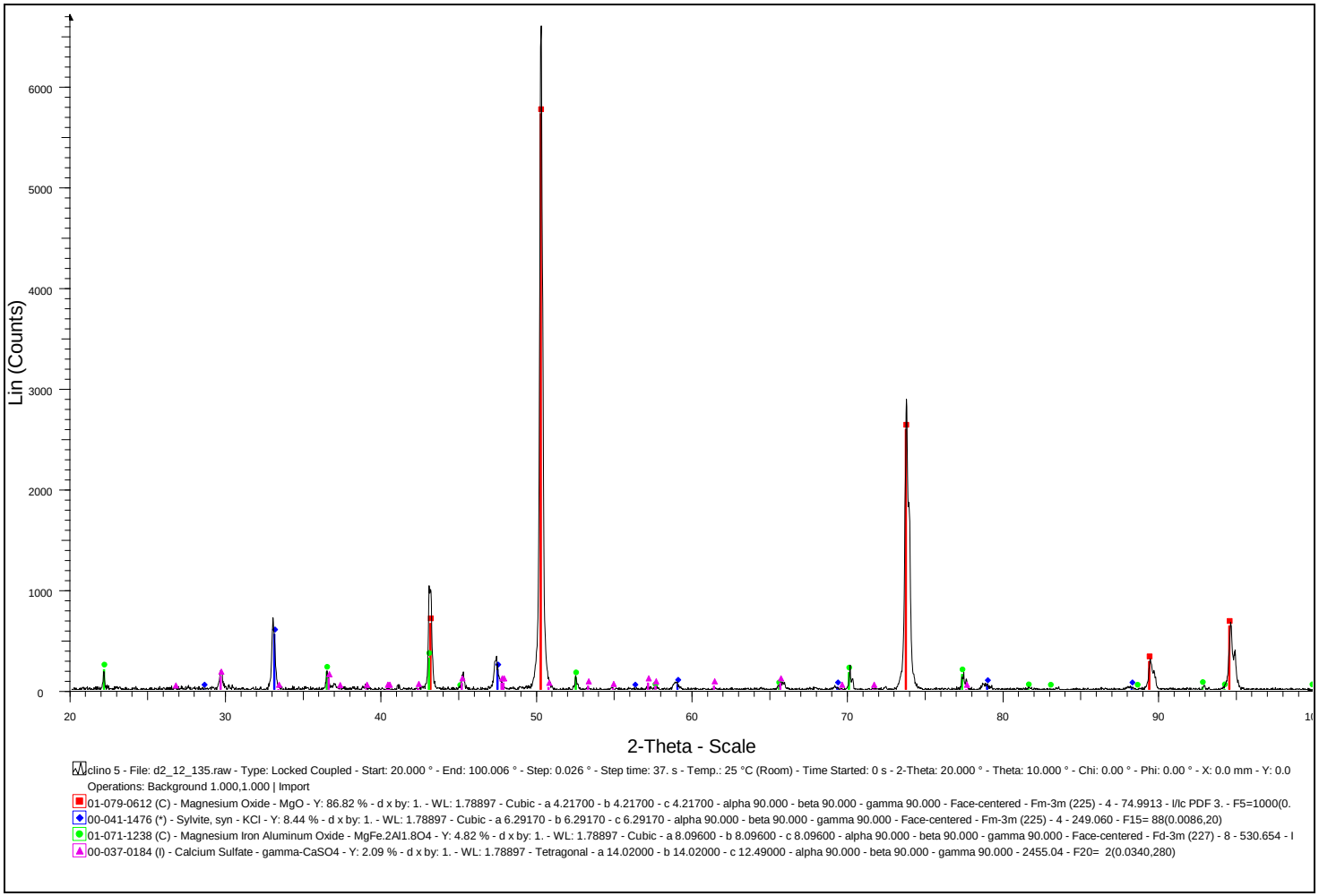


Figure A 1 Magnesia-spinel brick type A – Used

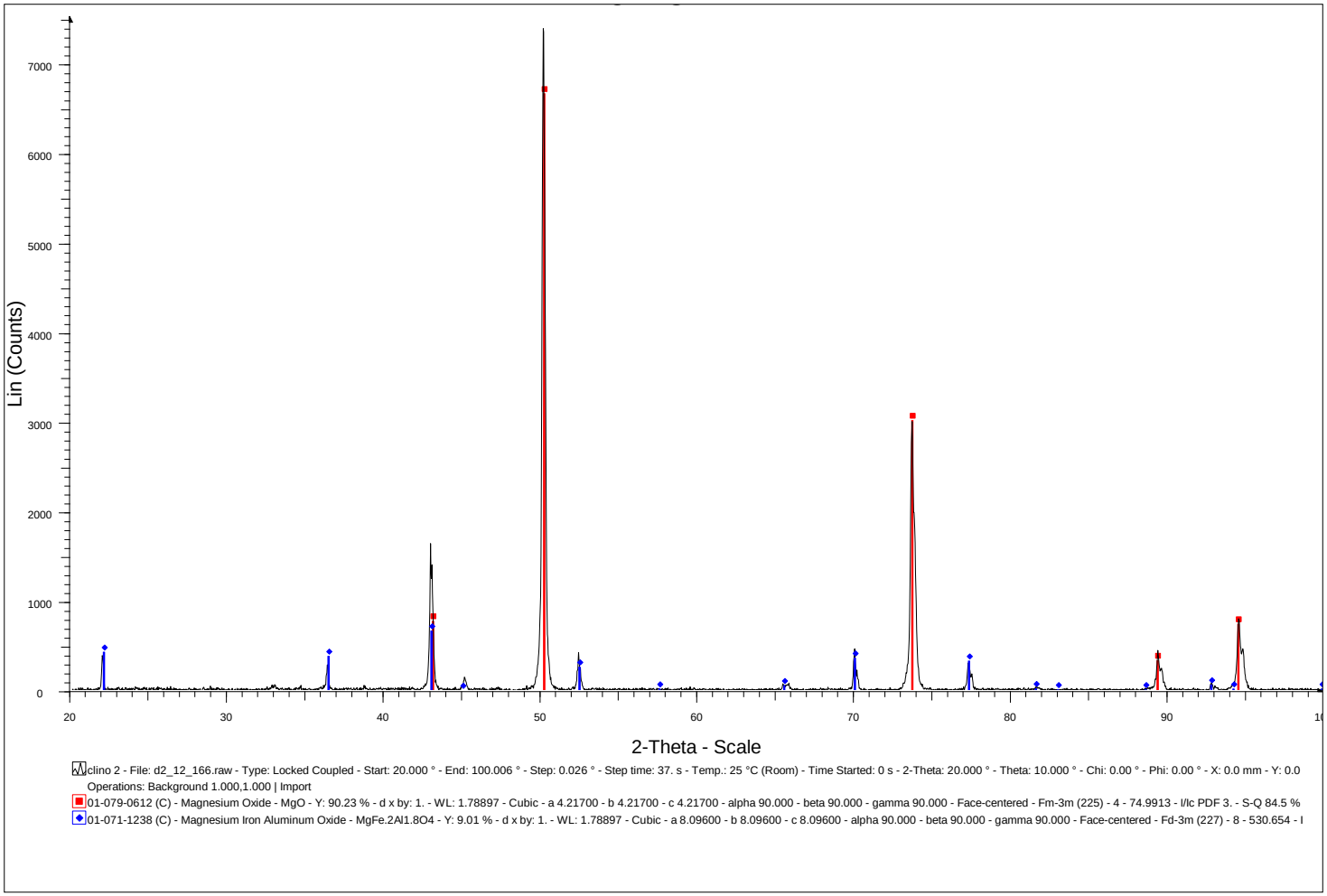


Figure A 2 Magnesia-spinel brick type A – unused

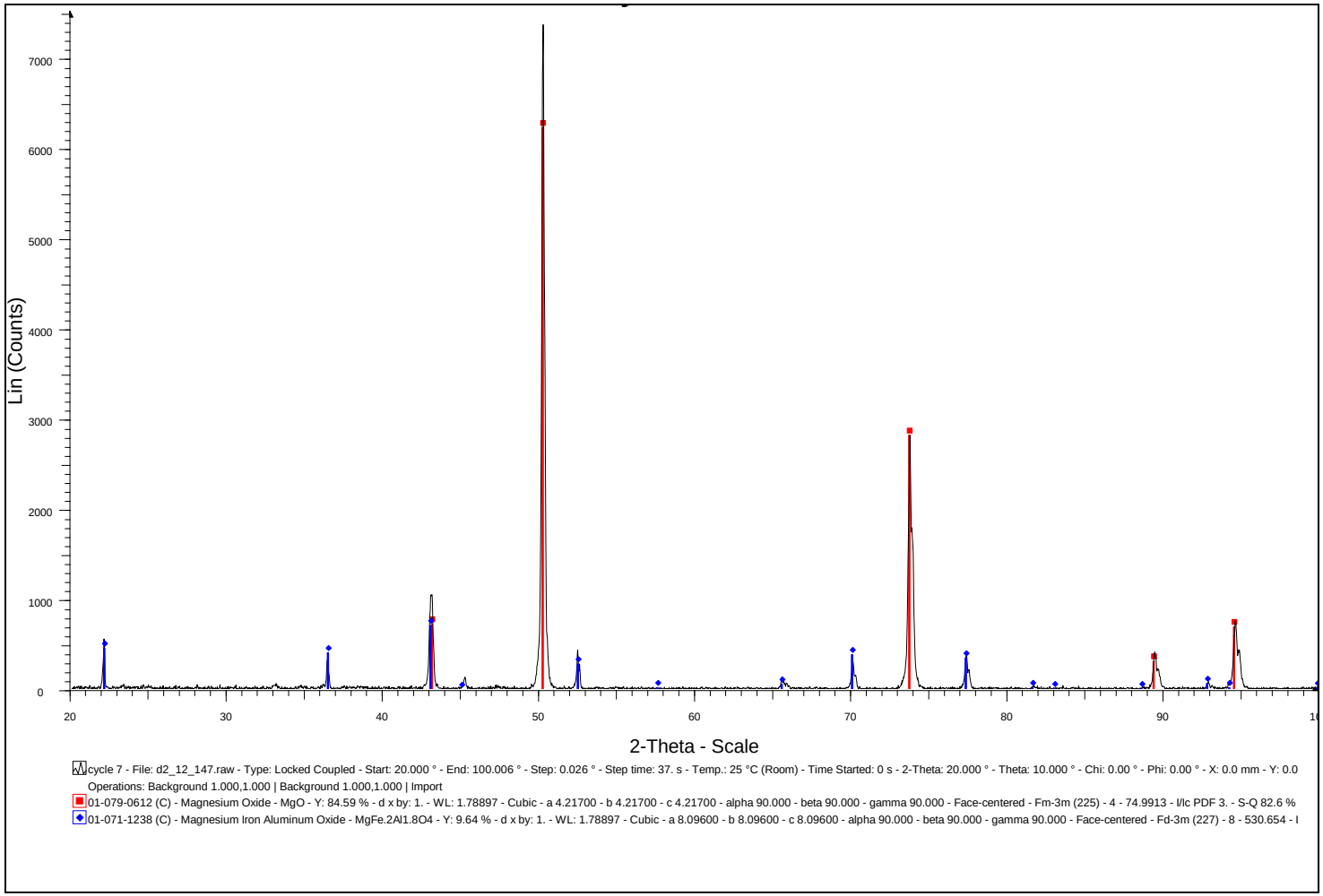


Figure A 3 Magnesia-spinel brick type B - unused

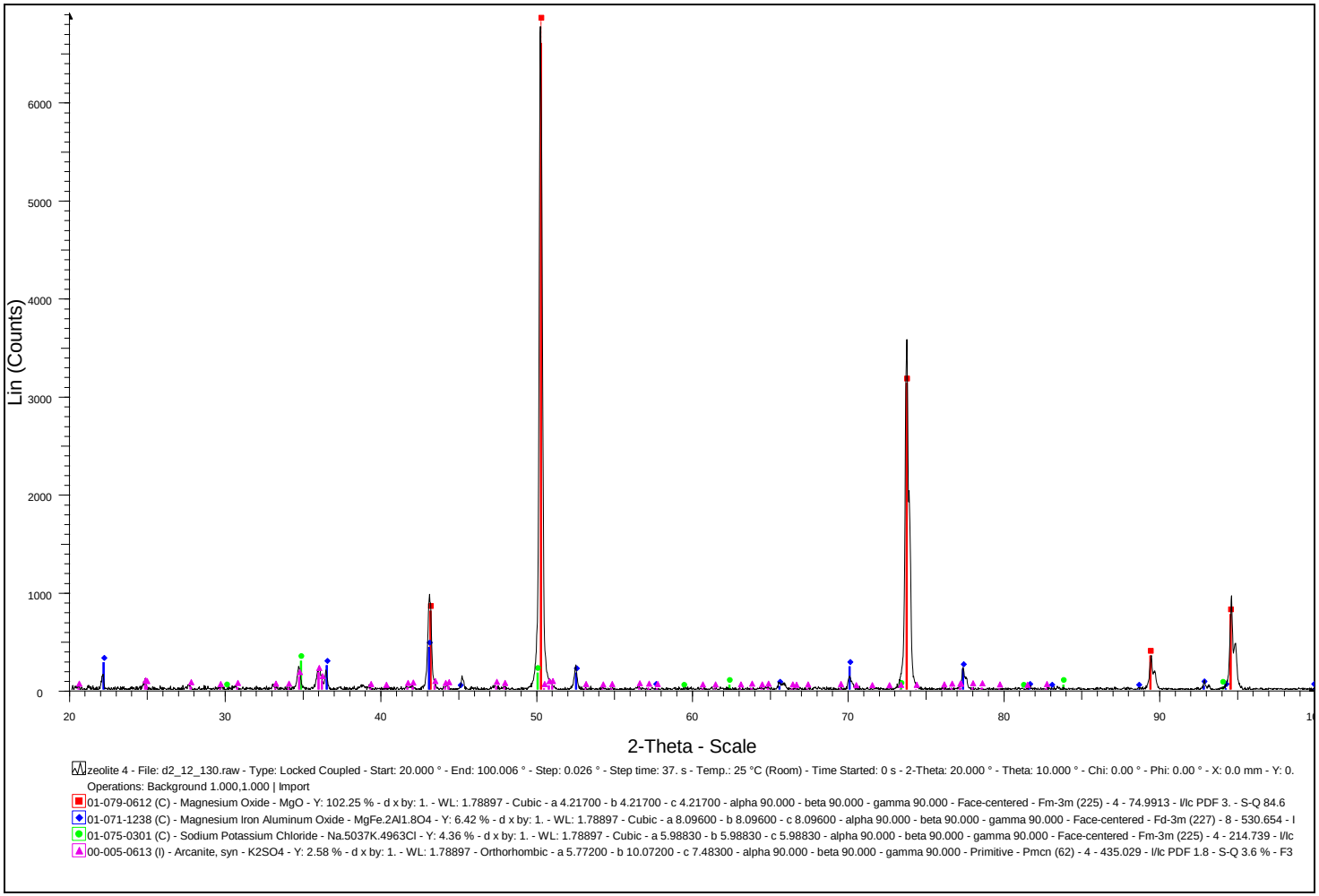


Figure A 4 Magnesia-spinel brick type B – used

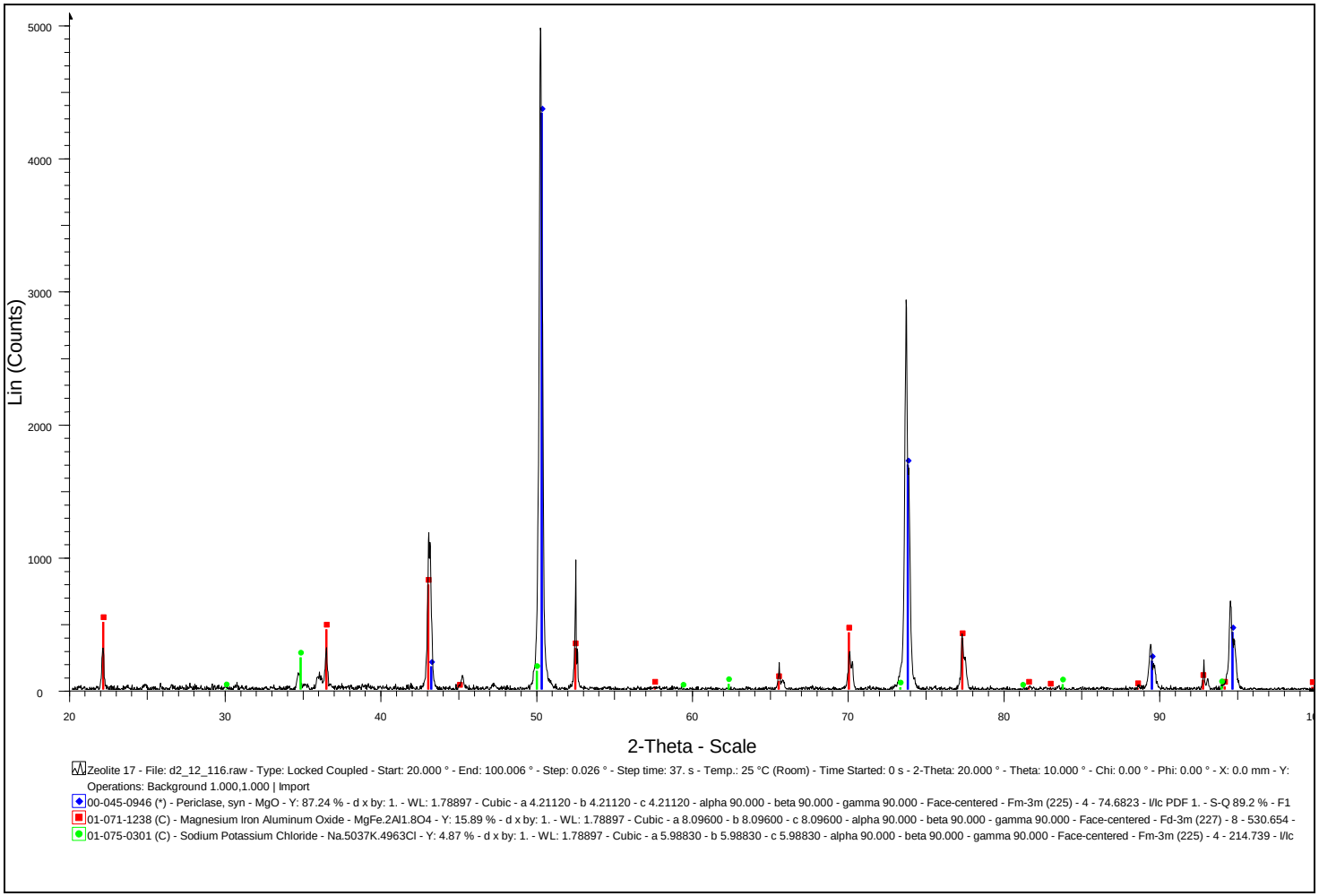


Figure A 5 Magnesia-fused spinel used brick

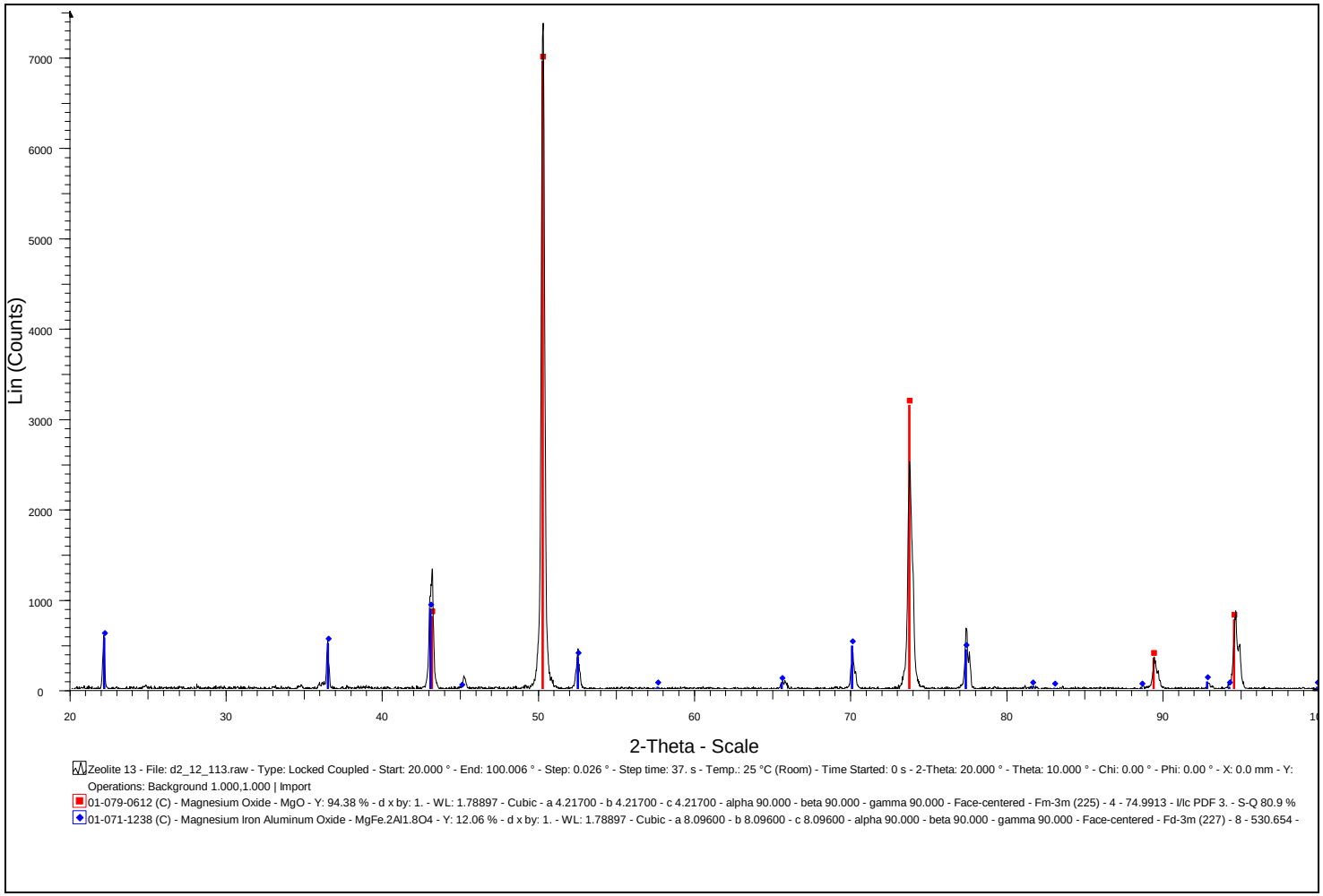


Figure A 6 Magnesia-fused spinel unused

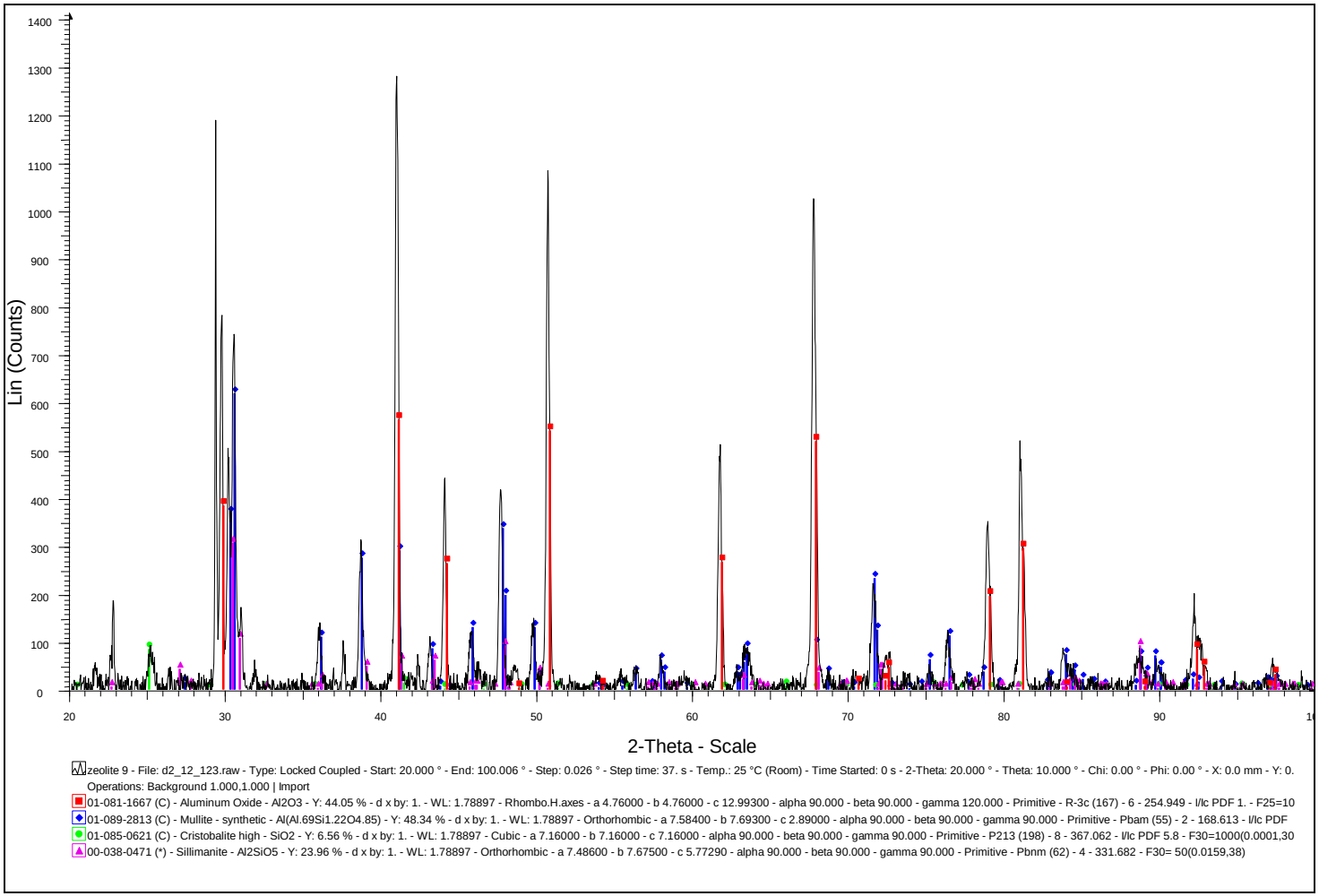


Figure A 7 High-alumina brick unused

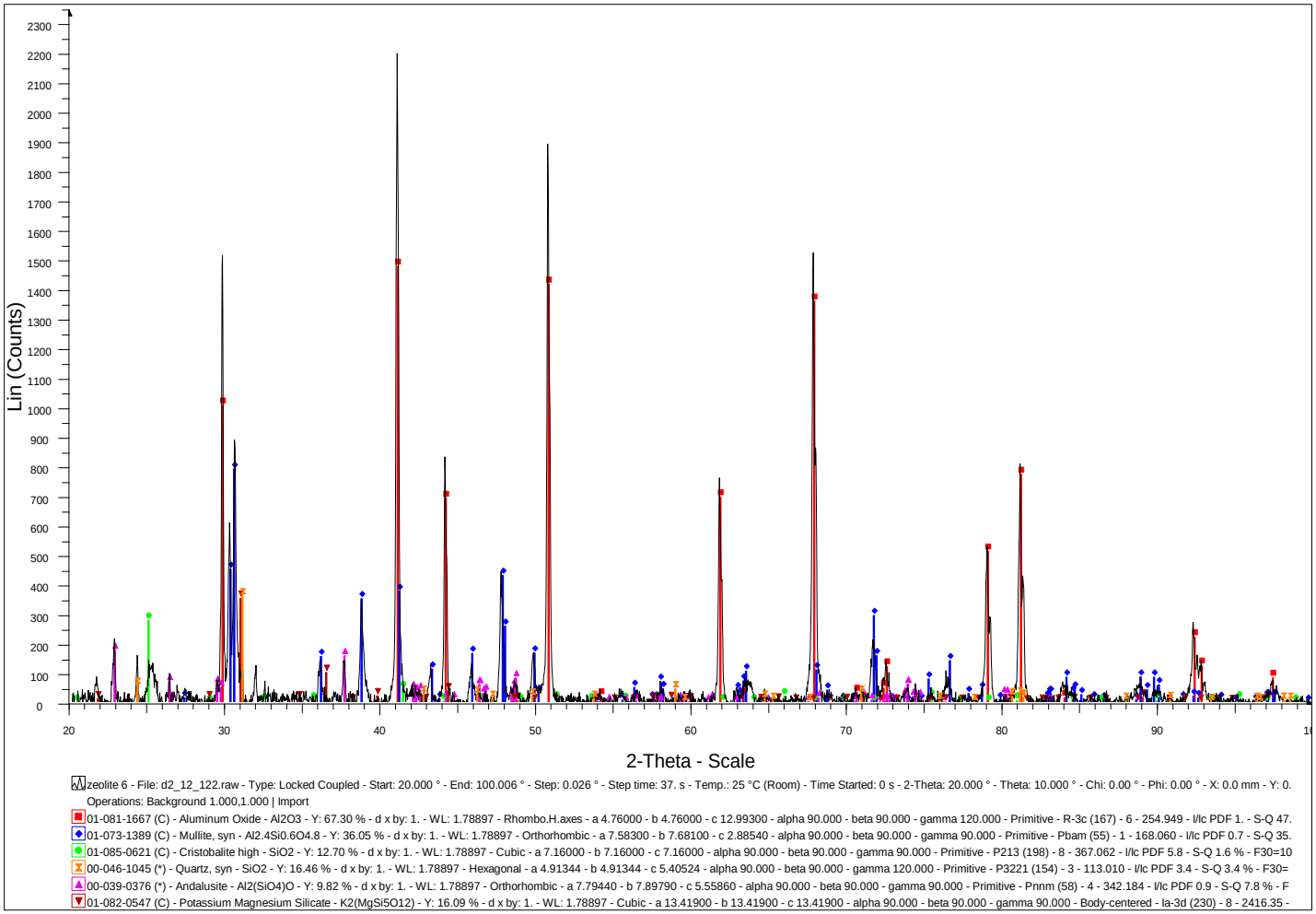


Figure A 8 High-alumina brick: used

APPENDIX B: Calculations for conversion from mass% to mole%

Table B 1 Calculation for Mass% to Moles%: Magnesia-spinel brick type A

Calculation for Mass% to Moles%: Magnesia-spinel brick type A

Species	XRF mass% Unused brick	molar masses	number of moles	XRF Mass% damaged brick	% Mole Fraction damaged brick
SiO_2	0.48	60.08	0.01	0.43	0.33
Al_2O_3	16.05	101.96	0.14	14.36	6.52
Fe_2O_3	0.49	159.69	0.00	0.52	0.15
CaO	5.30	56.08	0.11	6.30	5.20
MgO	77.68	40.30	1.82	73.42	84.35
Mn_2O_3	-	157.07	0.00	0.09	0.03
SO_3	-	80.06	0.01	0.87	0.50
Na_2O	-	61.98	0.01	0.53	0.40
Cl	-	35.45	0.03	0.99	1.29
K_2O	-	94.20	0.03	2.49	1.22
Total	100.00	846.89	2.16	100.00	100.00

Table B 2 Calculation for Mass% to Moles%: Magnesia-spinel brick type B

Calculation for Mass% to Moles%: Magnesia-spinel brick type B

Species	XRF mass% Unused brick	molar masses	number of moles	XRF Mass% damaged brick	% Mole Fraction damaged brick
SiO_2	0.67	60.08	0.01	0.68	0.52
Al_2O_3	14.07	101.96	0.16	15.93	7.20
Fe_2O_3	0.43	159.69	0.00	0.71	0.20
CaO	0.90	56.08	0.02	1.14	0.94
MgO	83.78	40.30	1.94	78.24	89.40
Mn_2O_3	0.15	157.07	0.00	0.15	0.04
SO_3	-	80.06	0.01	0.86	0.49
Na_2O	-	61.98	0.01	0.33	0.25
K_2O	-	94.20	0.02	1.96	0.96
Total	100.00	811.43	2.17	100.00	100.00

Table B 3 Calculation for Mass% to Moles%: Magnesia-fused spinel

Calculation for Mass% to Moles%: Magnesia-fused spinel

Species	XRF mass% Unused brick	molar masses	number of moles	XRF Mass% damaged brick	% Mole Fraction damaged brick
SiO_2	1.07	60.08	0.02	0.98	0.75
Al_2O_3	18.22	101.96	0.16	16.73	7.53
Fe_2O_3	0.67	159.69	0.00	0.61	0.18
CaO	1.26	56.08	0.02	1.20	0.98
MgO	78.79	40.30	1.95	78.57	89.41
Mn_2O_3	-	157.07	-	-	-
SO_3	-	80.06	0.00	0.35	0.20
Na_2O	-	61.98	0.01	0.34	0.25
Cl	-	35.45	0.00	0.14	0.18
K_2O	-	94.20	0.01	1.08	0.53
Total	100.01	846.89	2.18	100.00	100.00

Table B 4 Calculation for Mass% to Moles%: High - alumina brick

Species	XRF mass% Unused brick	molar masses	number of moles	XRF Mass% damaged brick	% Mole Fraction damaged brick
SiO_2	13.17	60.08	0.24	14.56	22.13
Al_2O_3	74.92	101.96	0.77	78.86	70.63
Fe_2O_3	2.57	159.69	0.01	1.74	0.99
CaO	5.85	56.08	0.01	0.68	1.11
MgO	0.48	40.30	0.01	0.31	0.70
TiO_2	3.01	79.87	0.04	3.12	3.57
SO_3	-	80.06	0.00	0.20	0.23
Na_2O	-	61.98	0.00	0.25	0.37
K_2O	-	94.20	0.00	0.28	0.27
Total	100.00	734.23	1.10	100.00	100.00

APPENDIX C: ASR data

Table C 1

Date	K_2O %	Na_2O %	SO_3 %	Cl %	ASR
Jan-10	2.07	0.20	1.30	0.37	1.23
Feb-10	2.05	0.21	0.78	0.32	2.12
Mar-10	2.15	0.13	1.01	0.30	1.64
Apr-10	1.71	0.18	0.90	0.29	1.51
May-10	2.19	0.10	1.37	0.27	1.23
Jun-10	2.07	0.01	2.05	0.33	0.68
Jul-10	1.94	0.02	2.95	0.33	0.44
Aug-10	2.14	0.10	1.94	0.38	0.78
Sep-10	2.24	0.29	1.42	0.31	1.36
Oct-10	2.37	0.23	1.32	0.32	1.48
Nov-10	2.16	0.07	1.61	0.39	0.92
Dec-10	2.04	0.13	1.62	0.47	0.85
Jan-11	2.12	0.09	1.69	0.51	0.80
Mar-11	1.72	0.26	0.88	0.24	1.74
Apr-11	1.52	0.28	1.01	0.25	1.36
May-11	2.06	0.16	1.04	0.29	1.57
Jun-11	1.85	0.22	1.33	0.27	1.17

The alkali-sulphate ratio is calculated as follows:

$$\mathrm{ASR} = \frac{\frac{\mathrm{Na_2O}}{\mathrm{Na_2O\,molarmass}} + \frac{\mathrm{K_2O}}{\mathrm{K_2O\,molarmass}} - \frac{\mathrm{Cl}}{\mathrm{Cl\,molarmass}}}{\frac{\mathrm{SO_3}}{\mathrm{SO_3\,molarmass}}}$$

APPENDIX D: Kiln feed composition

Table D 1 Kiln feed composition

Date	SiO_2	Al_2O_3	Fe_2O_3	Mn_2O_3	CaO	MgO	K_2O	Na_2O	TiO_2	SO_3	Cl
	%	%	%	%	%	%	%	%	%	%	%
Jan-10	20.83	4.12	2.67	1.16	66.53	2.23	0.49	0.39	0.23	0.02	0.03
Feb-10	20.57	4.12	3.05	1.26	66.02	2.43	0.57	0.41	0.23	0.01	0.03
Mar-10	20.76	4.11	2.54	1.12	66.33	2.32	0.58	0.41	0.22	0.02	0.02
Apr-10	20.79	3.79	2.59	1.01	66.06	2.40	0.60	0.44	0.22	0.03	0.02
May-10	20.77	3.72	2.62	1.19	66.75	2.39	0.56	0.48	0.22	0.02	0.02
Jun-10	20.97	3.61	2.62	1.43	67.23	2.58	0.45	0.35	0.22	0.03	0.03
Jul-10	20.73	3.62	2.65	1.36	66.21	3.26	0.45	0.37	0.21	0.03	0.03
Aug-10	20.95	3.60	2.66	1.23	67.25	2.43	0.47	0.48	0.20	0.03	0.03
Sep-10	21.10	3.97	2.54	1.21	67.98	2.48	0.53	0.67	0.20	0.03	0.02
Oct-10	21.00	4.08	2.58	1.11	67.99	2.40	0.54	0.61	0.21	0.03	0.03
Nov-10	20.86	3.80	2.62	1.10	67.24	2.54	0.62	0.44	0.21	0.05	0.01
Dec-10	20.78	3.55	2.66	0.88	66.80	2.50	0.53	0.42	0.20	0.06	0.01
Jan-11	20.73	3.66	2.67	0.84	66.34	2.37	0.51	0.40	0.21	0.05	0.01
Feb-11	20.90	3.69	2.56	0.74	66.11	2.32	0.61	0.49	0.21	0.05	0.01
Mar-11	20.61	3.86	2.64	1.37	65.49	2.69	0.52	0.51	0.21	0.04	0.01
Apr-11	20.18	3.41	2.70	1.73	64.99	4.04	0.44	0.44	0.20	0.06	0.01
May-11	20.11	3.65	2.53	1.57	64.68	3.33	0.60	0.48	0.21	0.04	0.02
Jun-11	20.34	3.69	2.49	1.28	65.71	2.99	0.55	0.48	0.21	0.05	0.03
AVERAGE	**21.00**	**3.83**	**2.67**	**1.22**	**67.32**	**2.69**	**0.54**	**0.47**	**0.22**	**0.04**	**0.02**

APPENDIX E: Residence time in Kiln

Residence time in Kiln “t”= $\frac{11.2 * \mathrm{L}}{DNS}$

L = Length of kiln in meter

S = Kiln inclination in degree

D = Effective diameter of kiln in meter

N = Rotation per minute (rpm)

Where D= 3.8 m, L= 70 m, S = 3 and N = 3.1

Residence time in Kiln “t”= $\frac{11.2 * 70}{3.8 * 3.1 * 3}$

Residence time in Kiln “t”= 22.2 minutes